R. & M. No. 3783

R. & M. No. 3783

PROCUREMENT EXECUTIVE, MINISTRY OF DEFENCE

AERONAUTICAL RESEARCH COUNCIL

REPORTS AND MEMORANDA

Evaluation of Pressure Distributions on Thin Wings with Distorted Control Surfaces Oscillating Harmonically in Linearised, Compressible, Subsonic Flow

Part 1: Details of the Mathematical Techniques Used in the Evaluation of the Pressure Distributions, and a Set of Numerical Results including Comparisons with Experiment

By W. R. MARCHBANK

British Aircraft Corporation Ltd.

LONDON: HER MAJESTY'S STATIONERY OFFICE

1976

PRICE £4·50 NET

Evaluation of Pressure Distributions on Thin Wings with Distorted Control Surfaces Oscillating Harmonically in Linearised, Compressible, Subsonic Flow

Part 1: Details of the Mathematical Techniques used in the Evaluation of the Pressure Distributions, and a Set of Numerical Results including Comparisons with Experiment

By W. R. MARCHBANK
British Aircraft Corporation Ltd.

Reports and Memoranda No. 3783*
January, 1975

Summary

Details of a method which enables the calculation of converged pressure distributions on a wing with distorted control surfaces oscillating harmonically in linearised, compressible subsonic flow, are presented. The local loading solutions, which have been developed from the original work of Landahl are used to extract the discontinuous part of the boundary conditions associated with oscillating control surfaces. The resulting regularised problem is then solved using a Lifting Surface Collocation procedure, giving together with the local solutions, the required pressure distribution. Results using the current theory for a rectangular wing and two swept tapered wings, are compared with experiment and other theoretical methods, including the long established 'equivalent modes' technique.

---

* Replaces A.R.C. 35 831.

LIST OF CONTENTS

1. Introduction

The work of Landahl (Ref. 1), in which the basic singular behaviour of the pressure distribution in the neighbourhood of the control-surface hinge-line corner was determined, has enabled direct solutions of the control-surface problem to be formulated. The present work extends that presented in References (2 and 9), to include the unsteady case with distorted control-surface vibration modes.

Part II of this report gives details of the suite of computer programs, which enable the calculation of pressure distributions and integrated effects for wing, control-surface configurations. Results from this new method have been compared with theoretical and experimental results from N.L.R. (Ref. 3), and with results using a program written by D. E. Davies (Ref. 4) which uses 'equivalent modes' to represent the control-surface mode.

2. Problem Formulation

Consider a very thin three-dimensional aerofoil and a system of cartesian coordinates x, y, z with the origin at the aerofoil apex. Fig. 1 shows such an aerofoil and indicates the position of the coordinate system relative to the wing.

The aerofoil is immersed in a compressible stream of undisturbed velocity U in the direction of the x-axis, and is assumed to deform harmonically with angular frequency ω about a mean position in the plane $z=0$.

Suppose that the vertical displacement of a point (x, y) on the aerofoil at time t be given by $z(x, y) \,.\, e^{i\omega t}$, and the corresponding pressure difference coefficient on the aerofoil surface be given by $\Delta C_p(x, y) \,.\, e^{i\omega t}$.

For small disturbances linearised theory applies, and the downwash at the aerofoil is given by,

$$w(x, y) = \frac{\partial z}{\partial x} + i \,.\, \frac{\omega}{U} \,.\, z, \tag{1}$$

and it may be shown (Ref. 5) that the pressure difference coefficient satisfies the integral equation,

$$w(x_r, y_s) = -\frac{1}{8\pi} \iint_S \Delta C_p(x, y) \,.\, K(X, Y; M, \nu) \,.\, dy\, dx, \tag{2}$$

where

$K(X, Y; M, \nu)$ is the Kernel Function,

$X = x_r - x$,
$Y = y_s - y$,

M is the free stream Mach Number,

ν is the reduced frequency based on semi-span,

S is the projected wing planform in the plane $z=0$. (3)

In general S is symmetric about $y=0$, and may be defined as follows

$$\begin{aligned} -s \leqslant\ & y \leqslant s, \\ x_l(y) \leqslant\ & x \leqslant x_t(y), \end{aligned} \tag{4}$$

where s is the semi-span and $x = x_l(y)$, $x = x_t(y)$ are the equations of the leading and trailing edge respectively.

Before proceeding to define ΔC_p and K in more detail, the cartesian coordinates x, y, z are non-dimensionalised by the semi-span s, and the basic problem re-formulated in terms of an x, y, z coordinate system based on s (*see* Fig. 1).

Thus from equation (1) the downwash at the aerofoil is given by

$$w(x, y) = \frac{\partial z}{\partial x} + i \,.\, \nu \,.\, z, \tag{5}$$

where

$$\nu = \frac{\omega . s}{u}, \tag{6}$$

and the integral equation becomes

$$w(x_r, y_s) = -\frac{1}{8\pi} \int_{x_l(y)}^{x_t(y)} \int_{-1}^{1} \Delta C_p(x, y) . s^2 . K(X,Y; M, \nu)\, dy\, dx. \tag{7}$$

2.1. The Kernel Function

Following Ref. (6) the Kernel function may be defined as follows,

$s^2 . K(X, Y; M, \nu) =$

For $\tau_1 > 0$

$$\frac{1}{Y^2}\left(1+\frac{X}{R}\right) . \{\cos(\nu\zeta) - i \sin(\nu\zeta)\} - \frac{\nu(1-M)}{R-X} . \{\sin(\nu\zeta) + i\cos(\nu\zeta)\} - \nu^2[\{G(\nu|Y|, \nu|\tau_1|) . \cos(\nu\zeta) -$$

$$- H(\nu|Y|, \nu|\tau_1|) . \sin(\nu\zeta)\} - \{G(\nu|Y|, \nu|\tau_1|) . \sin(\nu\zeta) + H(\nu|Y|, \nu|\tau_1|) . \cos(\nu\zeta)\}]$$

For $\tau_1 \leqslant 0$

$$\frac{1}{Y^2}\left[\left\{2\cos(\nu X) - \left(1-\frac{X}{R}\right) . \cos(\nu\zeta)\right\} - i\left\{2\sin(\nu X) - \left(1-\frac{X}{R}\right)\sin(\nu\zeta)\right\}\right] - \frac{\nu(1+M)}{R+X}\{\sin(\nu\zeta) + i\cos(\nu\zeta)\} -$$

$$- \nu^2[\{2G(\nu|Y|, 0)\cos(\nu X) - G(\nu|Y|, \nu|\tau_1|)\cos(\nu\zeta) - H(\nu|Y|, \nu|\tau_1|)\sin(\nu\zeta)\} -$$

$$- i\{2G(\nu|Y|, 0)\sin(\nu X) - G(\nu|Y|, \nu|\tau_1|)\sin(\nu\zeta) + H(\nu|Y|, \nu|\tau_1|)\cos(\nu\zeta)\}] \tag{8}$$

where

$$R = \sqrt{X^2 + \beta^2 Y^2}$$

$$\beta = \sqrt{1-M^2},$$

$$\tau_1 = \frac{MR - X}{\beta^2}$$

and

$$\zeta = X + \tau_1. \tag{9}$$

The functions G and H are defined in Ref. (6), and are evaluated using a technique introduced by Dat (Ref. 7) and developed by Kellaway (Ref. 6).

2.2. The Pressure Difference Coefficient ΔC_p

The pressure difference coefficient is defined by the equation,

$$\Delta C_p = \frac{p_l - p_u}{\frac{1}{2}\rho U^2}, \tag{10}$$

where

p_l = lower-surface pressure on the aerofoil,

p_u = upper-surface pressure on the aerofoil,

ρ = free-stream density,

and may be written in the form,

$$\Delta C_p(x, y) = \Delta C_p'(x, y) + i\Delta C_p''(x, y), \tag{11}$$

where $\Delta C_p'(x, y)$ denotes the real part of $\Delta C_p(x, y)$, and $\Delta C_p''(x, y)$ denotes the imaginary part of $\Delta C_p(x, y)$.

Following the work presented in Ref. 2, the ΔC_p distribution is assumed to be the sum of two distinct sub-distributions:

(i) ${}_1\Delta C_p$, a loading which only accounts for smooth variations of downwash over the aerofoil,

and

(ii) ${}_2\Delta C_p$, loading which accounts for the main downwash discontinuity effects associated with an oscillating, distorted control surface.

From the report, Ref. 5, a suitable representation for ${}_1\Delta C_p$ may be defined as follows,

$${}_1\Delta C_p = \sqrt{\frac{1-\xi_1}{1+\xi_1}} \,.\, \sqrt{1-\eta^2} \,.\, R^*(\xi_1, \eta), \tag{12}$$

where

$$\eta = y, \tag{13}$$

$$\xi_1 = \frac{2}{c(\eta)}\left\{x - \frac{1}{2}[x_l(\eta) + x_t(\eta)]\right\}, \tag{14}$$

$$c(\eta) = x_t(\eta) - x_l(\eta), \tag{15}$$

and where $R^*(\xi_1, \eta)$ is some regular but unknown function.

Before defining ${}_2\Delta C_p$ it is necessary to point out, that in order to calculate the downwash associated with this pressure distribution, it is most convenient to choose a generalised ξ coordinate in such a way that the planform's leading and trailing edges, and the hinge line are all constant ξ lines. In general then, such a coordinate system is defined through:

$$y = \eta \tag{16}$$

and

$$x = X_1(\eta, \xi) + \frac{(1-\xi^2)}{(1-\xi_h^2)} \,.\, \{x_h(\eta) - X_1(\eta, \xi_h)\}, \tag{17}$$

where

$$X_1(\eta, \xi) = x_l(\eta) \,.\, \frac{(1-\xi)}{2} + x_t(\eta) \,.\, \frac{(1+\xi)}{2}, \tag{18}$$

$x_h(\eta)$ is the equation of the hinge line and ξ_h is the coordinate of the hinge line in the (ξ, η) coordinate system.

2.3. The Assumed Definition of ${}_2\Delta C_p$

The analysis used to define the ${}_2\Delta C_p$ distribution was performed assuming, for the sake of generality, that the control-surface configuration is of the type shown in Fig. 2. That is, the control surface extends to the wing tip; clearly the principle of superposition may be used to define a ${}_2\Delta C_p$ distribution for control surfaces not extending to the wing tip.

The deformation mode in which the control surface is oscillating, is assumed to be of the form

$$z(x, y) = 0 \quad \text{for points } (x, y) \text{ off the control surface}$$

and

$$z(x, y) = \bar{X} \,.\, F(\bar{X}, \bar{Y}) \quad \text{for points } (x, y) \text{ on the control surface,} \tag{19}$$

where

$$\bar{X} = x - x_h(y), \tag{20}$$

$$\begin{aligned}\bar{Y} &= \eta - \eta_e,\\ &= y - y_e,\end{aligned} \tag{21}$$

$y_e = \eta_e$ is the side edge of the control surface, and $F(\bar{X}, \bar{Y})$ is some regular function.

From equation (19) it is clear that finite discontinuities in $z(x, y)$ at the hinge line are not allowed.

Using the control-surface deformation defined by equation (19), it was shown in Ref. 8 that a suitable form for ${}_2\Delta C_p$ could be defined as follows:

$${}_2\Delta C_p(x, y) = 2[p(x, y) \pm p(x, -y)], \tag{22}$$

with the plus sign corresponding to symmetric control-surface modes, and the minus sign corresponding to anti-symmetric control-surface modes,

$$p(x, y) = p_1(x, y) + p_2(x, y) + p_3(x, y). \tag{23}$$

The definition of $p_1(x, y)$

$$p_1(x, y) = \bar{P}(x, y) \,.\, \bar{F}(y) \,.\, A(x, y) \,.\, \bar{Y} \,.\left\{\log\left[\frac{\sqrt{R_p + x_t - x} - \sqrt{2(x_t - x)}}{\sqrt{R_p + x_t - x} + \sqrt{2(x_t - x)}}\right] - \log\left[\frac{\sqrt{R_e + (x_t - x_h)} - \sqrt{x_t - x}}{\sqrt{R_e + (x_t - x_h)} + \sqrt{x_t - x}}\right]\right\}, \tag{24}$$

where

$$R_p = \sqrt{(x_t - x)^2 + \bar{\bar{\beta}}^2 \bar{Y}^2}, \tag{25}$$

$$\bar{\bar{\beta}} = \sqrt{\beta^2 + \kappa_t^2}, \tag{26}$$

$$\kappa_t = x_t'(y_e), \tag{27}$$

$$R_e = \sqrt{\bar{X}^2 + \bar{\beta}^2 \bar{Y}^2}, \tag{28}$$

$$\bar{\beta} = \sqrt{\beta^2 + \kappa_0^2}, \tag{29}$$

$$\kappa_0 = x_h'(y_e), \tag{30}$$

$$A(x, y) = A'(x, y) + iA''(x, y), \tag{31}$$

$$A'(x, y) = -\frac{1}{\pi}\left[2F_{\bar{X}}(\bar{X}, 0) + \bar{Y}\left\{F_{\bar{X}y}(\bar{X}, 0) + \frac{3}{2}\kappa_0 F_{\bar{X}\bar{X}}(\bar{X}, 0) - \frac{\kappa_0}{2}\nu^2 F(\bar{X}, 0)\right\} + \bar{X}\{F_{\bar{X}\bar{X}}(\bar{X}, 0) - \nu^2 F(\bar{X}, 0)\}\right], \tag{32}$$

$$A''(x, y) = -\frac{\nu}{\pi}[2F(\bar{X}, 0) + \bar{Y}\{F_y(\bar{X}, 0) + 2\kappa_0 F_{\bar{X}}(\bar{X}, 0)\} + 2 \,.\, \bar{X} \,.\, F_{\bar{X}}(\bar{X}, 0)], \tag{33}$$

$$\bar{P}(x, y)=\sqrt{\frac{1+\xi}{1+\xi_1}}\left[1-\frac{1}{2}\frac{(\xi-\xi_1)}{(1+\xi_1)}+\frac{3}{8}\frac{(\xi-\xi_1)^2}{(1+\xi_1)^2}\right] \qquad \xi<\xi_1,$$
$$=1 \qquad \xi\geqslant\xi_1. \tag{34}$$

with

$$\xi_1=\frac{(-1+\xi_h)}{2}, \tag{35}$$

giving the required $\sqrt{}$ zero at the leading edge, and

$$\bar{F}(y)=\sqrt{\frac{1-y}{1-y_e}}\left(1+\frac{\bar{Y}}{2(1-y_e)}+\frac{3}{8}\frac{\bar{Y}^2}{(1-y_e)^2}\right) \qquad y>y_e,$$
$$=\sqrt{\frac{1+y}{1+y_e}}\left(1-\frac{\bar{Y}}{2(1+y_e)}+\frac{3}{8}\frac{\bar{Y}^2}{(1+y_e)^2}\right) \qquad y\leqslant y_e, \tag{36}$$

giving a $\sqrt{}$ zero at both the starboard and port wing tips.

Definition of $p_2(x, y)$

$$p_2(x, y)=H_1(y)\,.\,B(x, y)\,.\left\{\bar{C}(x)\,.\,\log\left[\frac{\sqrt{R_t+\bar{\beta}(1-y)}-\sqrt{2\bar{\beta}(1-y)}}{\sqrt{R_t+\bar{\beta}(1-y)}+\sqrt{2\bar{\beta}(1-y)}}\right]-\log\left[AG(x, y)\right]\right\}+$$
$$+\bar{C}(x)\,.\,H_1(y)\,.\,\bar{G}\,.\,\frac{\bar{X}}{R_t}\,.\,\sqrt{\frac{2\bar{\beta}(1-y)}{R_t+\bar{\beta}(1-y)}}, \tag{37}$$

where

$$R_t=\sqrt{\bar{X}^2+\bar{\beta}^2(1-y)^2}, \tag{38}$$

$$AG(x, y)=\frac{\sqrt{R_e+\bar{\beta}\bar{Y}+S^*(x, y)}-\sqrt{S^*(x, y)}}{\sqrt{R_e+\bar{\beta}\bar{Y}+S^*(x, y)}+\sqrt{S^*(x, y)}}, \tag{39}$$

$$S^*(x, y)=\frac{(x_t-x)\,.\,(x-x_l)(1-y)}{c_1\,.\,c_2\,.\,(1-y_e)}, \tag{40}$$

$$c_1=x_t-x_h, \tag{41}$$

$$c_2=x_h-x_l, \tag{42}$$

$$B(x, y)=B'(x, y)+iB''(x, y), \tag{43}$$

$$B'(x, y)=-\frac{1}{\pi\bar{\beta}}\left[F(0, \bar{Y})+\bar{X}\left\{2\,.\,F_{\bar{X}}(0, \bar{Y})+\frac{\kappa_0}{\bar{\beta}^2}\,.\,F_y(0, \bar{Y})\right\}+\right.$$
$$+\bar{X}^2\left\{\frac{3}{2}F_{\bar{X}\bar{X}}(0, \bar{Y})+\frac{\kappa_0}{\bar{\beta}^2}F_{\bar{X}y}(0, \bar{Y})-\frac{\nu^2}{2}\left(1+\frac{1}{2}\frac{M^2}{\bar{\beta}^2}\left(5+3\frac{M^2}{\bar{\beta}^2}\right)\right)F(0, \bar{Y})+\right.$$
$$\left.\left.+\left(\frac{3}{4}\,.\,\frac{\kappa_0^2}{\bar{\beta}^4}-\frac{1}{4\bar{\beta}^2}\right)\,.\,F_{yy}(0, \bar{Y})\right\}\right], \tag{44}$$

$$B''(x, y)=-\frac{\bar{X}\nu}{\pi\bar{\beta}}\left[\left(2+\frac{M^2}{\bar{\beta}^2}\right)\,.\,(F(0, \bar{Y})+\bar{X}\,.\,F_{\bar{X}}(0, \bar{Y}))+\bar{X}\,.\,\frac{\kappa_0}{\bar{\beta}^2}\,.\,\left(1+\frac{3}{2}\frac{M^2}{\bar{\beta}^2}\right)\,.\,F_y(0, \bar{Y})\right], \tag{45}$$

$$\bar{G} = -\frac{\kappa_0}{\pi\bar{\beta}^2}\left[1+\frac{1}{32}\left(\frac{\kappa_0}{\bar{\beta}}\right)^2\right].F(0, 0), \tag{46}$$

$$\begin{aligned}\bar{C}(x, y) &= \sqrt{\frac{x_t - x}{c_1}}\left(1+\frac{1}{2c_1}\bar{X}+\frac{3}{8c_1^2}.\bar{X}^2\right) \qquad x > x_h,\\ &= \sqrt{\frac{x - x_l}{c_2}}\left(1-\frac{1}{2c_2}\bar{X}+\frac{3}{8c_2^2}.\bar{X}^2\right) \qquad x \leqslant x_h,\end{aligned} \tag{47}$$

giving a $\sqrt{}$ zero at both the leading and trailing edges of the wing,

$$\begin{aligned}H_1(y) &= 1 \qquad y \geqslant -y_2\\ &= \sqrt{1+y}.\frac{1}{16(1-y_2)^{\frac{7}{2}}}[-5y^3+3(2-7y_2)y^2-(35y_2^2-28y_2+8)y+\\ &\quad +(-35y_2^3+70y_2^2-56y_2+16)] \qquad y < -y_2\end{aligned} \tag{48}$$

where $y_2 = 0{\cdot}6$, giving a $\sqrt{}$ zero at the port tip.

The definition of $p_3(x, y)$

$$p_3(x, y) = \bar{F}(y).\bar{C}(x, y)\left[C(x, y).\frac{\bar{X}}{R_e}+E(x, y).R_e+D\frac{\bar{Y}^3}{R_e^3}\right] \tag{49}$$

where

$$C(x, y) = C'(x, y)+iC''(x, y), \tag{50}$$

with

$$\begin{aligned}C'(x, y) &= \frac{1}{\pi\bar{\beta}}\left[\frac{1}{2}\log\left(\frac{\bar{\beta}+\kappa_0}{\bar{\beta}-\kappa_0}\right)F(0, 0)+\frac{\bar{X}}{2}.\frac{\kappa_0^2}{\bar{\beta}^3}.F_y(0, 0)+\right.\\ &\quad \left.+\bar{Y}\left\{\frac{1}{2}\log\left(\frac{\bar{\beta}+\kappa_0}{\bar{\beta}-\kappa_0}\right)-\frac{\kappa_0}{\bar{\beta}}\right\}.F_y(0, 0)-\bar{Y}.\bar{\beta}.\log\left(1-\left(\frac{\kappa_0}{\bar{\beta}}\right)^2\right).F_{\bar{X}}(0, 0)\right],\end{aligned} \tag{51}$$

$$C''(x, y) = \frac{\nu}{\pi}F(0, 0)\left[-\bar{Y}\log\left(1-\left(\frac{\kappa_0}{\bar{\beta}}\right)^2\right)+\bar{Y}\frac{(\kappa_0/\bar{\beta})^2}{1-(\kappa_0/\bar{\beta})^2}.\frac{M^2}{\bar{\beta}^2}+\bar{X}.\frac{\kappa_0}{\bar{\beta}^4}.M^2\right], \tag{52}$$

and

$$E(x, y) = E'(x, y)+iE''(x, y), \tag{53}$$

with

$$\begin{aligned}E'(x, y) &= \frac{1}{\pi\bar{\beta}}\left[\frac{-F_y(0, 0)}{\bar{\beta}}+2\frac{\kappa_0}{\bar{\beta}}.F_{\bar{X}}(0, 0)+\frac{\kappa_0^2}{2\bar{\beta}^3}.F_y(0, 0)+\right.\\ &\quad \left.+\log\left(\frac{\bar{\beta}+\kappa_o}{\bar{\beta}-\kappa_0}\right).\left(F_{\bar{X}}(0, 0)+\frac{1}{2}\frac{\kappa_0}{\bar{\beta}^2}.F_y(0, 0)\right)\right],\end{aligned} \tag{54}$$

$$\begin{aligned}E''(x, y) &= \frac{\nu}{\pi\bar{\beta}}F(0, 0)\left[\log\left(\frac{\bar{\beta}+\kappa_0}{\bar{\beta}-\kappa_0}\right).\left(1+\frac{1}{2}\frac{M^2}{\bar{\beta}^2}\right)+\frac{\kappa}{\bar{\beta}^2}\left(2+\frac{M^2}{\bar{\beta}^2}\right)+\right.\\ &\quad \left.+\frac{M^2}{\bar{\beta}^2}\frac{(\kappa_0/\bar{\beta})}{1-(\kappa_0/\bar{\beta})^2}\right],\end{aligned} \tag{55}$$

also

$$D = -\frac{1}{2\pi}\bar{\beta}^2\log\left(1-\frac{\kappa_0^2}{\bar{\beta}^2}\right). \tag{56}$$

2.4. Introduction of the Term 'Regularised Downwash'

From equation (7), and using the breakdown of the pressure difference coefficient into ${}_1\Delta C_p$ and ${}_2\Delta C_p$ as described in Section 2.2, it is possible to write

$$w(x_r, y_s) = w_1(x_r, y_s) + w_2(x_r, y_s), \tag{57}$$

where

$$w_1(x_r, y_s) = -\frac{1}{8\pi}\int_{x_l(y)}^{x_t(y)}\int_{-1}^{1} {}_1\Delta C_p(x, y)\,.\,s^2\,.\,K(X, Y; M, \nu)\,dy\,dx, \tag{58}$$

and

$$w_2(x_r, y_s) = -\frac{1}{8\pi}\int_{x_l(y)}^{x_t(y)}\int_{-1}^{1} {}_2\Delta C_p(x, y)\,.\,s^2\,.\,K(X, Y; M, \nu)\,dy\,dx \tag{59}$$

The function $w_1(x_r, y_s)$ introduced above is known as the regularised downwash. The reason for this is that provided ${}_2\Delta C_p(x, y)$ has been well defined, the downwash function $w_2(x_r, y_s)$ will contain the main discontinuity effects associated with the prescribed boundary conditions, thus ensuring the regularity of

$$w_1(x_r, y_s) = w(x_r, y_s) - w_2(x_r, y_s).$$

The regularised downwash, once it has been calculated, defines a smooth-lifting-surface problem which may be solved using existing techniques to give ${}_1\Delta C_p(x, y)$.

Clearly then, the main problem is to evaluate $w_2(x_r, y_s)$ accurately, which immediately facilitates the evaluation of $w_1(x_r, y_s)$, the regularised downwash.

3. Preliminary Analytic Work on the Evaluation of $w_2(x_r, y_s)$

The Kernel function $K(X, Y; M, \nu)$ defined by equation (8) is clearly very irregular near $Y=0$, $X=0$, and is singular for $Y=0$. It is this behaviour attributed to $K(X, Y; M, \nu)$, which can cause severe numerical problems in the evaluation of $w_2(x_r, y_s)$, unless great care is taken. So that detailed knowledge of $K(X, Y; M, \nu)$, and of the effect that this function has on the subsequent integrations, is required.

3.1. The Transformation of the Integral Equation for $w_2(x_r, y_s)$ to the (ξ, η) Coordinate System

Consider the transformation of the integral equation (59) to the (ξ, η) coordinate system defined by equations (16), (17) and (18), then

$$dy\,.\,dx = J(\xi, \eta)\,.\,d\xi\,.\,d\eta, \tag{60}$$

where

$$J(\xi, \eta) = \frac{c(\eta)}{2} - \frac{2\xi}{1-\xi_h^2}\{x_h(\eta) - X_1(\eta, \xi_h)\}. \tag{61}$$

The Kernel function has arguments Y, X which transform to give:

$$\begin{aligned} Y &= y_s - y, \\ &= \eta_s - \eta, \\ &= \bar{\eta} \text{ say,} \end{aligned} \tag{62}$$

where $\eta_s = y_s$.

$$\begin{aligned} X &= x_r - x, \\ &= X_1(\eta_s, \xi_r) - X_1(\eta, \xi) + \frac{(1-\xi_r^2)}{(1-\xi_h^2)}\,.\,\{x_h(\eta_s) - X_1(\eta_s, \xi_h)\} - \frac{(1-\xi^2)}{(1-\xi_h^2)}\{x_h(\eta) - X_1(\eta, \xi_h)\}, \\ &= X_1(\eta_s, \xi_r) - X_1(\eta, \xi) + \frac{(1-\xi^2)}{(1-\xi_h^2)}\,.\,\{x_h(\eta_s) - x_h(\eta) - [X_1(\eta_s, \xi_h) - X_1(\eta, \xi_h)]\} - \\ &\quad -\bar{\xi}\,.\,\frac{(\xi+\xi_r)}{(1-\xi_h^2)}\,.\,\{x_h(\eta_s) - X_1(\eta_s, \xi_h)\}, \end{aligned} \tag{63}$$

where

$$\bar{\xi} = \xi_r - \xi. \tag{64}$$

Now from equation (18),

$$X_1(\eta, \xi) = \frac{c(\eta)}{2} \cdot (1+\xi) + x_l(\eta), \tag{65}$$

giving

$$X_1(\eta_s, \xi_r) - X_1(\eta, \xi) = \tfrac{1}{2}\{[\bar{\Delta}x_l(\eta) + \bar{\Delta}x_t(\eta)] - \xi[\bar{\Delta}x_l(\eta) - \bar{\Delta}x_t(\eta)]\} \cdot \bar{\eta} + \frac{c(\eta_s)}{2} \cdot \bar{\xi},$$

$$= g(\xi, \eta) \cdot \bar{\eta} + \frac{c(\eta_s)}{2} \cdot \bar{\xi}, \tag{66}$$

where

$$\bar{\Delta}x_l(\eta) = \frac{x_l(\eta_s) - x_l(\eta)}{\bar{\eta}}, \tag{67}$$

with a similar expression for $\bar{\Delta}x_t(\eta)$, and

$$g(\xi, \eta) = \tfrac{1}{2}\{[\bar{\Delta}x_l(\eta) + \bar{\Delta}x_t(\eta)] - \xi[\bar{\Delta}x_l(\eta) - \bar{\Delta}x_t(\eta)]\}. \tag{68}$$

The expression for X now may be written in the form:

$$X = g_1(\xi, \eta) \cdot \bar{\eta} + g_2(\xi) \cdot \bar{\xi}, \tag{69}$$

where

$$g_1(\xi, \eta) = g(\xi, \eta) + \frac{(1-\xi^2)}{(1-\xi_h^2)} \cdot \{\bar{\Delta}x_h(\eta) - g(\xi_h, \eta)\}, \tag{70}$$

and

$$g_2(\xi) = \frac{c(\eta_s)}{2} - \frac{(\xi+\xi_r)}{(1-\xi_h^2)} \cdot \{x_h(\eta_s) - X_1(\eta_s, \xi_h)\}. \tag{71}$$

The integral equation (59) becomes,

$$w_2(x_r, y_s) = -\frac{1}{8\pi} \int_{-1}^{1} \not\!\!\int_{-1}^{1} {}_2\Delta C_p(x, y) \cdot J(\xi, \eta) \cdot \bar{K}(\bar{\xi}, \bar{\eta}; M, \nu)\, d\eta\, d\xi, \tag{72}$$

where $\bar{K}(\bar{\xi}, \bar{\eta}; M, \nu)$ is the transformed Kernel function.

Introduce the function $L(\xi)$ where,

$$L(\xi) = \not\!\!\int_{-1}^{1} {}_2\Delta C_p(x, y) \cdot J(\xi, \eta) \cdot \bar{K}(\bar{\xi}, \bar{\eta}; M, \nu)\, d\eta, \tag{73}$$

then

$$w_2(x_r, y_s) = -\frac{1}{8\pi} \int_{-1}^{1} L(\xi)\, d\xi. \tag{74}$$

Clearly a detailed knowledge of the functional behaviour of $L(\xi)$ is required, in order to evaluate accurately $w_2(x_r, y_s)$.

3.2. A Detailed Analysis of $L(\xi)$

The Kernel function may be re-written in the form,

$$\bar{K}(\bar{\xi}, \bar{\eta}\,; M, \nu) = \frac{1}{\bar{\eta}^2}\left(\frac{X}{R} - \text{sgn}\,(\bar{\xi})\right) . \{(\cos(\nu\zeta) + \nu\tau_1 \sin(\nu\zeta)) - i(\sin(\nu\zeta) -$$
$$-\nu\tau_1 \cos(\nu\zeta))\} - \frac{\nu}{R}(\sin(\nu\zeta) + i\cos(\nu\zeta)) -$$
$$-\nu^2[\{G(\nu|\bar{\eta}|, \nu|\tau_1|)\cos(\nu\zeta) - H(\nu|\bar{\eta}|, \nu|\tau_1|)\sin(\nu\zeta)\} -$$
$$-i\{G(\nu|\bar{\eta}|, \nu|\tau_1|)\sin(\nu\zeta) + H(\nu|\bar{\eta}|, \nu|\tau_1|)\cos(\nu\zeta\}] + \bar{\bar{K}}(\bar{\xi}, \bar{\eta}; M, \nu) \tag{75}$$

where
For $\bar{\xi} < 0$
with $\tau_1 \geqslant 0$

$$\bar{\bar{K}}(\bar{\xi}, \bar{\eta}; M, \nu) = 0, \tag{76}$$

and *with* $\tau_1 > 0$

$$\bar{\bar{K}}(\bar{\xi}, \bar{\eta}; M, \nu) = \frac{2}{\bar{\eta}^2}[\{\cos\nu X - (\cos\nu\zeta + \nu\tau_1\sin\nu\zeta)\} - i\{\sin\nu X - (\sin\nu\zeta - \nu\tau_1\cos\nu\zeta)\}] -$$
$$-2\,.\,\nu^2[\{G(\nu|\bar{\eta}|, 0)\cos\nu X - G(\nu|\bar{\eta}|, \nu|\tau_1|)\cos\nu\zeta\} -$$
$$-i\{G(\nu|\bar{\eta}|, 0)\sin\nu X - G(\nu|\bar{\eta}|, \nu|\tau_1|)\sin\nu\zeta\}]. \tag{77}$$

For $\bar{\xi} \geqslant 0$
with $\tau_1 > 0$

$$\bar{\bar{K}}(\bar{\xi}, \bar{\eta}; M, \nu) = \frac{2}{\bar{\eta}^2}[\{\cos\nu\zeta + \nu\tau_1\sin\nu\zeta\} - i\{\sin\nu\zeta - \nu\tau_1\cos\nu\zeta\}], \tag{78}$$

and *with* $\tau_1 \leqslant 0$

$$\bar{\bar{K}}(\bar{\xi}, \bar{\eta}; M, \nu) = \frac{2}{\bar{\eta}^2}[\cos\nu X - i\sin\nu X] - 2\,.\,\nu^2[\{G(\nu|\bar{\eta}|, 0)\cos\nu X - G(\nu|\bar{\eta}|, \nu|\tau_1|)\cos\nu\zeta\} -$$
$$-i\{G(\nu|\bar{\eta}|, 0)\sin\nu X - G(\nu|\bar{\eta}|, \nu|\tau_1|)\sin\nu\zeta\}]. \tag{79}$$

From previous work on the static-control-surface problem (Ref. 2), it is clear that the dominant singularities in the $L(\xi)$ function will arise through the term $N(\bar{\xi}, \bar{\eta}; M, \nu)$ in the Kernel function, where

$$N(\bar{\xi}, \bar{\eta}; M, \nu) = \frac{1}{\bar{\eta}^2}\frac{X}{R}\{(\cos\nu\zeta + \nu\tau_1\sin\nu\zeta) - i(\sin\nu\zeta - \nu\tau_1\cos\nu\zeta)\} - \frac{\nu}{R}(\sin\nu\zeta + i\cos\nu\zeta) \tag{80}$$

Consider then the integral

$$\bar{L}(\xi) = \int_{\eta_s - \bar{A}}^{\eta_s + \bar{B}} {}_2\Delta C_p(x, y)\,.\,J(\xi, \eta)\,.\,N(\bar{\xi}, \bar{\eta}; M, \nu)\,d\eta, \tag{81}$$

where $\bar{A}$, $\bar{B}$ are positive parameters sufficiently small to allow a Taylor Series expansion of ${}_2\Delta C_p(x, y)\,.\,J(\xi, \eta)$ about η_s for $\eta_s \neq \eta_e$, $\xi \neq \xi_h$. Using the work in Ref. 6, and writing $U^*(\xi, \eta) = {}_2\Delta C_p(x, y).\ J(\xi, \eta)$, it may be shown that

$$\bar{L}(\xi) = \frac{-2U^*(\xi_r, \eta_s)}{g_2(\xi_r)}\,.\,\sqrt{a(\xi_r, \eta_s)}\,.\,\frac{1}{\bar{\xi}} + \frac{2}{\sqrt{a(\xi_r, \eta_s)}}\left\{\frac{\beta^2}{a(\xi_r, \eta_s)}\left[\frac{\partial}{\partial\eta}g_1(\xi, \eta)\right]_{\substack{\eta=\eta_s\\ \xi=\xi_r}}.\ U^*(\xi_r, \eta_s) +\right.$$
$$\left. + g_1(\xi_r, \eta_s)\,.\left[\frac{\partial}{\partial\eta}U^*(\xi, \eta)\right]_{\substack{\eta=\eta_s\\ \xi=\xi_r}} + i\,.\,\nu U^*(\xi_r, \eta_s)\,.\,(1 + g_1^2(\xi_r, \eta_s))\right\}\log|\bar{\xi}| +$$
$$+ 0(\bar{\xi}\log|\bar{\xi}|) + \text{regular terms as } \bar{\xi} \to 0 \text{ with } \xi_r \neq \xi_h, \tag{82}$$

with

$$a(\xi_r, \eta_s) = \beta^2 + g_1^2(\xi_r, \eta_s). \tag{83}$$

Thus the exact analytic behaviour of $L(\xi)$ near ξ_r has been determined. Clearly this information is absolutely necessary in order to formulate successfully the numerical integration of $L(\xi)$.

4. The Evaluation of $w_2(x_r, y_s)$

As indicated in Section 3, and following Ref. 5 the double integral defining $w_2(x_r, y_s)$ is evaluated in the first instance with respect to η, then with respect to ξ.

4.1. The Integration with Respect to η

The highly singular nature of the Kernel function in the neighbourhood of η_s indicates a natural division of the integral defining $L(\xi)$. The range of integration is sub-divided into three regions,

$$\begin{aligned} &\text{Region 1} \quad && -1 \leqslant \eta \leqslant \eta_s - \bar{A}, \\ &\text{Region 2} \quad && \eta_s + \bar{B} \leqslant \eta \leqslant 1, \\ &\text{Region 3} \quad && \eta_s - \bar{A} < \eta < \eta_s + \bar{B}. \end{aligned} \tag{84}$$

In Ref. 2 suitable values of the parameters $\bar{A}$, $\bar{B}$ were found to be

$$\begin{aligned} \bar{A} &= 0.1, \\ \bar{B} &= \begin{cases} 0.1 & \text{for} \quad \eta_s \leqslant 0.9, \\ 1-\eta_s & \text{for} \quad \eta_s > 0.9. \end{cases} \end{aligned} \tag{85}$$

The regional breakdown of the spanwise integral is shown in Fig. 2. For the integrations over Regions 1 and 2 the Kernel function defined by equation (75) may be used, since this is the simpler form, and all singularities and irregularities in the Kernel function are confined to Region 3. However, for the integration over Region 3 a form must be used which identifies more explicitly the singularities of the Kernel function as functions of ξ and η.

4.1.1. *The rearrangement of the Kernel function for the integration over Region* 3. The function X/R may be written in the form

$$\frac{X}{R} = \operatorname{sgn}(\bar{\xi}) - \frac{\beta^2 \bar{\eta}^2 \operatorname{sgn}(\bar{\xi})}{R[R + X \operatorname{sgn}(\bar{\xi})]}, \tag{86}$$

so that using equation (75) it is possible to rewrite the Kernel function in the form

$$\bar{K}(\bar{\xi}, \bar{\eta}; M, \nu) = K_1(\bar{\xi}, \bar{\eta}; M, \nu) + K_2(\bar{\xi}, \bar{\eta}; M, \nu) + K_3(\bar{\xi}, \bar{\eta}; M, \nu), \tag{87}$$

where

$$K_1(\bar{\xi}, \bar{\eta}\,; M, \nu) = \frac{-\beta^2 \operatorname{sgn}(\bar{\xi})}{R[R + X \operatorname{sgn}(\bar{\xi})]}\{(\cos \nu\zeta + \nu\tau_1 \sin \nu\zeta) - i(\sin \nu\zeta - \nu\tau_1 \cos \nu\zeta)\}, \tag{88}$$

and *for* $\bar{\xi} \leqslant 0$

$$K_2(\bar{\xi}, \bar{\eta}; M, \nu) = 0, \tag{89}$$

for $\bar{\xi} > 0$

$$K_2(\bar{\xi}, \bar{\eta}; M, \nu) = \left(\frac{2}{\bar{\eta}^2} + \nu^2 \log|\bar{\eta}|\right).(\cos \nu X - i \sin \nu X), \tag{90}$$

$$K_3(\bar{\xi}, \bar{\eta}\,; M, \nu) = -\frac{\nu}{R}(\sin \nu\zeta + i \cos \nu\zeta) - \nu^2[\{G(\nu|\bar{\eta}|, \nu|\tau_1|) \cos \nu\zeta - H(\nu|\bar{\eta}|, \nu|\tau_1|) \sin \nu\zeta\} -$$
$$- i\{G(\nu|\bar{\eta}|, \nu|\tau_1|) \sin \nu\zeta + H(\nu|\bar{\eta}|, \nu|\tau_1|) \cos \nu\zeta\}] + \bar{K}_3(\bar{\xi}, \bar{\eta}\,; M, \nu), \tag{91}$$

with $\bar{K}_3(\bar{\xi}, \bar{\eta}; M, \nu)$ defined as follows:

For $\bar{\xi} < 0$
with $\tau_1 \geqslant 0$

$$\bar{K}_3(\bar{\xi}, \bar{\eta}; M, \nu) = 0, \tag{92}$$

and *with* $\tau_1 < 0$

$$\bar{K}_3(\bar{\xi}, \bar{\eta}; M, \nu) = \frac{2}{\bar{\eta}^2}[\{\cos \nu X - (\cos \nu\zeta + \nu\tau_1 \sin \nu\zeta)\} - i\{\sin \nu X - (\sin \nu\zeta - \nu\tau_1 \cos \nu\zeta)\}] -$$
$$- 2\nu^2[\{G(\nu|\bar{\eta}|, 0) \cos \nu X - G(\nu|\bar{\eta}|, \nu|\tau_1|) \cos \nu\zeta\}$$
$$- i\{G(\nu|\bar{\eta}|, 0) \sin \nu X - G(\nu|\bar{\eta}|, \nu|\tau_1|) \sin \nu\zeta\}], \tag{93}$$

For $\bar{\xi} \geqslant 0$
with $\tau_1 \geqslant 0$

$$\bar{K}_3(\bar{\xi}, \bar{\eta}; M, \nu) = \frac{2}{\bar{\eta}^2}[\{\cos \nu\zeta + \nu\tau_1 \sin \nu\zeta - \cos \nu X\} - i\{\sin \nu\zeta - \nu\tau_1 \cos \nu\zeta - \sin \nu X\}] -$$
$$- \nu^2 \log |\bar{\eta}| \,.\, [\cos \nu X - i \sin \nu X], \tag{94}$$

and *with* $\tau_1 < 0$

$$\bar{K}_3(\bar{\xi}, \bar{\eta}\,; M, \nu) = -2\nu^2[\{G^*(\nu|\bar{\eta}|, 0) \cos \nu X - G(\nu|\bar{\eta}|, \nu|\tau_1|) \cos \nu\zeta\} -$$
$$- i\{G^*(\nu|\bar{\eta}|, 0) \sin \nu X - G(\nu|\bar{\eta}|, \nu|\tau_1|) \sin \nu\zeta\}], \tag{95}$$

where

$$G^*(\nu|\bar{\eta}|, 0) = G(\nu|\bar{\eta}|, 0) + \tfrac{1}{2} \log |\bar{\eta}|. \tag{96}$$

It was shown in Ref. 6 that

$$G(\nu|\bar{\eta}|, 0) = -\tfrac{1}{2} \log |\bar{\eta}| + \text{regular terms as } |\bar{\eta}| \to 0, \tag{97}$$

so that the function $G^*(\nu|\bar{\eta}|, 0)$ is regular as $|\bar{\eta}| \to 0$. The singular term extracted from $G(\nu|\bar{\eta}|, 0)$ has been incorporated in the K_2 term, this proves convenient for the numerical η-integration.

The Kernel function then, has been separated into three basic terms. K_1 is a highly irregular function for $(\bar{\eta}, \bar{\xi}) \to (0, 0)$, K_2 is singular and gives a finite part integral, K_3 includes the complicated humerical functions $G(\nu|\bar{\eta}|, \nu|\tau_1|)$ and $H(\nu|\bar{\eta}|, \nu|\tau_1|)$, and it is for this reason that K_3 is considered separately.

It was shown in Ref. 6 that the part of the Kernel function designated K_1 above, gives the total $1/\bar{\xi}$ contribution to the function $L(\xi)$. Clearly then, to allow accurate extraction of the $1/\bar{\xi}$ singularity, the spanwise integral involving K_1 must be evaluated accurately. In fact this integral is evaluated in double precision using an inverse hyperbolic 'stretching' transformation

$$\bar{\eta} = A^* \sinh(t) - B^* \tag{98}$$

of the type introduced in Section 3.1 of Ref. 5. The coefficients A^*, B^*, together with more detailed information on the spanwise integration, is given in Appendix A.

4.2. The Integration with Respect to ξ

From equation (74) the expression for $w_2(x_r, y_s)$ is,

$$w_2(x_r, y_s) = -\frac{1}{8\pi}\int_{-1}^{1} L(\xi)\, d\xi, \tag{99}$$

and from equation (82) it is known that $L(\xi)$ takes the form

$$L(\xi)=\frac{b_0}{\bar{\xi}}+b_1\log|\bar{\xi}|+0(\bar{\xi}\log|\bar{\xi}|)+\text{regular terms} \tag{100}$$

for $\xi\to\xi_r$ with $\xi_r\neq\xi_h$,
where

$$b_0=-2U^*(\xi_r,\eta_s)\frac{\sqrt{a(\xi_r,\eta_s)}}{g_2(\xi_r)}, \tag{101}$$

and

$$b_1=\frac{2}{\sqrt{a(\xi_r,\eta_s)}}\left\{\frac{\beta^2}{a(\xi_r,\eta_s)}\cdot\left[\frac{\partial g_1}{\partial\eta}(\xi,\eta)\right]_{\substack{\eta=\eta_s\\ \xi=\xi_r}}.U^*(\xi_r,\eta_s)+g_1(\xi_r,\eta_s)\left[\frac{\partial}{\partial\eta}U^*(\xi,\eta)\right]_{\substack{\eta=\eta_s\\ \xi=\xi_r}}+\right.$$
$$\left.+i\nu U^*(\xi_r,\eta_s).(1+g_1^2(\xi_r,\eta_s))\right\}. \tag{102}$$

Then the expression for $w_2(x_r, y_s)$ may be written in the form,

$$w_2(x_r,y_s)=-\frac{1}{8\pi}\left\{\int_{-1}^{1}\left(L(\xi)-\frac{b_0}{\bar{\xi}}-b_1\log|\bar{\xi}|\right)d\xi+b_0I_2+b_1I_3\right\}, \tag{103}$$

where

$$I_2=\oint_{-1}^{1}\frac{d\xi}{\bar{\xi}}, \tag{104}$$

and

$$I_3=\int_{-1}^{1}\log|\bar{\xi}|\,d\xi \tag{105}$$

The problem of evaluating the integrand $L(\xi)-(b_0/\bar{\xi})-b_1\log|\bar{\xi}|$ accurately for small $|\bar{\xi}|$, is resolved by the evaluation of the integral giving the $1/\bar{\xi}$ singularity in double precision (*see* Section 4.1.1), and evaluating the resulting difference over a difference in double precision to preserve accuracy. This procedure, together with the other techniques used to evaluate $w_2(x_r, y_s)$, are presented in more detail in Appendix B.

5. Use of the Method and a Discussion of the Results

The method described in the preceding sections has been programmed in Fortran IV for use with an I.B.M. 360/65 computer.

5.1. The Control Surface Program

Using the described method, the downwash $w_2(x_r, y_s)$ is evaluated at a specified set of points distributed over the starboard wing. These points are chosen to be collocation points for the Lifting-Surface calculation using the regularised downwash $w_1(x_r, y_s)$. The results reported in this section were obtained using a standard Multhopp distribution of collocation points, i.e.

$$\xi_{1_r}=-\cos\left(\frac{2r\pi}{2n+1}\right),\qquad r=1,\ldots,n, \tag{106}$$

where ξ_1 is the coordinate defined by equation (14) and

$$\eta_s=\cos\left(\frac{s\pi}{m+1}\right),\qquad s=1,\ldots,\frac{m+1}{2}\ m\text{ odd},$$
$$\frac{m}{2}\ m\text{ even}. \tag{107}$$

The order of collocation solution is determined by the parameters m, n. Thus given an m and n, the regularised downwash $w_1(x_r, y_s)$ is calculated at the collocation points and used as the boundary condition in an oscillating lifting-surface calculation. This gives a ${}_1\Delta C_p$ pressure-difference distribution, which together with the defined ${}_2\Delta C_p$ distribution enables the calculation of the total pressure-difference distribution ΔC_p through the relation

$$\Delta C_p = {}_1\Delta C_p + {}_2\Delta C_p. \tag{108}$$

From the ΔC_p distribution various integrated effects have been calculated and presented. Details of the techniques used in evaluating these integrated effects are given in Part II of this report.

5.2. Numerical Results

The following planform configurations were investigated using the procedure described in the preceding text:

(i) Wing E with an outboard distorted control surface, Fig. (3) gives details of this planform.

(ii) The N.L.R. Rectangular wing with full-span flat-plate control-surface, Fig. (8) gives details of this planform.

(iii) The N.L.R. Swept Tapered wing with an inboard control surface;

  (a) Deflected like a flat plate.

  (b) With a control surface camber mode.

  Fig. (18) gives details of this planform.

(iv) The B.A.C. Swept Tapered wing with inboard control surface deflected like a flat plate. Fig. (41) gives details of this planform.

For all but the first case the results consist of

(a) Values of the pressure difference coefficient ΔC_p.

(b) Values of the local chordwise integrals designated P_i, $i = 1, 2, 3$ where

$$P_1 = P_1' + iP_1'' = \int_{x_l}^{x_t} \Delta C_p \, dx, \tag{109}$$

$$P_2 = P_2' + iP_2'' = \int_{x_l}^{x_t} (x - x_l - c/4) \,.\, \Delta C_p \,.\, dx \tag{110}$$

and

$$P_3 = P_3' + iP_3'' = \int_{x_h}^{x_t} (x - x_h) \,.\, \Delta C_p \,.\, dx. \tag{111}$$

(c) Values of the Generalised Airforces designated Q_i, $i = 1, 2, 3$ where

$$Q_1 = Q_1' + iQ_1'' = \int_{-1}^{1} \int_{x_l}^{x_t} \Delta C_p \, dx \, d\eta, \tag{112}$$

$$Q_2 = Q_2' + iQ_2'' = \int_{-1}^{1} \int_{x_l}^{x_t} x \,.\, \Delta C_p \, dx \, d\eta \tag{113}$$

and

$$Q_3 = Q_3' + iQ_3'' = 2 \int_{\eta_{e_1}}^{\eta_{e_2}} \int_{x_h}^{x_t} (x - x_h) \,.\, \Delta C_p \,.\, dx \,.\, d\eta, \tag{114}$$

where the spanwise extent of the starboard control surface is defined by $\eta_{e_1} \leq \eta \leq \eta_{e_2}$.

5.2.1. *The results for Wing E.* The planform of this swept tapered wing is illustrated in Fig. (3), together with relevant geometrical information. The distortion on the symmetrically deflected control surfaces was defined by the equation

$$z = \bar{X} \,.\, \tfrac{1}{4} e^{\bar{X}} \, e^{\bar{Y}} \tag{115}$$

where $\bar{X} = x - x_h$, and $\bar{Y} = \eta - \eta_{e_1}$. The Mach number and reduced frequency for this case were $M = 0{\cdot}7$, $\nu = 1{\cdot}6$. This case was designed to show that the assumed loading form ${}_2\Delta C_p$ does in fact remove the main singularities in $w(x_r, y_s)$, producing a smooth regularised downwash.

Figs. 4 and 5 show plots of $w_1(x_r, y_s)$ against η along lines of constant ξ_1, and Figs. 6 and 7 show plots of $w_1(x_r, y_s)$ against ξ_1 along lines of constant η. The coordinate ξ_1 defined by equation (14), is effectively a constant percentage chord coordinate. The lines of constant ξ_1 and η are drawn on the planform of Wing E in Fig. 3. It is to be noted that the singularity in $w_1(x_r, y_s)$, at the hinge-line side-edge corner, reported in Ref. 2, is no longer apparent. The removal of this singular effect is discussed in Ref. 9. The figures show that the new loading function gives a much lower order effect at the hinge-line, side-edge corner. Overall the curves are fairly smooth, and show that the main singularities in $w(x_r, y_s)$ due to the twisted and cambered control surface, have been successfully removed.

5.2.2. *The results for the N.L.R. Rectangular Wing.* Fig. 8 illustrates this planform, and gives relevant geometrical information. The Mach number and reduced frequency for this case were $M = 0{\cdot}0$, $\nu = 1{\cdot}115$.

Using the current method two solutions were obtained using collocation orders $m = 14$, $n = 6$ and $m = 16$, $n = 8$. The aerodynamic convergence of the pressure-difference distribution, using the two solutions, is shown in Table 1. This table contains tabulated values of ΔC_p at a set of points on the planform.

The pressure results for the $m = 16$, $n = 8$ solution were then plotted against the experimental results of Hertrich (Ref. 10), and the theoretical results of N.L.R. (Ref. 3), for the spanwise stations $\eta = 0{\cdot}138$, $\eta = 0{\cdot}627$, $\eta = 0{\cdot}983$, these results are shown in Figs. 9 to 14. The comparison between the theories was good, with the experimental results showing the same trends, but at different levels. The true control-surface theories were then compared with the theoretical pressures obtained using an equivalent mode program of Davies (Ref. 4). The comparison is fairly good, with the pressures from the equivalent modes oscillating about the true control-surface-theory results, and rounding out the logarithmic peak, as one would expect.

Figs. 15 to 17 show the spanwise variation of the locally integrated effects P_1, P_2, P_3, comparing the B.A.C. and N.L.R. theories. The graphs show very good comparisons, as one would expect from the pressure comparisons.

Table 2 shows values of Q_1, Q_2, Q_3 from the current method and from the Davies Equivalent modes. The comparison is clearly very good.

5.2.3. *The results for the N.L.R. Swept Tapered Wing.* Fig. 18 illustrates this planform, and gives relevant geometrical information. The Mach number and reduced frequency for this case were $M = 0{\cdot}8$, $\nu = 0{\cdot}672$. Two control-surface modes were considered, a flat-plate mode at unit incidence, and a camber mode.

(A) *Results for the flat-plate control-surface mode at unit incidence*

As in the previous case two solutions were obtained using the current method, with $m = 14$, $n = 6$ and $m = 16$, $n = 8$. Table 3 shows the aerodynamic convergence of the pressures from the two solutions. The comparison is good, except near the trailing edge were certain discrepancies appear.

The pressure results for the $m = 16$, $n = 8$ solution were then plotted against the experimental and theoretical results of N.L.R. (Ref. 3), for the spanwise stations $\eta = 0{\cdot}45$, $\eta = 0{\cdot}55$, $\eta = 0{\cdot}64$ and $\eta = 0{\cdot}8$, these results are shown in Figs. 19 to 26.

The comparison between the theories and the experiment is seen to be fairly good. The pressure distributions from a Davies equivalent-mode calculation are also presented, and show quite good agreement with the true control-surface theories, considering the fairly low order of chordwise collocation distribution.

Figs. 27 to 29 show the spanwise variation of P_1, P_2, P_3, comparing B.A.C. theory with N.L.R. theory and experiment.

Table 4 shows values of Q_1, Q_2, Q_3 from the current method and using Davies' Equivalent modes. The real parts of the Q_i show good comparison characteristics; the imaginary parts of Q_1 and Q_2 show certain differences which it is felt are caused by cancellation effects from the chordwise integrals of $\Delta C_p''$ (*see* Figs. 20, 22, 24 and 26). This is supported by the excellent agreement for Q_3'', where only the $\Delta C_p''$ on the control surface is used.

(B) *Results for the control-surface-camber mode*

A control-surface-camber mode was defined by

$$z = (x - x_h)[1 + (x - x_h) + 2(x - x_h)^2], \tag{116}$$

and solutions were obtained for this configuration in two ways.

A direct solution of this problem was obtained using the defined camber surface, the second solution was obtained by writing

$$z = z_1 + z_2, \tag{117}$$

where

$$z_1 = x - x_h, \quad \text{and} \quad z_2 = (x - x_h)^2[1 + 2(x - x_h)], \tag{118}$$

and then treating the mode z_1 as a control-surface problem and z_2 as a regular lifting-surface problem.

Figs. 30 to 37 show that ΔC_p comparisons for the stations $\eta = 0{\cdot}45$, $\eta = 0{\cdot}55$, $\eta = 0{\cdot}64$ and $\eta = 0{\cdot}8$. The comparisons are very good, except for $\Delta C_p''$ near the leading edge, where reasonable differences may be seen. These differences are most probably due to the basic convergence of the B.A.C. control-surface theory, as applied to distorted control surfaces.

Figs. 38 to 40 show the spanwise variation of P_1, P_2, P_3 for the two methods of solution, the results show good agreement.

Table 5 shows values of Q_1, Q_2, Q_3 from the two methods, the Q_i', $i = 1, 2, 3$, and Q_3'' again show good agreement. The Q_1'' and Q_2'' show poor agreement, which may be accounted for by the cancellation effects on the chordwise integral of $\Delta C_p''$, accentuating the differences in $\Delta C_p''$ near the leading edge of the wing.

5.2.4. *The results for the B.A.C. Swept Tapered Wing.* Fig. 41 illustrates this planform, and gives relevant geometrical information. The Mach number and reduced frequency for this case were $\underline{M = 0{\cdot}5, \nu = 0{\cdot}9551}$.

Figs. 42 to 49 show comparisons of theoretical and experimental pressures, the comparison is very good for the stations over the control surface, with rather larger discrepancies for the real pressures outboard of the control surface.

Figs. 50 to 52 show the spanwise variation of P_1, P_2, P_3 for the B.A.C. theory and the N.L.R. experiment. The comparisons are good for P_1, P_2, but not so good for P_3. This may be attributed to the differences in the theoretical and experimental pressure at the trailing edge of the control surface. This difference will mainly be due to boundary-layer effects.

Table 6 compares values of Q_i, $i = 1, 2, 3$, from the current method and from the Davies' Equivalent modes technique. Good agreement is obtained between the two methods. It is to be noted that the cancellation effects involved in integrating $\Delta C_p''$ are very small, due to the fact that the point at which the $\Delta C_p''$ distribution crosses the axis has moved closer to the leading edge.

6. Conclusions

This report describes a numerical method of calculating the pressure distribution over a wing with harmonically oscillating, distorted control surfaces in subsonic flow. The applicability of the method has been assessed by treating particular planform, control-surface configurations at various Mach numbers and reduced frequencies. The results have been compared with experiment, with theoretical results from N.L.R., and with an equivalent modes technique programmed by Davies.

The aerodynamic convergence capability of the B.A.C. solution has been demonstrated, and good comparisons have been obtained with the theory and with experiment of N.L.R.

The equivalent-modes technique gives reasonable pressure comparisons with the current method, the agreement apparently improving with increasing n. The generalised forces obtained using equivalent modes compare favourably with those obtained using the B.A.C. control-surface theory.

For distorted control surfaces, accurate control-surface treatment of twist effects combined with lifting-surface calculations on the residual camber, have been shown to give good agreement with complete control-surface solutions.

LIST OF SYMBOLS

$A(x, y)$	*See* equations (31), (32), (33)
$\bar{A}$	Part width of integration region 3 (*see* Fig. 2)
A^*	*See* equation (A-36)
a	*See* equation (83)
$AG(x, y)$	*See* equation (39)
$B(x, y)$	*See* equations (43), (44), (45)
$\bar{B}$	Part width of integration region 3 (*see* Fig. 2)
B^*	*See* equation (A-37)
b_0	*See* equation (101)
b_1	*See* equation (102)
$C(x, y)$	*See* equations (50), (51), (52)
$\bar{C}(x, y)$	*See* equation (47)
c	Local chord of the wing
c_1	Local chord of the control surface
c_2	$c - c_1$
D	*See* equation (56)
$E(x, y)$	*See* equations (53), (54), (55)
$F(\bar{X}, \bar{Y})$	Defines the control surface distortion mode. *See* equation (19)
$\bar{F}(x, y)$	*See* equation (36)
G	Numeric function used in the definition of the Kernel function. *See* equation (75)
$\bar{G}$	See equation (46)
G^*	*See* equation (96)
$g(\xi, \eta)$	*See* equation (68)
$g_1(\xi, \eta)$	*See* equation (70)
$g_2(\xi)$	*See* equation (71)
H	Numeric function used in the definition of the Kernel function. *See* equation (75)
$H_1(y)$	*See* equation (48)
$J(\xi, \eta)$	Jacobean of the transformation to the (ξ, η) coordinate system. *See* equation (60)
$K(X, Y; M, \nu)$	The Kernel function. *See* equation (8)
$\bar{K}(\bar{\xi}, \bar{\eta}; M, \nu)$	The transformed Kernel function. *See* equation (75)
$\bar{\bar{K}}(\bar{\xi}, \bar{\eta}; M, \nu)$	*See* equations (76), (77), (78), (79)
$K_1(\bar{\xi}, \bar{\eta}; M, \nu)$	*See* equation (88)
$K_2(\bar{\xi}, \bar{\eta}; M, \nu)$	*See* equations (89), (90)
$K_3(\bar{\xi}, \bar{\eta}; M, \nu)$	*See* equation (91)
$\bar{K}_3(\bar{\xi}, \bar{\eta}; M, \nu)$	*See* equations (92), (93), (94), (95)
$L(\xi)$	The spanwise integral, *see* equation (73)
$\bar{L}(\xi)$	*See* equation (81)
M	Mach number
m	Spanwise collocation order
$N(\bar{\xi}, \bar{\eta}; M, \nu)$	*See* equation (80)
n	Chordwise collocation order
$\bar{P}(x, y)$	*See* equation (34)
P_1	*See* equation (109)
P_2	*See* equation (110)
P_3	*See* equation (111)
$p(x, y)$	Used to define ${}_2\Delta C_p$. *See* equation (22)
$p_1(x, y)$	*See* equation (24)
$p_2(x, y)$	*See* equation (37)
$p_3(x, y)$	*See* equation (49)
p_l	Lower-surface pressure on the aerofoil
p_u	Upper-surface pressure on the aerofoil
Q_1	*See* equation (112)
Q_2	*See* equation (113)
Q_3	*See* equation (114)
R	*See* equation (9)

$R^*(\xi_1, \eta)$	*See* equation (12)
R_e	*See* equation (28)
R_p	*See* equation (25)
R_t	*See* equation (38)
S	The projected wing planform in the plane $z=0$
$S^*(x, y)$	*See* equation (40)
s	Semi-span
t	Time variable
U	Free-stream velocity
$U^*(\xi, \eta)$	${}_2\Delta C_p(x, y) . J(\xi, \eta)$
$w(x, y)$	Downwash on the aerofoil. *See* equation (1)
$w_1(x, y)$	The regularised downwash. *See* equation (57)
$w_2(x, y)$	*See* equation (57)
X	$x_r - x$
$\bar{X}$	$x - x_h$
X_1	*See* equation (18)
x	Cartesian coordinate in the free-stream direction
$x_h(y)$	Equation of the hinge line
$x_l(y)$	Equation of leading edge of the wing
x_r	Streamwise coordinate of collocation station
$x_t(y)$	Equation of trailing edge of the wing
Y	$y - y_s$
$\bar{Y}$	$y - y_e = \eta - \eta_e$
y	Cartesian coordinate in spanwise direction
y_e	Side edge of the control surface
y_s	Spanwise coordinate of collocation station
y_2	*See* equation (48)
z	Cartesian coordinate measured positive downwards
β	$\sqrt{1-M^2}$
$\bar{\beta}$	*See* equation (29)
$\bar{\bar{\beta}}$	*See* equation (26)
$\Delta C_p(x, y)$	Loading distribution over wing and control surface
${}_1\Delta C_p(x, y)$	Regular contribution to $\Delta C_p(x, y)$
${}_2\Delta C_p(x, y)$	Singular contribution to $\Delta C_p(x, y)$
ζ	*See* equation (9)
η	y/s
η_e	Coordinate of side edge of the control surface
η_{e_1}, η_{e_2}	Coordinates of side edges of the control surface
η_s	Spanwise coordinate of collocation station
$\bar{\eta}$	$\eta_s - \eta$
κ_0	$x'_h(y_e)$
κ_t	$x'_t(y_e)$
ν	Reduced frequency, based on semi-span $\dfrac{\omega . s}{U}$
ξ	*See* equation (17)
ξ_1	*See* equation (14)
ξ_h	Hinge line coordinate in the (ξ, η) coordinate system
ξ_r	ξ-wise coordinate of collocation station
$\underline{\xi_1}$	*See* equation (35)
$\bar{\xi}$	$\xi_r - \xi$
ρ	Free-stream density
τ_1	*See* equation (9)
ω	Frequency of oscillation

REFERENCES

No.	*Author(s)*	*Titles, etc.*
1	M. T. Landahl	On the pressure loading functions for oscillating wings with control surfaces Proc. A.I.A.A./A.S.M.E. 8th Structures, Structural Dynamics and Materials Conference, Palm Springs, March, 1967
2	W. R. Marchbank, J. M. R. Kennelly and B. L. Hewitt	The evaluation of pressure distributions on wings with control surfaces in subsonic flow B.A.C. Preston Divn. Report Ae 311, Nov. 1970
3	R. J. Zwaan	On a Kernel-Function method for the calculation of pressure distributions on wings with harmonically oscillating control surfaces in subsonic flow N.L.R. TR/70123U March 1971
4	D. E. Davies	Calculation of unsteady airforces on a thin wing oscillating harmonically in subsonic flow Structures Report 290, August 1963
5	B. L. Hewitt and W. E. R. Kellaway	A new treatment of the subsonic lifting surface problem using curvilinear coordinates Part I: Details of the method as applied to regular surfaces with finite tip chords and a preliminary set of numerical results B.A.C. (M.A.D.) Ae 290, Part I, August 1968
6	R. Blanchfield and W. E. R. Kellaway	Subsonic oscillating lifting surface theory B.A.C. (M.O.D.) Program S17 User Manual (To be published)
7	R. Dat and J. Malfois	Calculating the Kernel of the lifting surface integral equation in unsteady subsonic flow La Recherche Aérospatiale, 1970, Number 5 (Sept.–Oct.), pages 251 to 259
8	B. L. Hewitt	Special loading functions for treating wings with control surfaces in unsteady, subsonic flow B.A.C. (M.A.D.) Ae 345 (To be published)
9	T. G. Wigley and B. L. Hewitt	The evaluation of a loading form for the calculation of linearised theory pressure distributions on wings with control surfaces having swept hinge lines in steady subsonic flow B.A.C. (M.A.D.) Ae 344, March 1973
10	H. Hertrich	Zur experimentellen Bestimmung der aerodynamischen Reaktionen an schwingenden Halbflügelmodellen im Unterschall-Windkanal Teil III: Messingen an einem Rechteckflügel mit Ruder. A.V.A. A. Bericht 66 J 08 (1967)

APPENDIX A

An Evaluation of the Spanwise Integral $L(\xi)$

From equation (73)

$$L(\xi) = \int_{-1}^{1} U^*(\xi, \eta) \,.\, \bar{K}(\bar{\xi}, \bar{\eta}; M, \nu)\, d\eta, \tag{A-1}$$

where

$$U^*(\xi, \eta) = {}_2\Delta C_p(x, y) \,.\, J(\xi, \eta). \tag{A-2}$$

Using the subdivision into three regions, introduced in Section 4.1, $L(\xi)$ may be written in the form

$$L(\xi) = L_1(\xi) + L_2(\xi) + L_3(\xi), \tag{A-3}$$

where

$$L_1(\xi) = \int_{-1}^{\eta_s - \bar{A}} U^*(\xi, \eta) \,.\, \bar{K}(\bar{\xi}, \bar{\eta}; M, \nu)\, d\eta, \tag{A-4}$$

$$L_2(\xi) = \int_{\eta_s + \bar{B}}^{1} U^*(\xi, \eta) \,.\, \bar{K}(\bar{\xi}, \bar{\eta}; M, \nu)\, d\eta, \tag{A-5}$$

and

$$L_3(\xi) = \int_{\eta_s - \bar{A}}^{\eta_s + \bar{B}} U^*(\xi, \eta) \,.\, \bar{K}(\bar{\xi}, \bar{\eta}; M, \nu)\, d\eta. \tag{A-6}$$

A.1. The Numerical Evaluation of $L_1(\xi)$, $L_2(\xi)$

The Kernel function is regular over regions (1) and (2), that is the range of integration of $L_1(\xi)$ and $L_2(\xi)$ respectively, However, the loading function $U^*(\xi, \eta)$ exhibits the following behaviour,

$$\begin{aligned} U^*(\xi, \eta) &\sim \sqrt{1-\eta} \qquad \text{for} \quad \eta \to 1, \\ &\sim \sqrt{1+\eta} \qquad \text{for} \quad \eta \to -1, \end{aligned}$$

and using equation (24) it may be shown that for the case of either non-zero frequency, or of camber on the control surface

$$\begin{aligned} U^*(\xi, \eta) &\sim (\eta - \eta_e) \log|\eta - \eta_e| \qquad \text{for} \quad \eta \to \eta_e, \\ &\sim (\eta + \eta_e) \log|\eta + \eta_e| \qquad \text{for} \quad \eta \to -\eta_e \end{aligned} \tag{A-7}$$

Clearly some account must be taken of these singularities in order to obtain quadrature convergence. The relative positions of η_s, η_e, $-\eta_e$ will obviously effect the quadrature technique used. Consider the most general case where $-1 \leqslant -\eta_e \leqslant \eta_s - \bar{A}$, and $\eta_s + \bar{B} \leqslant \eta_e \leqslant 1$, then

$$L_1(\xi) = L_{11}(\xi) + L_{12}(\xi), \tag{A-8}$$

where

$$L_{11}(\xi) = \int_{-1}^{-\eta_e} U^*(\xi, \eta) \,.\, \bar{K}\, d\eta, \tag{A-9}$$

$$L_{12}(\xi) = \int_{-\eta_e}^{\eta_s - \bar{A}} U^*(\xi, \eta) \,.\, \bar{K}\, d\eta, \tag{A-10}$$

and $\bar{K}$ represents the Kernel function $\bar{K}(\bar{\xi}, \bar{\eta}; M, \nu)$.
Also

$$L_2(\xi) = L_{21}(\xi) + L_{22}(\xi), \tag{A-11}$$

where

$$L_{21}(\xi) = \int_{\eta_s+\bar{B}}^{\eta_e} U^*(\xi, \eta) \,.\, \bar{K} \, d\eta, \tag{A-12}$$

and

$$L_{22}(\xi) = \int_{\eta_e}^{1} U^*(\xi, \eta) \,.\, \bar{K} \, d\eta. \tag{A-13}$$

This 'split range' technique proved adequate for the relatively weak singular form $(\eta - \eta_e) \log |\eta - \eta_e|$.

The integrals $L_{12}(\xi)$, $L_{21}(\xi)$ may be evaluated using Gauss–Legendre quadratures after making a normalising transformation of the form

$$\eta = \tfrac{1}{2}(\eta_u - \eta_l) \,.\, v + \tfrac{1}{2}(\eta_u + \eta_L), \tag{A-14}$$

where η_u and η_l are the upper and lower limits of the integrals concerned.

Consider next the evaluation of $L_{22}(\xi)$. After application of a normalising transformation of the form

$$\eta = (\eta_u - \eta_l)v + \eta_l \tag{A-15}$$

the integral becomes

$$L_{22}(\xi) = (1 - \eta_e) \int_0^1 \frac{U^*(\xi, \eta)}{\sqrt{1-v}} \,.\, \bar{K} \,.\, \sqrt{1-v} \, dv, \tag{A-16}$$

where use has been made of the fact that $U^*(\xi, \eta) \sim \sqrt{1-\eta}$ as $\eta \to 1$ thus $U^*(\xi, \eta) \sim \sqrt{1-v}$ as $v \to 1$.

In this form $L_{22}(\xi)$ may be evaluated using Gauss–Root quadratures. Now Gauss–Root quadratures take the form

$$\int_0^1 V(v)\sqrt{1-v} = \sum_{k=1}^{NQ} 2 \,.\, v_{k\,2.NQ+1}^2 W_k V(1 - v_k^2) \tag{A-17}$$

where NQ is the Gauss–Root quadrature order, $v_{k,\ 2.NQ+1} W_k$ are the kth positive root and weight of a $(2\,.\,NQ + 1)$th Gauss–Legendre quadrature.

Application of this to equation (A-16) gives

$$L_{22}(\xi) = \sum_{k=1}^{NQ} 2 \,.\, v_{k\ 2.NQ+1} W_k \,.\, V(1 - v_k^2), \tag{A-18}$$

where

$$V(v) = (1 - \eta_e) \,.\, U^*(\xi, \eta) \,.\, \bar{K}. \tag{A-19}$$

Note that functions of the form $U^*(\xi, \eta)/\sqrt{1-v}$ do not require evaluation.

The evaluation of $L_{11}(\xi)$ proceeds in a similar fashion.

The valuation technique described above for the case $-1 \leqslant -\eta_e \leqslant \eta_s - \bar{A}$ and $\eta_s + \bar{B} \leqslant \eta_e \leqslant 1$, may be applied to the other cases that arise.

A.2. The Numerical Evaluation of $L_3(\xi)$

From equation (A-6)

$$L_3(\xi) = \int_{\eta_s - \bar{A}}^{\eta_s + \bar{B}} U^*(\xi, \eta) \,.\, \bar{K} \, d\eta, \tag{A-20}$$

and using equation (87) this may be re-written as

$$L_3(\xi) = L_{31}(\xi) + L_{32}(\xi) + L_{33}(\xi), \tag{A-21}$$

where

$$L_{31}(\xi) = \int_{\eta_s - \bar{A}}^{\eta_s + \bar{B}} U^*(\xi, \eta) \,.\, K_1 \, d\eta, \tag{A-22}$$

$$L_{32}(\xi) = -\!\!\!\!\!\!\int_{\eta_s - \bar{A}}^{\eta_s + \bar{B}} U^*(\xi, \eta) \,.\, K_2 \, d\eta, \tag{A-23}$$

$$L_{33}(\xi) = \int_{\eta_s - \bar{A}}^{\eta_s + \bar{B}} U^*(\xi, \eta) \,.\, K_3 \, d\eta, \tag{A-24}$$

and

$$K_i = K_i(\bar{\xi}, \bar{\eta}; M, \nu) \qquad i = 1, 2, 3. \tag{A-25}$$

The evaluation of $L_{31}(\xi)$ and $L_{33}(\xi)$

(A) *For $|\bar{\xi}|$ not small*

For $|\bar{\xi}|$ not too small the functions K_1 and K_2 are regular, so that $L_{31}(\xi)$ and $L_{33}(\xi)$ may be evaluated by using the Gauss quadrature technique described in the previous section on the evaluation of $L_1(\xi)$ and $L_2(\xi)$. The exact methods used depend upon whether

$$\eta_s + \bar{B} = 1 \qquad\qquad \textit{or} \quad \eta_s + \bar{B} \neq 1,$$

and whether

$$\eta_s - \bar{A} < \eta_e < \eta_s + \bar{B} \qquad \textit{or} \quad \eta_e \leqslant \eta_s - \bar{A},\ \eta_e \geqslant \eta_s + \bar{B}.$$

(B) *For $|\bar{\xi}|$ small*

For $|\bar{\xi}|$ small the functions K_1 and K_2 are very irregular, this irregularity is 'stretched' out using the inverse hyperbolic transformation introduced in Ref. 5.

Formulation of the inverse hyperbolic stretching transformation

From equation (69)

$$X = g_1(\xi, \eta) \,.\, \bar{\eta} + g_2(\xi) \,.\, \bar{\xi}, \tag{A-26}$$

introduce u through

$$\bar{\eta} = -|\bar{\xi}| \,.\, u, \tag{A-27}$$

then

$$X = \bar{\xi} \,.\, X^*, \tag{A-28}$$

where

$$X^* = g_2(\xi) - g_1(\xi, \eta) \operatorname{sgn}(\bar{\xi}) \,.\, u. \tag{A-29}$$

Now

$$\begin{aligned} R &= \sqrt{X^2 + \beta^2 \bar{\eta}^2}, \\ &= |\bar{\xi}| R^*, \end{aligned} \tag{A-30}$$

where

$$R^* = \sqrt{X^{*2} + \beta^2 u^2}. \tag{A-31}$$

It may be shown that

$$R^* = \frac{1}{\sqrt{a(\xi, \eta)}} [\{a(\xi, \eta)u - g_2(\xi) \,.\, g_1(\xi, \eta) \operatorname{sgn}(\bar{\xi})\}^2 + \beta^2 g_2^2(\xi)]^{\frac{1}{2}}, \tag{A-32}$$

where

$$a(\xi, \eta) = \beta^2 + g_1^2(\xi, \eta). \tag{A-33}$$

This expression for R^* defines the required stretching transformation to be

$$u = \frac{g_2(\xi)}{a(\xi, \eta_s)} \{\beta \,.\, \sinh(t) + g_1(\xi, \eta_s) \operatorname{sgn}(\bar{\xi})\}. \tag{A-34}$$

Using equation (A-27) the total transformation may be written in the form

$$\bar{\eta} = A^* \sinh(t) + B^*, \tag{A-35}$$

where

$$A^* = \frac{-|\bar{\xi}| \,.\, g_2(\xi) \,.\, \beta}{a(\xi, \eta_s)}, \tag{A-36}$$

and

$$B^* = \frac{-\bar{\xi} g_1(\xi, \eta_s) \,.\, g_2(\xi)}{a(\xi, \eta_s)}. \tag{A-37}$$

Consider limits of integration in the η plane, η_l and η_u where $\eta_l \leqslant \eta_s \leqslant \eta_u$, then under the transformation (A-35)

η_l gives t_1 say,

and

η_u gives t_2 where,

$$t_1 = -\log\left(\frac{\bar{t}_1}{\beta|\bar{\xi}|}\right), \qquad t_2 = \log\left(\frac{\bar{t}_2}{\beta|\bar{\xi}|}\right), \tag{A-38}$$

$$\bar{t}_i = \bar{\bar{t}}_i + \sqrt{\bar{\bar{t}}_i^2 + \beta^2 \bar{\xi}^2}, \qquad i = 1, 2, \tag{A-39}$$

$$\bar{\bar{t}}_1 = \frac{a(\xi, \eta_s)}{g_2(\xi)} (\eta_s - \eta_l) + g_1(\xi, \eta_s) \,.\, \bar{\xi} \tag{A-40}$$

and

$$\bar{\bar{t}}_2 = \frac{a(\xi, \eta_s)}{g_2(\xi)} (\eta_u - \eta_s) - g_1(\xi, \eta_s) \,.\, \bar{\xi}. \tag{A-41}$$

The evaluation of $L_{33}(\xi)$

$L_{33}(\xi)$ is evaluated using Gaussian quadratures after splitting the range at η_e if $\eta_s - \bar{A} < \eta_e < \eta_s + \bar{B}$, and applying the stretching defined above. If $\eta_s + \bar{B} = 1$, then the root zero behaviour is taken into account after the stretching transformation, in the manner described in the first section of this Appendix.

The evaluation of $L_{31}(\xi)$

Since this integral gives the total $1/\bar{\xi}$ contribution to $L(\xi)$, it is evaluated in double precision. This then allows the accurate extraction of the $1/\bar{\xi}$ term for very small $|\bar{\xi}|$.

The inverse hyperbolic stretching is applied to the integral $L_{31}(\xi)$, which is then split into N intervals. In each of these intervals a 16th order double precision Gauss–Legendre quadrature is used, if $\eta_s+\bar{B}=1$ then the transformation

$$\sqrt{1-t}=v \tag{A-42}$$

is used to remove the infinite slope of the integrand in the interval with end point corresponding to $\eta_s+\bar{B}=1$.

This technique has been shown to work very well for values of $|\bar{\xi}|>10^{-6}$.

The evaluation of $L_{32}(\xi)$

$$L_{32}(\xi)=\int_{\eta_s-\bar{A}}^{\eta_s+\bar{B}} U^*(\xi,\eta)\,.\,K_2\,d\eta \tag{A-43}$$

where from equations (89) and (90),

$$K_2=0 \quad \text{for} \quad \bar{\xi}\leqslant 0, \tag{A-44}$$

$$K_2=\left(\frac{2}{\bar{\eta}^2}+\nu^2\log|\bar{\eta}|\right)(\cos\nu X-i\sin\nu X) \quad \text{for} \quad \bar{\xi}>0. \tag{A-45}$$

Consider the non-trivial case of $\bar{\xi}>0$, then

$$L_{32}(\xi)=\int_{\eta_s-\bar{A}}^{\eta_s+\bar{B}} \frac{\bar{U}(\xi,\eta)}{\bar{\eta}^2}\,.\,(2+\nu^2\bar{\eta}^2\log|\bar{\eta}|)\,d\eta, \tag{A-46}$$

where

$$\bar{U}(\xi,\eta)=U^*(\xi,\eta)\,.\,(\cos\nu X-i\sin\nu X). \tag{A-47}$$

An expansion of $\bar{U}(\xi,\eta)$ about η_s gives

$$L_{32}(\xi)=L_{321}(\xi)+L_{322}(\xi)+L_{323}(\xi), \tag{A-48}$$

where

$$L_{321}(\xi)=\int_{\eta_s-\bar{A}}^{\eta_s+\bar{B}} \frac{\bar{U}(\xi,\eta)-\bar{U}(\xi,\eta_s)+\bar{\eta}\bar{U}'(\xi,\eta_s)}{\bar{\eta}^2}(2+\nu^2\bar{\eta}^2\log|\bar{\eta}|)\,d\eta \tag{A-49}$$

$$L_{322}(\xi)=\bar{U}(\xi,\eta_s)\int_{\eta_s-\bar{A}}^{\eta_s+\bar{B}} \frac{1}{\bar{\eta}^2}\,.\,(2+\nu^2\bar{\eta}^2\log|\bar{\eta}|)\,d\eta, \tag{A-50}$$

$$L_{323}(\xi)=-\bar{U}'(\xi,\eta_s)\oint_{\eta_s-\bar{A}}^{\eta_s+\bar{B}} (2+\nu^2\bar{\eta}^2\log|\bar{\eta}|)\frac{d\eta}{\bar{\eta}}, \tag{A-51}$$

and

$$\bar{U}'(\xi,\eta_s)=\left[\left(\frac{\partial\bar{U}}{\partial\eta}\right)_\xi\right]_{\eta=\eta_s} \tag{A-52}$$

$L_{322}(\xi)$, $L_{323}(\xi)$ may be evaluated analytically to give

$$L_{322}(\xi)=\bar{U}(\xi,\eta_s)\left[-2\left(\frac{1}{\bar{B}}+\frac{1}{\bar{A}}\right)+\nu^2(\bar{B}\log\bar{B}+\bar{A}\log\bar{A}-\bar{B}-\bar{A})\right], \tag{A-53}$$

and

$$L_{323}(\xi)=\bar{U}'(\xi,\eta_s)\left[2\log\left(\frac{\bar{B}}{\bar{A}}\right)+\frac{\nu^2}{2}\left\{\bar{B}^2\log\bar{B}-\bar{A}^2\log\bar{A}+\frac{1}{2}(\bar{A}^2-\bar{B}^2)\right\}\right]. \tag{A-54}$$

The integral $L_{321}(\xi)$ may be evaluated using the Gaussian quadrature techniques described earlier in this section, if the integrand can be accurately evaluated. The function $[\bar{U}(\xi, \eta)-\bar{U}(\xi, \eta_s)+\bar{\eta}\bar{U}'(\xi, \eta_s)]/\bar{\eta}^2$ is evaluated in double precision to ensure accuracy as $\bar{\eta} \to 0$. By splitting the range of integration at $\bar{\eta}=0$, that is $\eta = \eta_s$, the difference over difference is never evaluated for $\bar{\eta}=0$, since Gaussian quadrature points do not coincide with the end points of the range.

APPENDIX B

The Integration with Respect to ξ

From equation (103)

$$w_2(x_r, y_s) = -\frac{1}{8\pi}\{I_1 + b_0 I_2 + b_1 I_3\}, \tag{B-1}$$

where

$$I_1 = \int_{-1}^{1} \left(L(\xi) - \frac{b_0}{\bar{\xi}} - b_1 \log|\bar{\xi}|\right) d\xi, \tag{B-2}$$

$$I_2 = \oint_{-1}^{1} \frac{d\xi}{\bar{\xi}}, \tag{B-3}$$

and

$$I_3 = \int_{-1}^{1} \log|\bar{\xi}|\, d\xi. \tag{B-4}$$

I_2 and I_3 may be evaluated analytically to give

$$I_2 = -\log\left(\frac{1-\xi_r}{1+\xi_r}\right), \tag{B-5}$$

$$I_3 = (1-\xi_r)\log(1-\xi_r) + (1+\xi_r)\log(1+\xi_r) - 2 \tag{B-6}$$

The evaluation of I_1

$$I_1 = \int_{-1}^{1} S(\xi)\, d\xi, \tag{B-7}$$

where

$$S(\xi) = L(\xi) - \frac{b_0}{\bar{\xi}} - b_1 \log|\bar{\xi}|. \tag{B-8}$$

The term in $L(\xi)$ giving the $1/\bar{\xi}$ content is $L_{31}(\xi)$, as defined in Appendix A, and this is evaluated in double precision so that $b_0/\bar{\xi}$ may be accurately extracted. The function $S(\xi)$ has the following form

$$\begin{aligned} S(\xi) &\sim \sqrt{1-\xi} \quad \text{for} \quad \xi \to 1, \\ &\sim \sqrt{1+\xi} \quad \text{for} \quad \xi \to -1, \\ &\sim \bar{\xi}\log\bar{\xi} \quad \text{for} \quad \bar{\xi} \to 0, \\ &\sim \log|\xi - \xi_h| \quad \text{for} \quad \xi \to \xi_h. \end{aligned} \tag{B-9}$$

In order to evaluate I_1 parameters δ_1, δ_2, δ_3 are introduced, and I_1 written as

$$I_1 = I_{11} + I_{12} + I_{13} + I_{14} + I_{15} + I_{16}, \tag{B-10}$$

where

$$I_{11} = \int_{-1}^{-1+\delta_1} S(\xi)\, d\xi, \tag{B-11}$$

$$I_{12} = \int_{-1+\delta_1}^{\xi_h - \delta_2} S(\xi)\, d\xi, \tag{B-12}$$

$$I_{13} = \int_{\xi_h - \delta_2}^{\xi_h} S(\xi)\, d\xi, \tag{B-13}$$

$$I_{14} = \int_{\xi_h}^{\xi_h + \delta_2} S(\xi)\, d\xi, \tag{B-14}$$

$$I_{15} = \int_{\xi_h + \delta_2}^{1-\delta_3} S(\xi)\, d\xi, \tag{B-15}$$

and

$$I_{16} = \int_{1-\delta_3}^{1} S(\xi)\, d\xi. \tag{B-16}$$

I_{11} and I_{16} may be evaluated using Gauss–Root quadrature after using the appropriate normalising transformation. I_{12} and I_{15} may be evaluated using Gauss–Legendre quadratures after normalising the range of integration.

Consider the evaluation of I_{13},

$$I_{13} = \int_{\xi_h - \delta_2}^{\xi_h} S(\xi)\, d\xi, \tag{B-17}$$

where

$$S(\xi) \sim \log|\xi - \xi_h| \quad \text{for} \quad \xi \to \xi_h.$$

Assume a transformation of the form

$$\begin{aligned} v^2 &= \xi_h - \xi, \\ 2v\, dv &= -d\xi, \end{aligned} \tag{B-18}$$

then

$$I_{13} = -2 \int_{\sqrt{\delta_2}}^{0} S(\xi)\, v\, dv. \tag{B-19}$$

Now the $\log|\xi - \xi_h|$ variation in $S(\xi)$ is transformed into $2 \log|v|$ so that

$$S(\xi) \,.\, v \sim v \log|v| \quad \text{as} \quad v \to 0,$$

and since $v = 0$ is an end point of the range this integral may be evaluated using Gauss–Legendre quadratures. Clearly the integral I_{14} may be evaluated similarly.

The values of the parameters δ_1, δ_2, δ_3 are determined through numerical experimentation. For swept wings with η_s stations close to the centre line, a very irregular behaviour of $L(\xi)$ across $\xi = \xi_r$ was noticed. By appropriate choice of one of the parameters δ_1, δ_2, δ_3 a split in the integration range at ξ_r was achieved, this improved the convergence properties of I_1.

TABLE 1

The Aerodynamic Convergence of the ΔC_p Distribution obtained for the N.L.R. Rectangular Wing $M=0{\cdot}0$, $\nu=1{\cdot}115$

Real Pressures

$(x-x_l)/c$	$\Delta C_p'$ at $\eta=0{\cdot}138$		$\Delta C_p'$ at $\eta=0{\cdot}627$		$\Delta C_p'$ at $\eta=0{\cdot}983$	
	$m=14$ $n=6$	$m=16$ $n=8$	$m=14$ $n=6$	$m=16$ $n=8$	$m=14$ $n=6$	$m=16$ $n=8$
0·02	2·847	2·857	2·118	2·131	0·483	0·519
0·1	1·560	1·539	1·164	1·136	0·232	0·192
0·24	1·397	1·432	1·043	1·091	0·199	0·215
0·34	1·567	1·570	1·225	1·226	0·250	0·269
0·44	1·861	1·832	1·521	1·475	0·320	0·309
0·54	2·317	2·318	1·970	1·970	0·427	0·424
0·64	3·370	3·425	3·023	3·104	0·820	0·859
0·68	4·700	4·761	4·362	4·449	1·683	1·728
0·72	4·651	4·701	4·329	4·397	1·681	1·717
0·76	3·215	3·236	2·918	2·942	0·812	0·824
0·84	2·015	1·963	1·797	1·716	0·428	0·378
0·94	0·944	0·931	0·792	0·816	0·166	0·178
0·98	0·443	0·499	0·226	0·365	−0·032	0·053

Imaginary Pressures

$(x-x_l)/c$	$\Delta C_p''$ at $\eta=0{\cdot}138$		$\Delta C_p''$ at $\eta=0{\cdot}627$		$\Delta C_p''$ at $\eta=0{\cdot}983$	
	$m=14$ $n=6$	$m=16$ $n=8$	$m=14$ $n=6$	$m=16$ $n=8$	$m=14$ $n=6$	$m=16$ $n=8$
0·02	−0·778	−0·763	−0·554	−0·538	−0·133	−0·126
0·1	−0·194	−0·200	−0·123	−0·153	−0·029	−0·028
0·24	0·072	0·084	0·051	0·082	0·015	0·030
0·34	0·212	0·215	0·181	0·185	0·039	0·028
0·44	0·358	0·346	0·316	0·286	0·062	0·038
0·54	0·528	0·525	0·462	0·454	0·102	0·103
0·64	0·769	0·790	0·678	0·716	0·181	0·213
0·68	0·934	0·959	0·838	0·883	0·240	0·271
0·72	1·238	1·260	1·144	1·181	0·395	0·416
0·76	1·380	1·392	1·293	1·308	0·458	0·459
0·84	1·433	1·414	1·376	1·336	0·530	0·489
0·94	1·039	1·039	0·992	1·012	0·414	0·432
0·98	0·598	0·628	0·491	0·571	0·188	0·255

TABLE 2

Comparison of the Generalised Airforces Q_i, $i = 1, 2, 3$ for the N.L.R. Rectangular Wing $M = 0{\cdot}0$, $\nu = 1{\cdot}115$

$$Q_1 = Q_1' + iQ_1'' = \int_{-1}^{1} \int_{x_l}^{x_t} \Delta C_p \, dx \, d\eta,$$

$$Q_2 = Q_2' + iQ_2'' = \int_{-1}^{1} \int_{x_l}^{x_t} x \, . \, \Delta C_p \, dx \, d\eta,$$

$$Q_3 = Q_3' + iQ_3'' = 2 \int_{\eta_{e_1}}^{\eta_{e_2}} \int_{x_h}^{x_t} (x - x_h) \, . \, \Delta C_p \, dx \, d\eta.$$

Real Part

Q_i'	B.A.C. $m = 14$ $n = 6$	Davies $m = 12$ $n = 10$	Davies $m = 8$ $n = 15$
Q_1'	2·964	2·964	2·95
Q_2'	1·269	1·268	1·263
Q_3'	0·0694	0·0708	0·0698

Imaginary Part

Q_i''	B.A.C. $m = 14$ $n = 6$	Davies $m = 12$ $n = 10$	Davies $m = 8$ $n = 15$
Q_1''	0·724	0·734	0·715
Q_2''	0·485	0·488	0·477
Q_3''	0·0589	0·0591	0·0571

TABLE 3

The Aerodynamic Convergence of the ΔC_p Distribution obtained for the N.L.R. Swept Tapered Wing with a Flat-Plate Flap at Unit Incidence $M = 0{\cdot}8$, $\nu = 0{\cdot}672$

Real Pressures

$(x-x_l)/c$	$\Delta C'_p$ at $\eta = 0{\cdot}45$		$\Delta C'_p$ at $\eta = 0{\cdot}55$		$\Delta C'_p$ at $\eta = 0{\cdot}64$		$\Delta C'_p$ at $\eta = 0{\cdot}8$	
	$m = 14$, $n = 6$	$m = 16$, $n = 8$	$m = 14$, $n = 6$	$m = 16$, $n = 8$	$m = 14$, $n = 6$	$m = 16$, $n = 8$	$m = 14$, $n = 6$	$m = 16$, $n = 8$
0·02	−0·345	−0·345	−0·232	−0·244	−0·065	−0·072	0·394	0·429
0·06	−0·075	−0·082	0·042	0·040	0·186	0·194	0·510	0·532
0·14	0·181	0·209	0·347	0·382	0·513	0·542	0·750	0·737
0·26	0·616	0·613	0·821	0·800	0·967	0·934	0·997	0·958
0·34	0·998	0·985	1·177	1·157	1·257	1·234	1·094	1·079
0·48	1·804	1·787	1·835	1·817	1·533	1·529	1·154	1·157
0·6	2·643	2·581	2·443	2·331	2·097	1·970	1·116	1·040
0·7	3·941	3·852	3·371	3·217	2·301	2·138	0·812	0·732
0·74	5·979	5·893	5·149	5·016	1·863	1·732	0·635	0·583
0·76	5·794	5·714	4·650	4·535	1·473	1·366	0·549	0·516
0·8	3·101	3·036	1·968	1·900	1·034	0·987	0·400	0·407
0·84	1·957	1·908	1·199	1·176	0·717	0·738	0·284	0·321
0·9	0·970	0·919	0·604	0·585	0·399	0·400	0·178	0·194
0·94	0·586	0·507	0·405	0·319	0·312	0·221	0·185	0·124
0·98	0·444	0·342	0·407	0·248	0·395	0·206	0·345	0·208

Imaginary Pressures

$(x-x_l)/c$	$\Delta C''_p$ at $\eta = 0{\cdot}45$		$\Delta C''_p$ at $\eta = 0{\cdot}55$		$\Delta C''_p$ at $\eta = 0{\cdot}64$		$\Delta C''_p$ at $\eta = 0{\cdot}8$	
	$m = 14$, $n = 6$	$m = 16$, $n = 8$	$m = 14$, $n = 6$	$m = 16$, $n = 8$	$m = 14$, $n = 6$	$m = 16$, $n = 8$	$m = 14$, $n = 6$	$m = 16$, $n = 8$
0·02	−0·859	−0·857	−1·107	−1·134	−1·353	−1·357	−1·744	−1·675
0·06	−0·721	−0·657	−0·859	−0·772	−0·989	−0·906	−1·122	−1·012
0·14	−0·660	−0·603	−0·733	−0·655	−0·759	−0·698	−0·645	−0·624
0·26	−0·719	−0·714	−0·668	−0·686	−0·571	−0·600	−0·271	−0·272
0·34	−0·700	−0·666	−0·560	−0·555	−0·404	−0·403	−0·080	−0·065
0·48	−0·394	−0·331	−0·169	−0·117	−0·183	−0·142	0·098	0·107
0·6	0·150	0·123	0·339	0·274	0·453	0·363	0·430	0·387
0·7	0·786	0·714	0·885	0·747	0·846	0·701	0·488	0·473
0·74	1·135	1·081	1·181	1·062	0·963	0·844	0·463	0·470
0·76	1·421	1·383	1·402	1·304	0·966	0·872	0·439	0·459
0·8	1·626	1·629	1·436	1·394	0·879	0·845	0·376	0·414
0·84	1·617	1·656	1·321	1·336	0·746	0·770	0·300	0·343
0·9	1·403	1·433	1·075	1·102	0·539	0·571	0·200	0·209
0·94	1·182	1·135	0·900	0·844	0·438	0·385	0·178	0·137
0·98	0·878	0·746	0·704	0·543	0·412	0·253	0·244	0·165

TABLE 4

Comparison of the Generalised Airforces Q_i, $i = 1, 2, 3$ for the N.L.R. Swept Tapered Wing with a Flate Plate Control Surface at Unit Incidence $M = 0{\cdot}8$, $\nu = 0{\cdot}672$

$$Q_1 = Q_1' + iQ_1'' = \int_{-1}^{1} \int_{x_l}^{x_t} \Delta C_p \, dx \, d\eta,$$

$$Q_2 = Q_2' + iQ_2'' = \int_{-1}^{1} \int_{x_l}^{x_t} x \,.\, \Delta C_p \, dx \, d\eta,$$

$$Q_3 = Q_3' + iQ_3'' = 2 \int_{\eta_{e_1}}^{\eta_{e_2}} \int_{x_h}^{x_t} (x - x_h) \,.\, \Delta C_p \, dx \, d\eta.$$

Real Part

			Equivalent Mode Calculation		
Q_i'	B.A.C. $m = 14$ $n = 6$	B.A.C. $m = 16$ $n = 8$	Davies $m = 14$ $n = 6$	Davies $m = 14$ $n = 8$	Davies $m = 12$ $n = 10$
Q_1'	3·427	3·355	3·407	3·372	3·414
Q_2'	4·716	4·594	4·617	4·564	4·598
Q_3'	0·125	0·117	0·124	0·116	0·115

Imaginary Part

			Equivalent Mode Calculation		
Q_i''	B.A.C. $m = 14$ $n = 6$	B.A.C. $m = 16$ $n = 8$	Davies $m = 14$ $n = 6$	Davies $m = 14$ $n = 8$	Davies $m = 12$ $n = 10$
Q_1''	0·058	0·078	0·182	0·193	0·217
Q_2''	0·722	0·714	0·831	0·842	0·880
Q_3''	0·109	0·107	0·106	0·108	0·109

TABLE 5

Comparison of the Generalised Airforces Q_i, $i = 1, 2, 3$ for the N.L.R. Swept Tapered Wing with a Control Surface Camber Defined by $z = (x-x_h)[1+(x-x_h)+2\,.\,(x-x_h)^2]$ $M=0{\cdot}8, \nu=0{\cdot}672$

$$Q_1 = Q_1' + iQ_1'' = \int_{-1}^{1} \int_{x_l}^{x_t} \Delta C_p \, dx \, d\eta,$$

$$Q_2 = Q_2' + iQ_2'' = \int_{-1}^{1} \int_{x_l}^{x_t} x\,.\,\Delta C_p \, dx \, d\eta$$

$$Q_3 = Q_3' + iQ_3'' = 2\int_{\eta_{e_1}}^{\eta_{e_2}} \int_{x_h}^{x_t} (x-x_h)\,.\,\Delta C_p \, dx \, d\eta.$$

KEY: A. B.A.C. results for the cambered control surface.
B. B.A.C. results for the flat-plate control $z = x - x_h$, $+a$ lifting-surface calculation on the control-surface mode $z = (x-x_h)^2[1+2(x-x_h)]$.

Real Part

Q_i'	A $m=14$ $n=6$	B $m=14$ $n=6$
Q_1'	6·625	6·688
Q_2'	9·578	9·598
Q_3'	0·430	0·422

Imaginary Part

Q_i''	A $m=14$ $n=6$	B $m=14$ $n=6$
Q_1''	−0·349	−0·472
Q_2''	0·503	0·443
Q_3''	0·169	0·170

TABLE 6

Comparison on the Generalised Airforces Q_i, $i = 1, 2, 3$ for the B.A.C. Swept Tapered Wing $M = 0{\cdot}5$, $\nu = 0{\cdot}9551$

$$Q_1 = Q_1' + iQ_1'' = \int_{-1}^{1} \int_{x_l}^{x_t} \Delta C_p \, dx \, d\eta,$$

$$Q_2 = Q_2' + iQ_2'' = \int_{-1}^{1} \int_{x_l}^{x_t} x \, . \, \Delta C_p \, dx \, d\eta,$$

$$Q_3 = Q_3' + iQ_3'' = 2 \int_{\eta_{e_1}}^{\eta_{e_2}} \int_{x_h}^{x_t} (x - x_h) \, . \, \Delta C_p \, dx \, d\eta.$$

Real Part

Q_i'	B.A.C. $m = 14$ $n = 6$	Equiv. modes Davies $m = 16$ $n = 8$
Q_1'	2·466	2·422
Q_2'	2·784	2·716
Q_3'	0·074	0·071

Imaginary Part

Q_i''	B.A.C. $m = 14$ $n = 6$	Equiv. modes Davies $m = 16$ $n = 8$
Q_1''	0·490	0·544
Q_2''	0·748	0·780
Q_3''	0·068	0·068

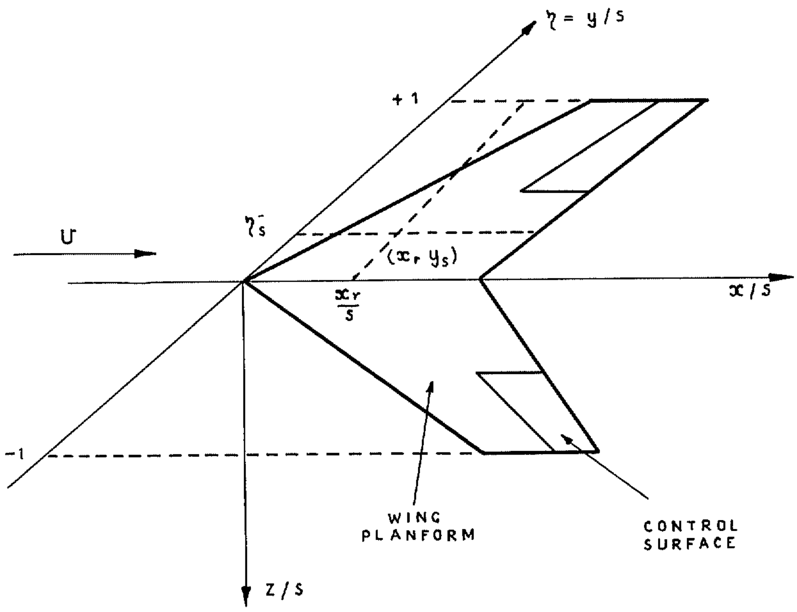

FIG. 1. The coordinate axes and a typical planform.

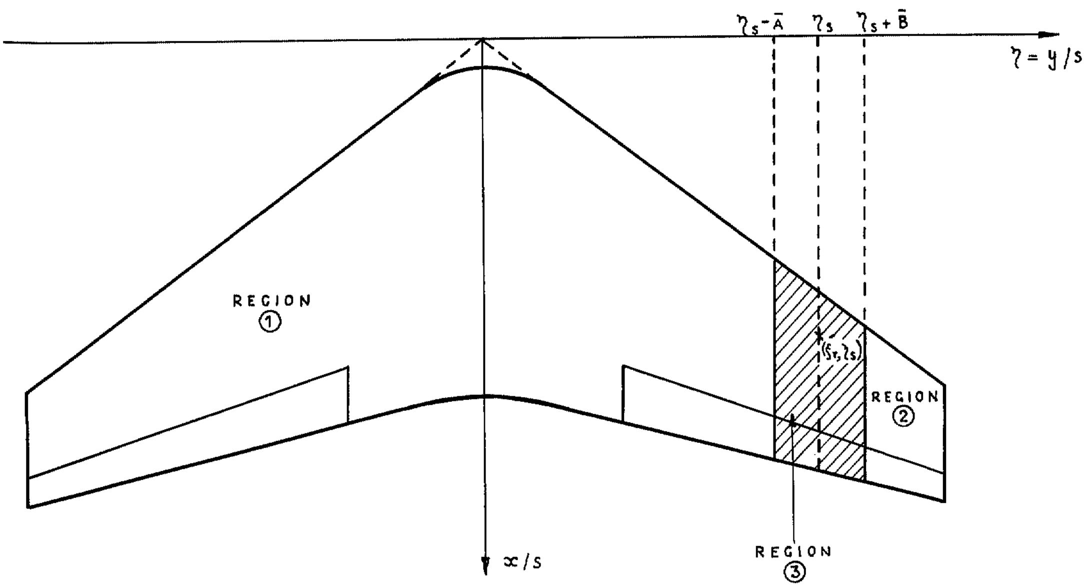

FIG. 2. A regularised planform breakdown into regions ① ② and ③.

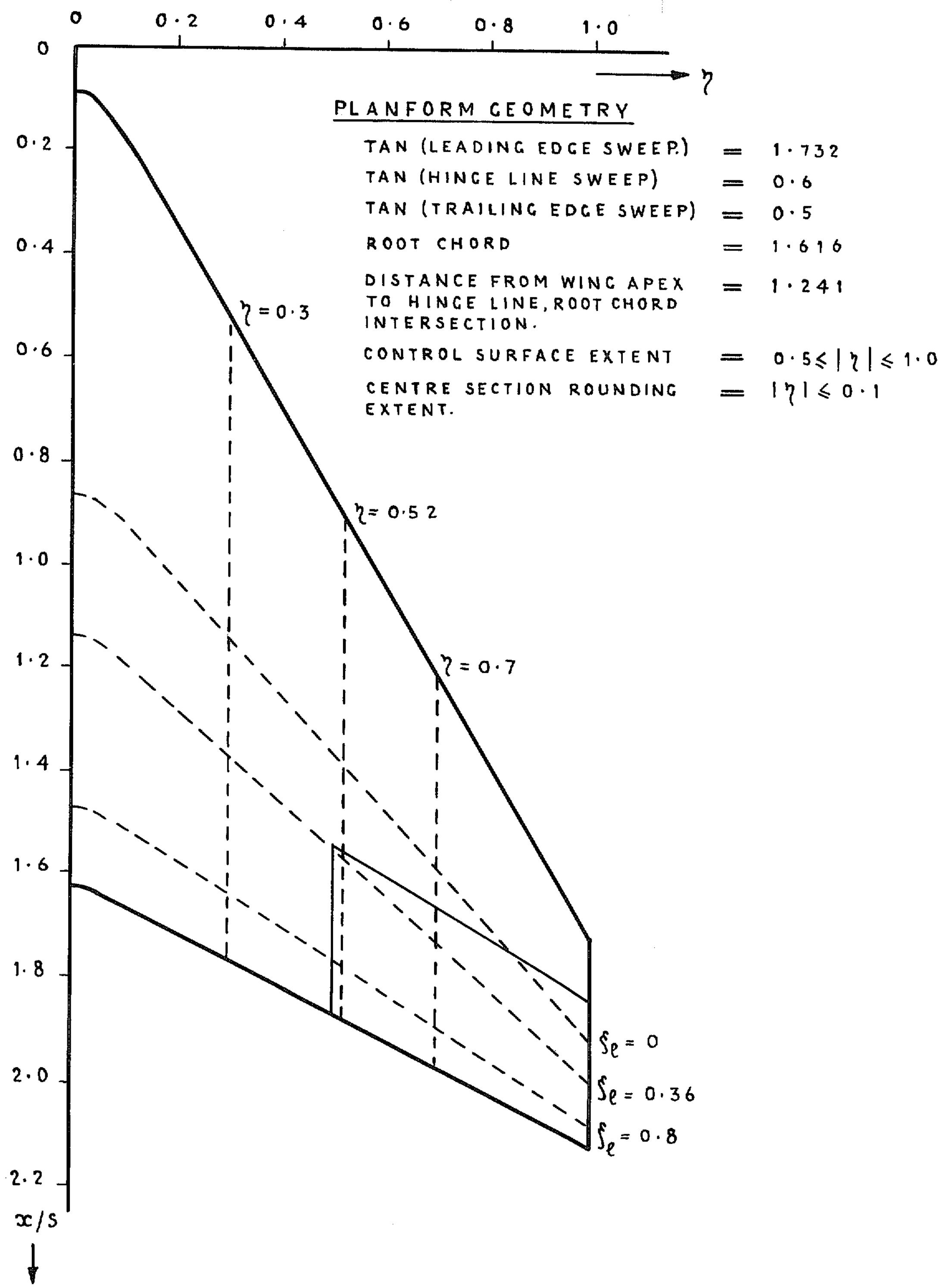
0
0·2
0·4
0·6
0·8
1·0
η
PLANFORM GEOMETRY
TAN (LEADING EDGE SWEEP) = 1·732
TAN (HINGE LINE SWEEP) = 0·6
TAN (TRAILING EDGE SWEEP) = 0·5
ROOT CHORD = 1·616
DISTANCE FROM WING APEX TO HINGE LINE, ROOT CHORD INTERSECTION. = 1·241
CONTROL SURFACE EXTENT = 0·5 ≤ |η| ≤ 1·0
CENTRE SECTION ROUNDING EXTENT. = |η| ≤ 0·1
η = 0·3
η = 0·52
η = 0·7
ξ_ℓ = 0
ξ_ℓ = 0·36
ξ_ℓ = 0·8
1·2
1·4
1·6
1·8
2·0
2·2
x/s

FIG. 3. Wing *E*.

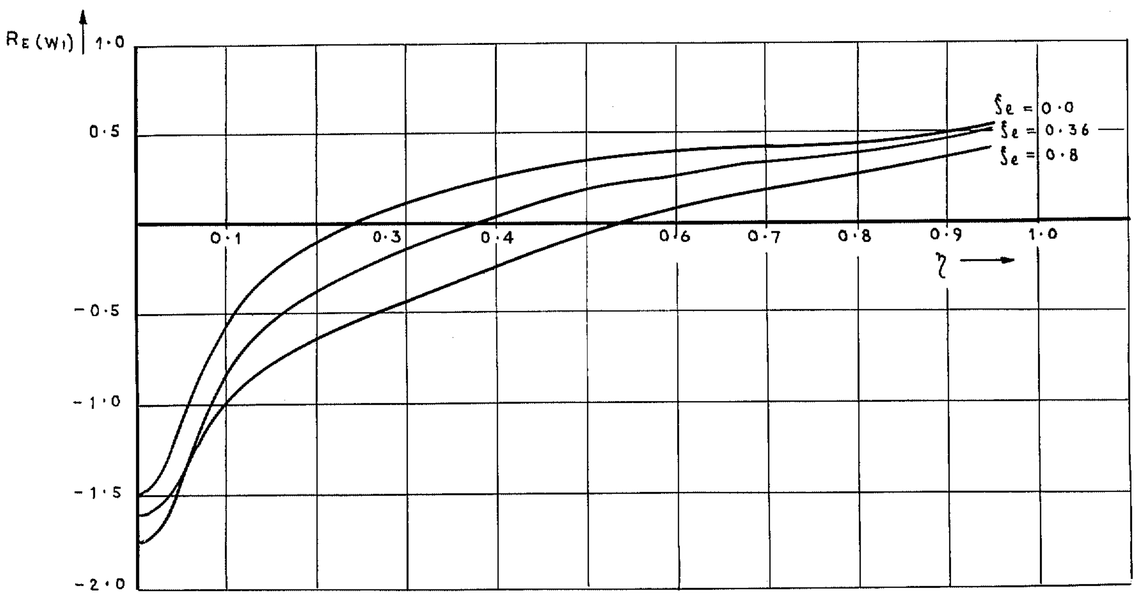

FIG. 4. Re $(W_1) V\eta$ for wing E.

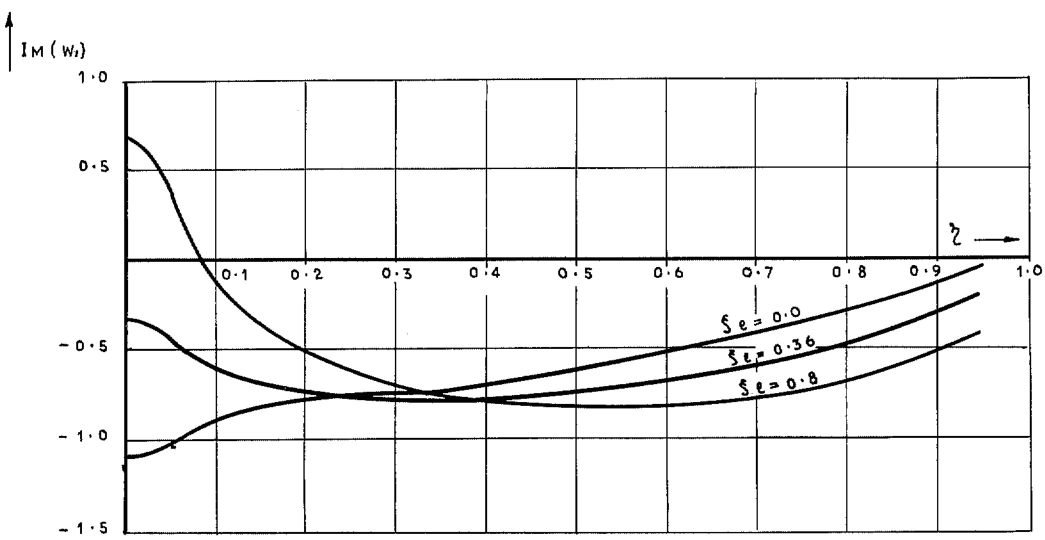

FIG. 5. IM $(W_1) V\eta$ for wing E.

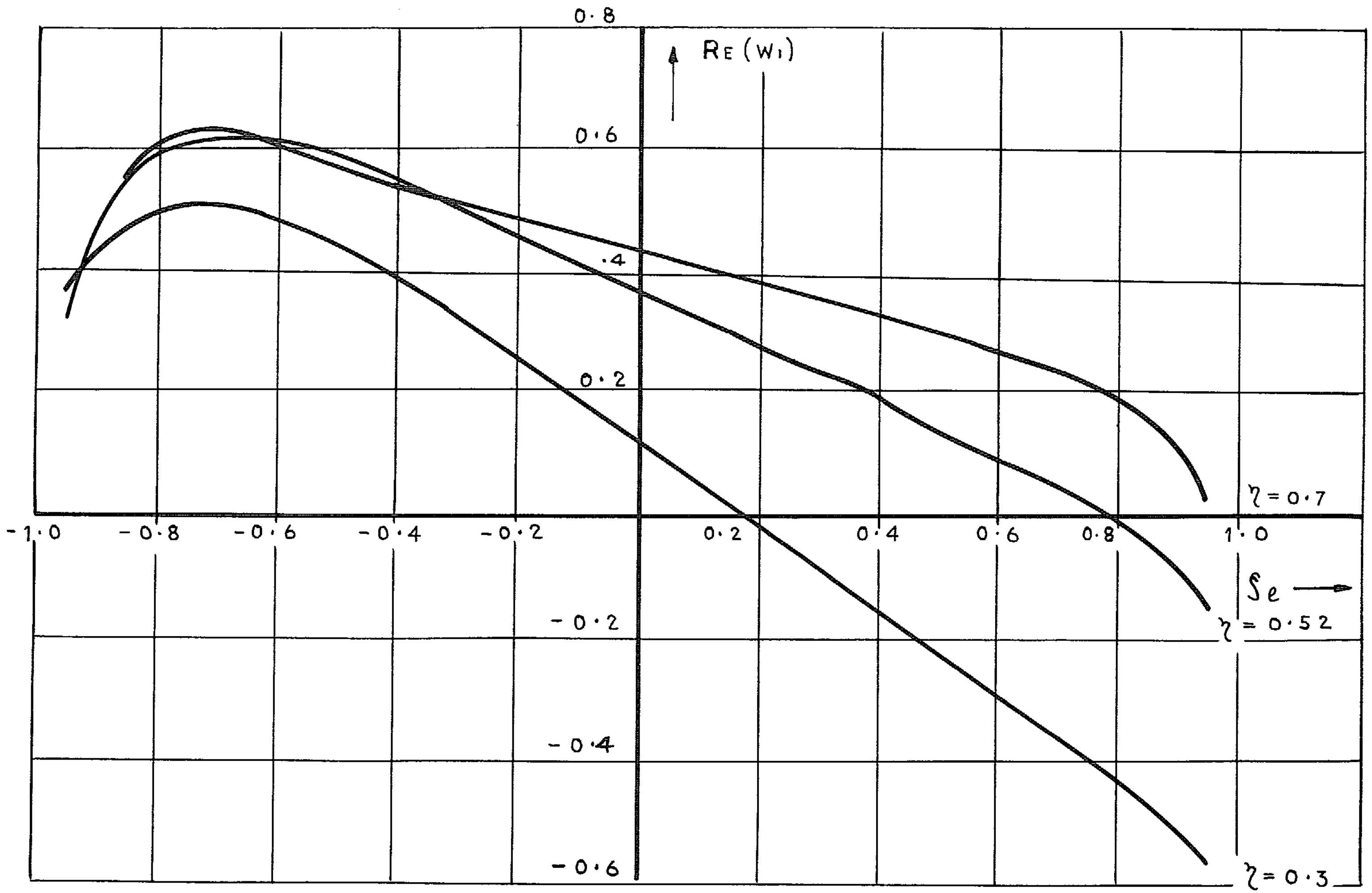

FIG. 6. Re $(W_1) V\xi_l$ for wing E.

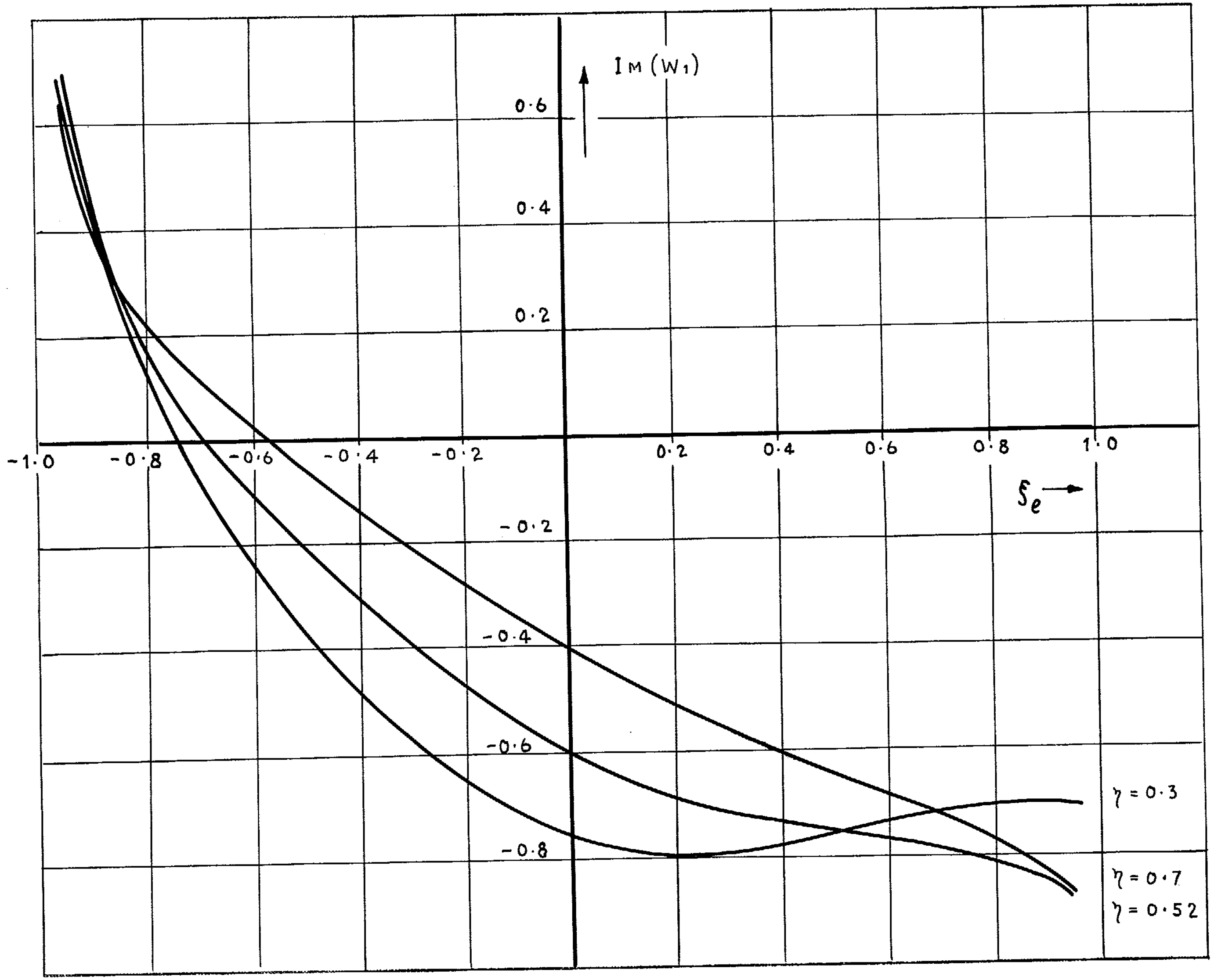

FIG. 7. Im $(W_1) V\xi_l$ for wing E.

PLANFORM GEOMETRY.

ROOT CHORD.	=	0·814
DISTANCE OF WING APEX TO HINGE LINE, ROOT CHORD INTERSECTION.	=	0·5698
CONTROL SURFACE EXTENT	=	$0 \leq \lvert\eta\rvert \leq 1 \cdot 0$

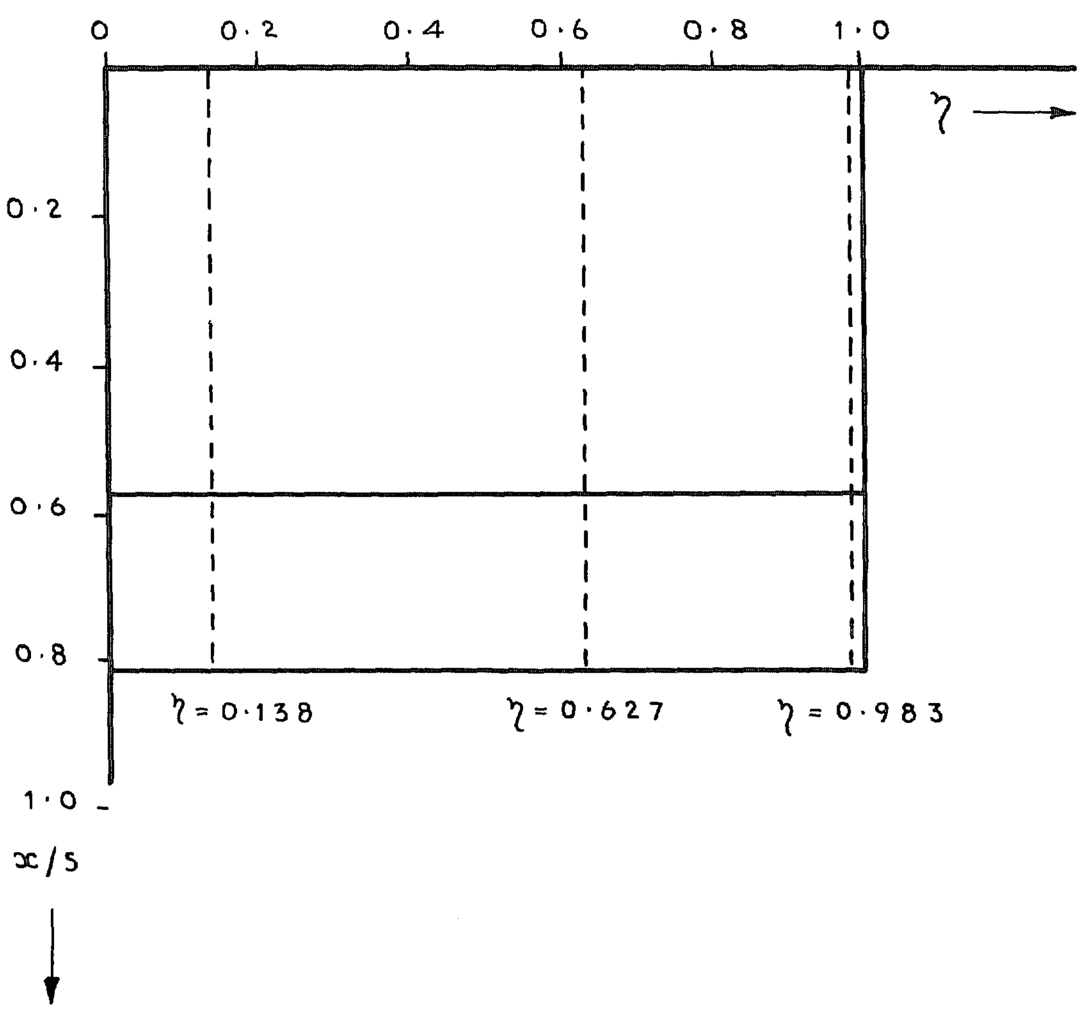

FIG. 8. N.L.R. rectangular wing.

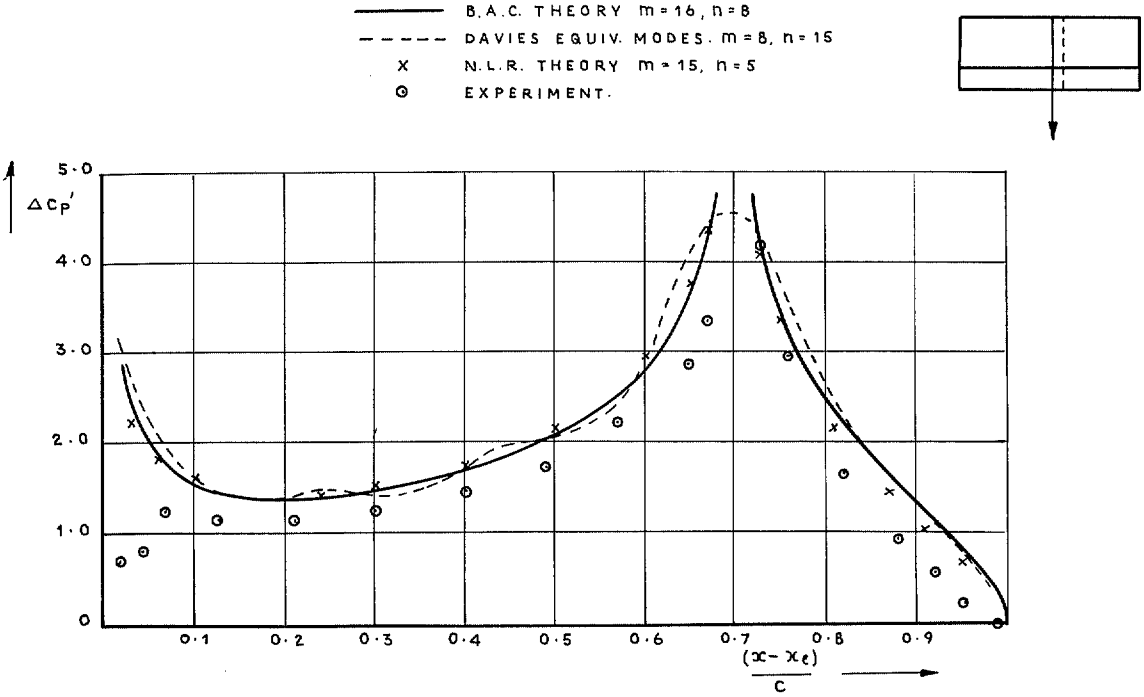

FIG. 9.

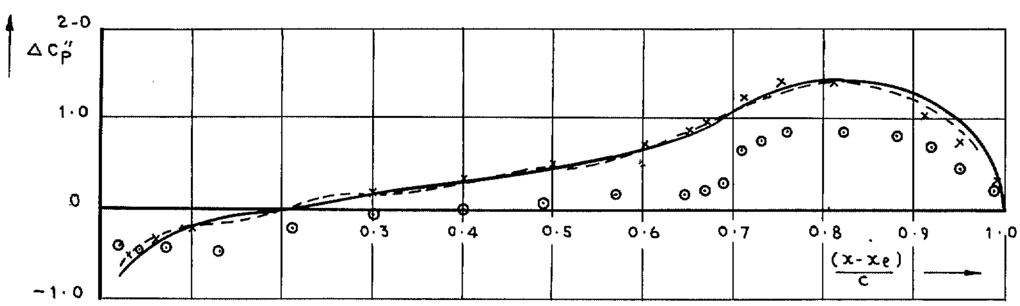

FIG. 10. Pressure comparisons for the N.L.R. rectangular wing. $M = 0{\cdot}0$, $\nu = 1{\cdot}115$. Real and imaginary pressures for the station eta (η) $= 0{\cdot}138$.

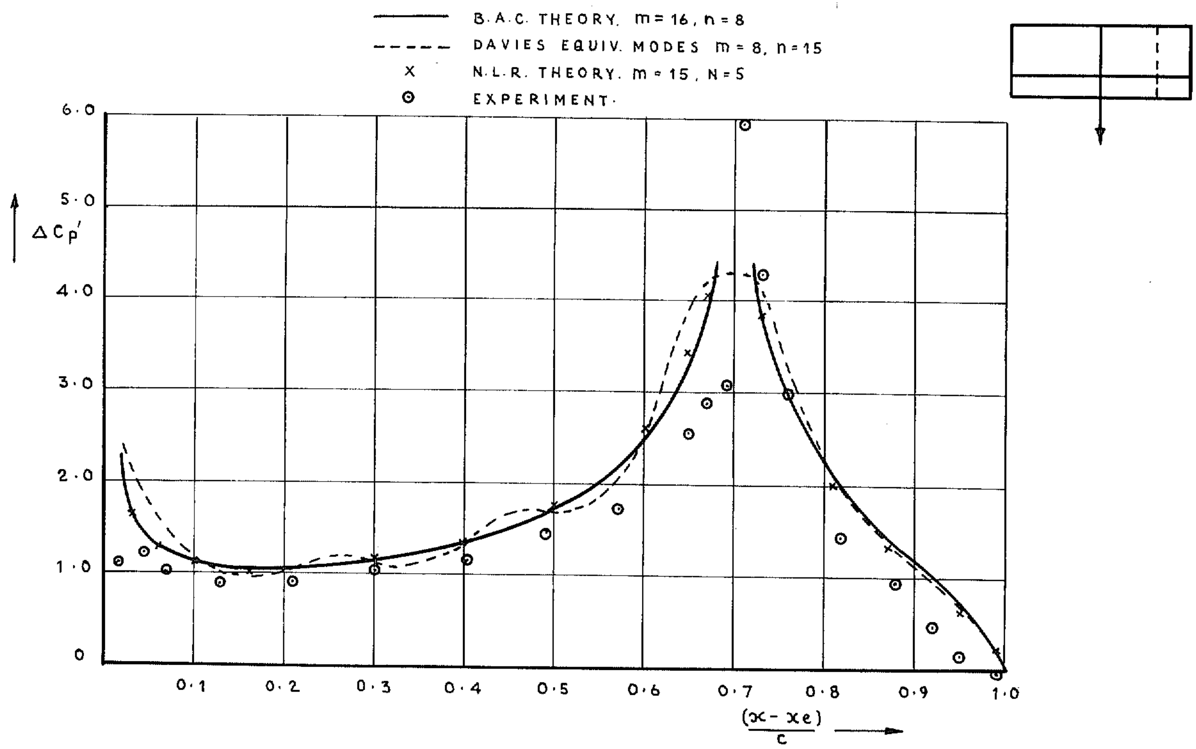

FIG. 11.

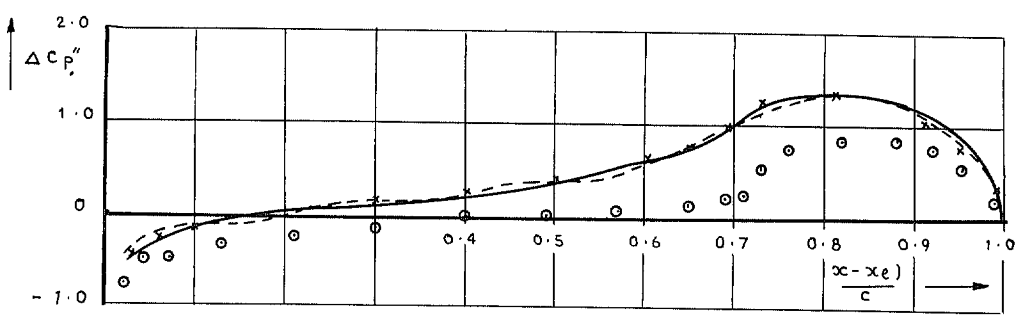

FIG. 12. Pressure comparisons for the N.L.R. rectangular wing. $M = 0{\cdot}0$, $\nu = 1{\cdot}115$. Real and imaginary pressures for the station eta $(\eta) = 0{\cdot}627$.

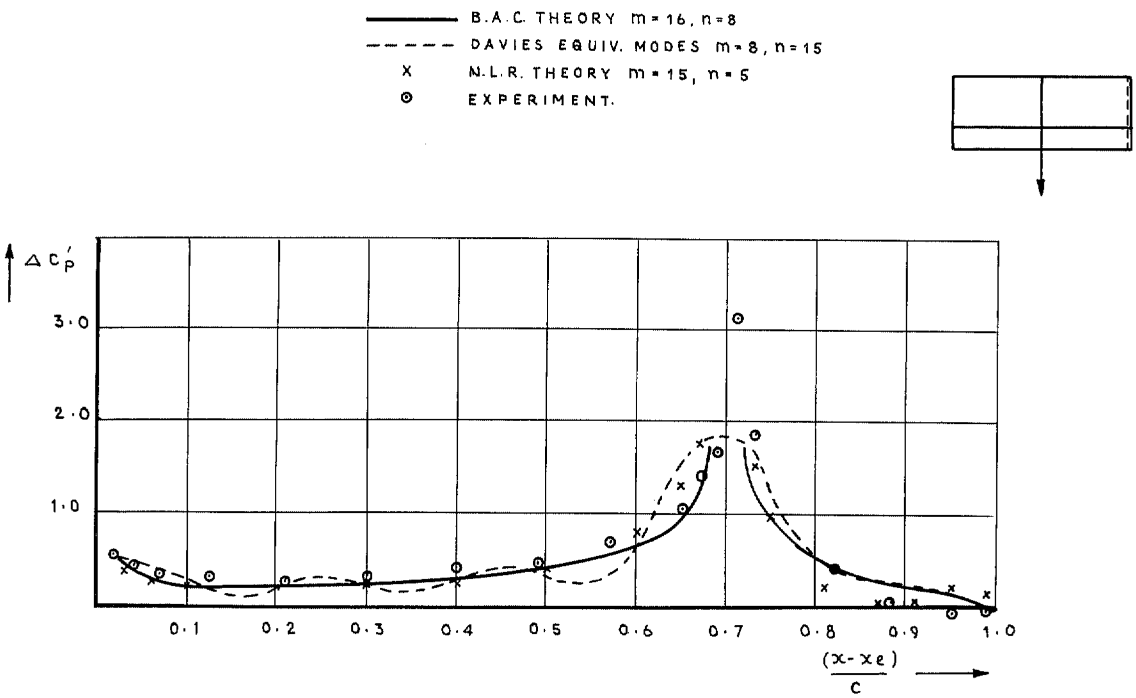

FIG. 13.

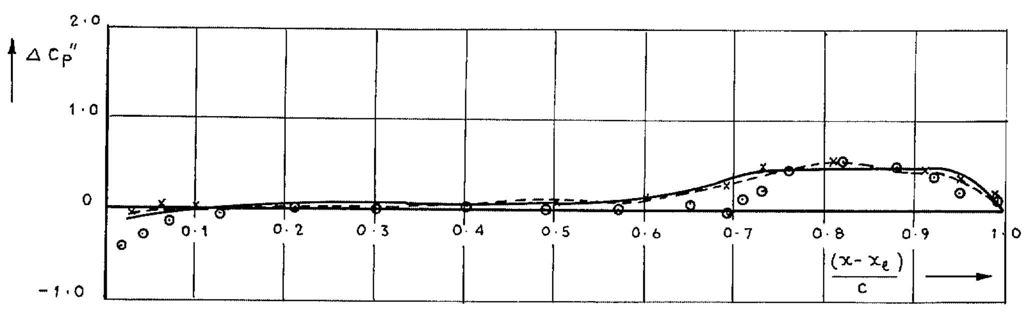

FIG. 14. Pressure comparisons for the N.L.R. rectangular wing. $M = 0{\cdot}0$, $\nu = 1{\cdot}115$. Real and imaginary pressures for the station eta (η) = 0·983.

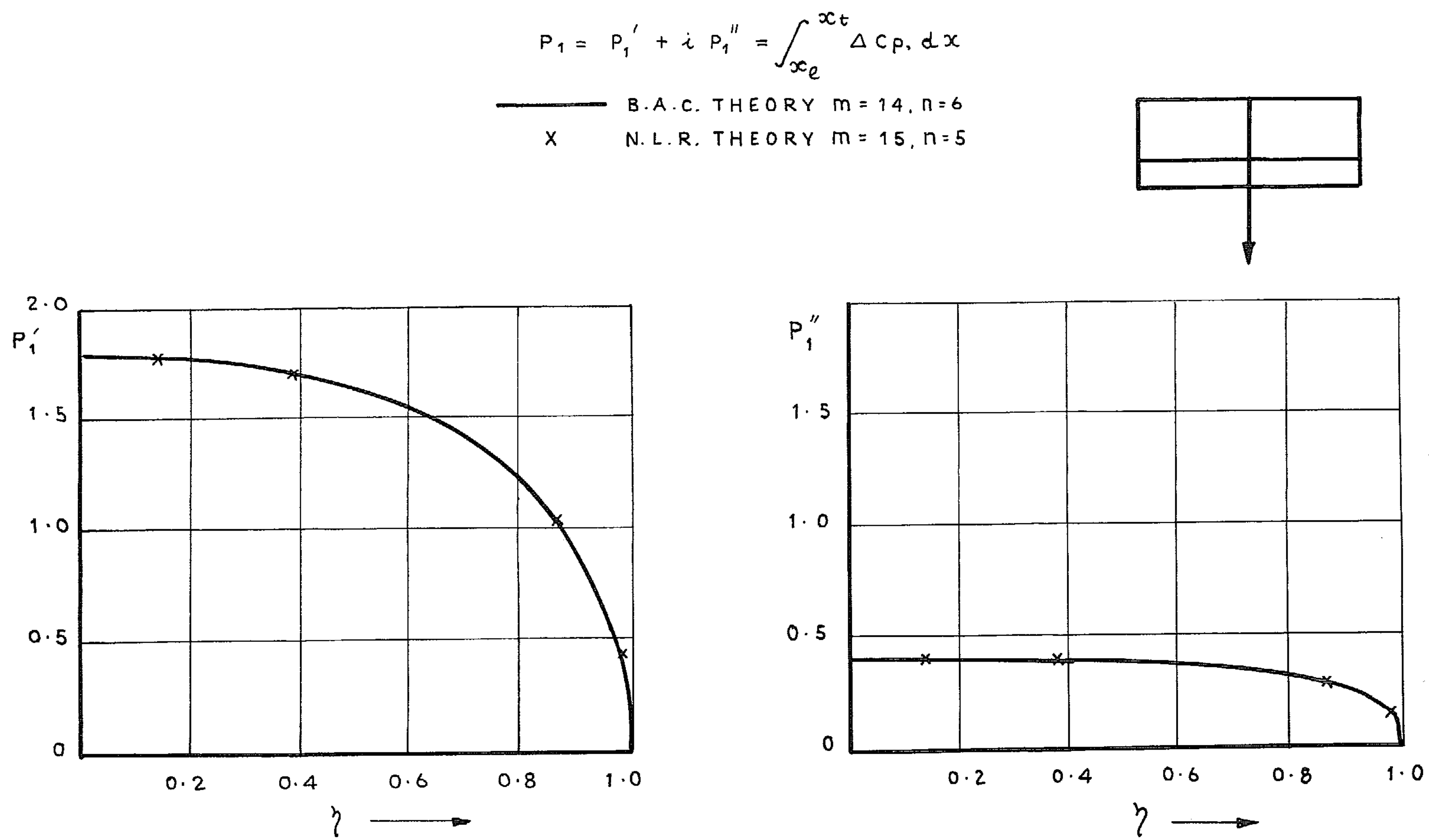

FIG. 15. Comparison of the local lift (P_1) on the N.L.R. rectangular wing. $M = 0{\cdot}0$, $\nu = 1{\cdot}115$.

$$P_2 = P_2' + i\,P_2'' = \int_{x_\ell}^{x_t} (x - x_\ell - c/4)\,.\,\Delta C_p\,.\,dx.$$

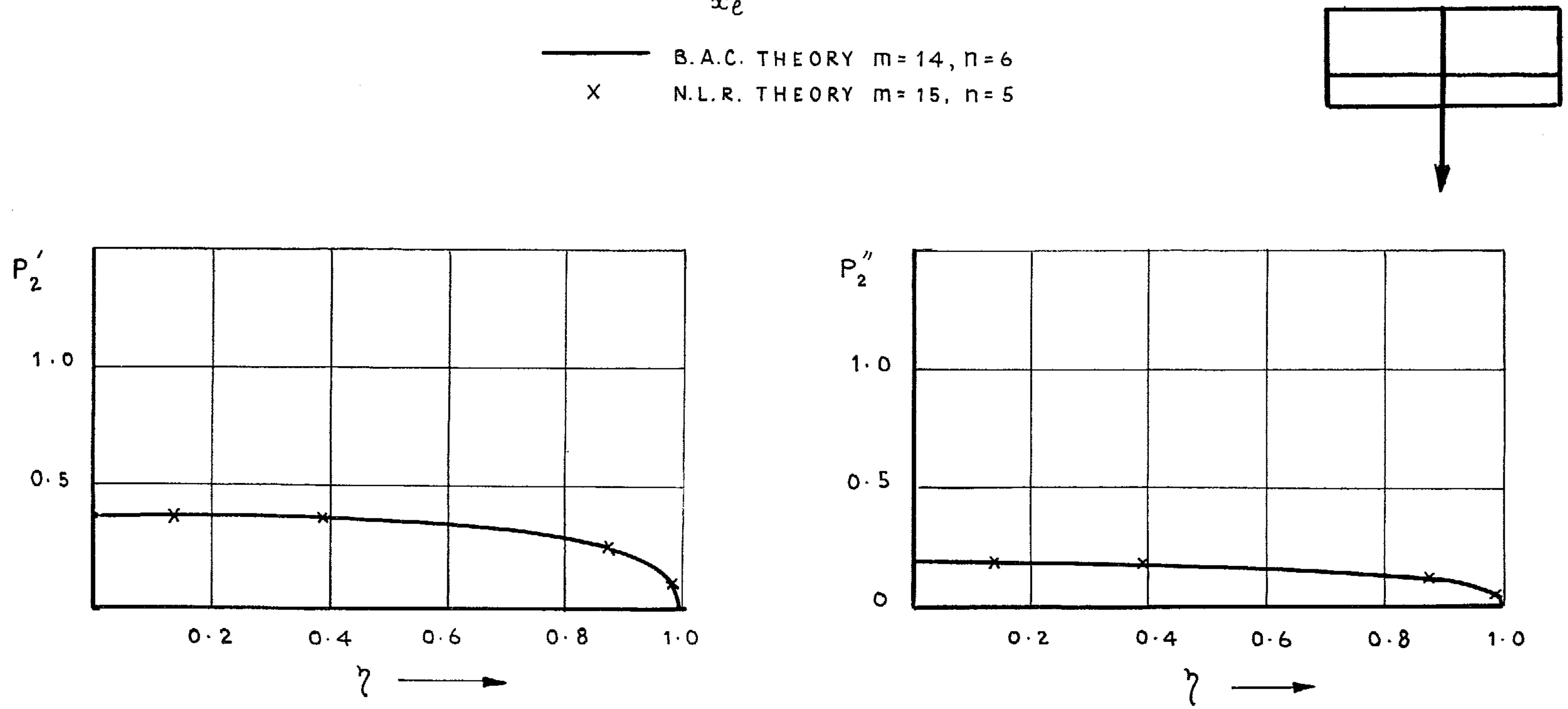

FIG. 16. Comparison of the local pitching moment about $\frac{1}{4}$ chord (P_2) on the N.L.R. rectangular wing. $M = 0{\cdot}0$, $\nu = 1{\cdot}115$.

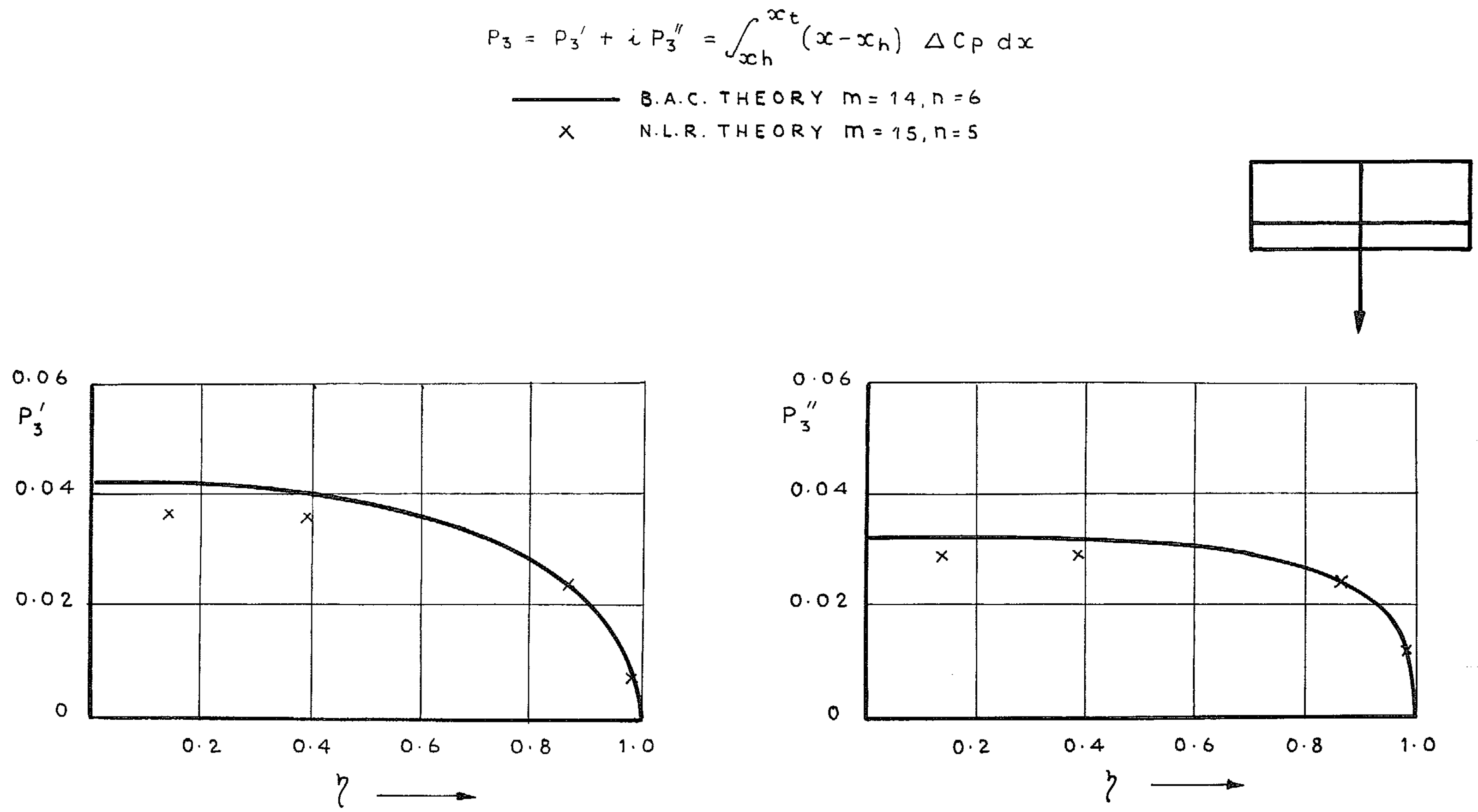

FIG. 17. Comparison of the local hinge moment (P_3) on the N.L.R. rectangular wing. $M = 0{\cdot}0$, $\nu = 1{\cdot}115$.

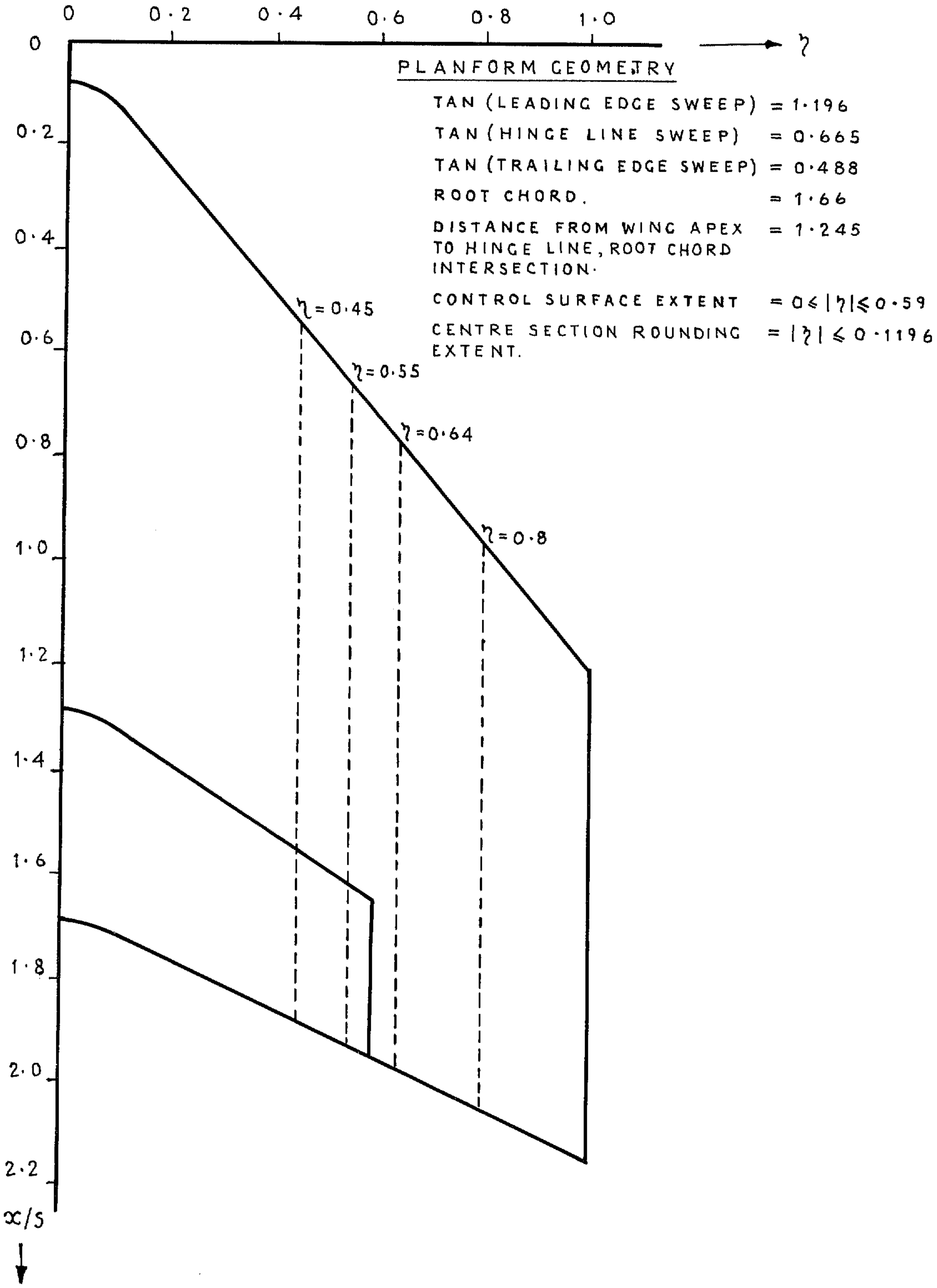

FIG. 18. N.L.R. swept tapered wing.

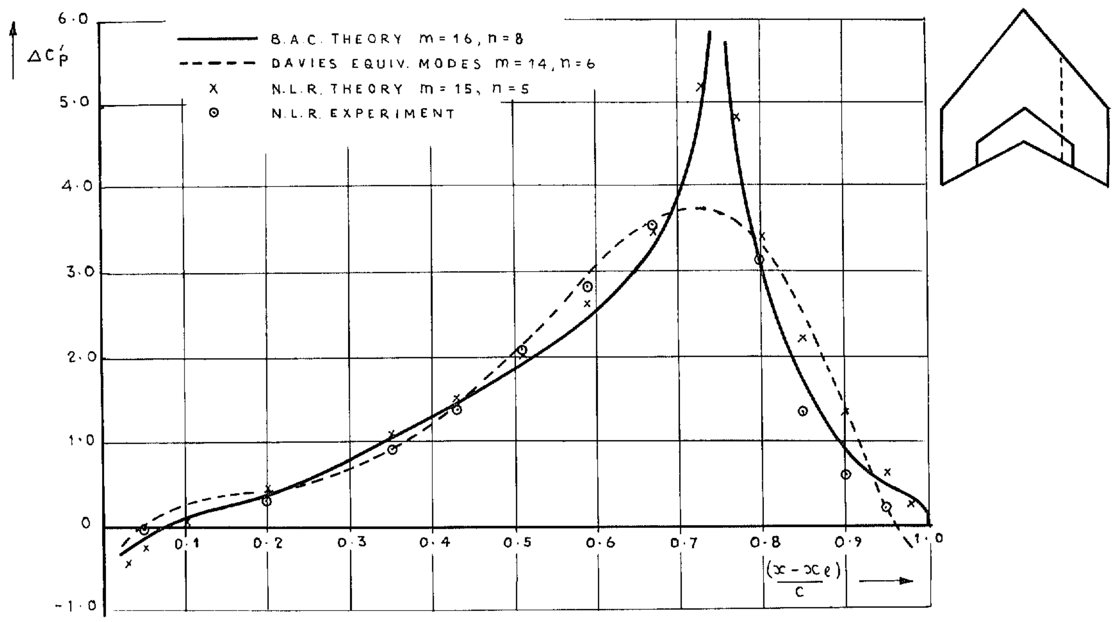

FIG. 19.

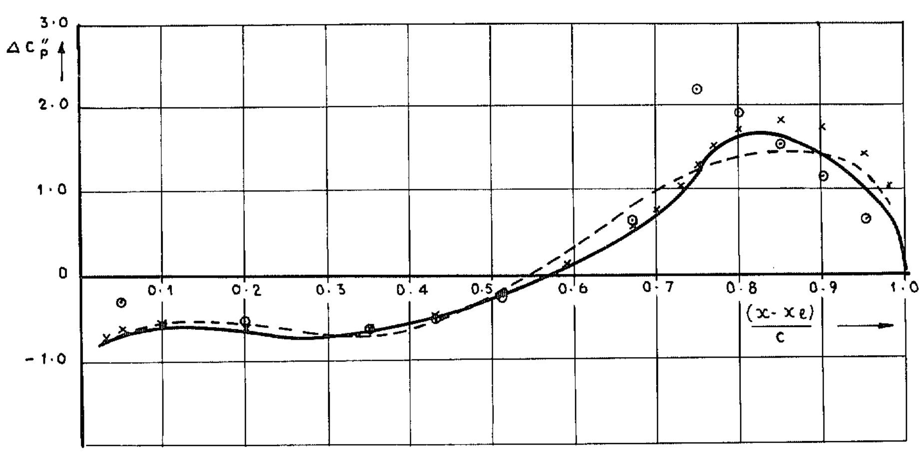

FIG. 20. Pressure comparisons for the N.L.R. swept tapered wing with a flat plate control surface at unit incidence. $M = 0{\cdot}8$, $\nu = 0{\cdot}672$. Real and imaginary pressures for the station eta (η) = 0·45.

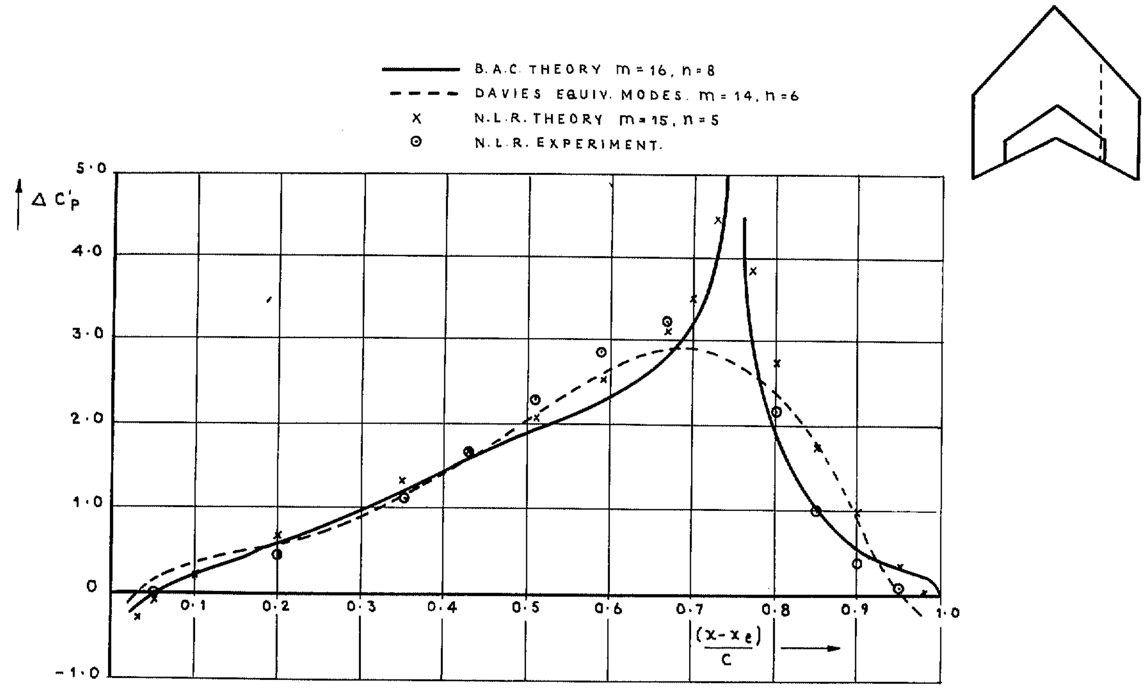

FIG. 21.

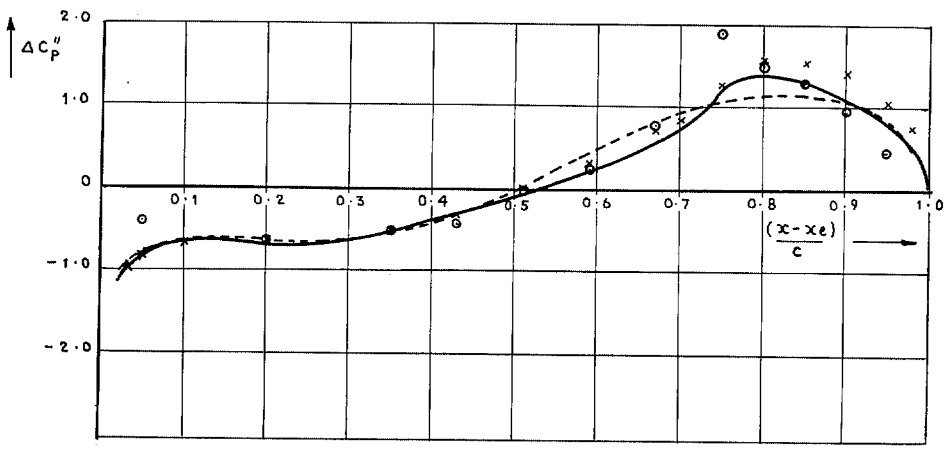

FIG. 22. Pressure comparisons for the N.L.R. swept tapered wing with a flat plate control surface at unit incidence. $M = 0{\cdot}8$, $\nu = 0{\cdot}672$. Real and imaginary pressures for the station eta (η) $= 0{\cdot}55$.

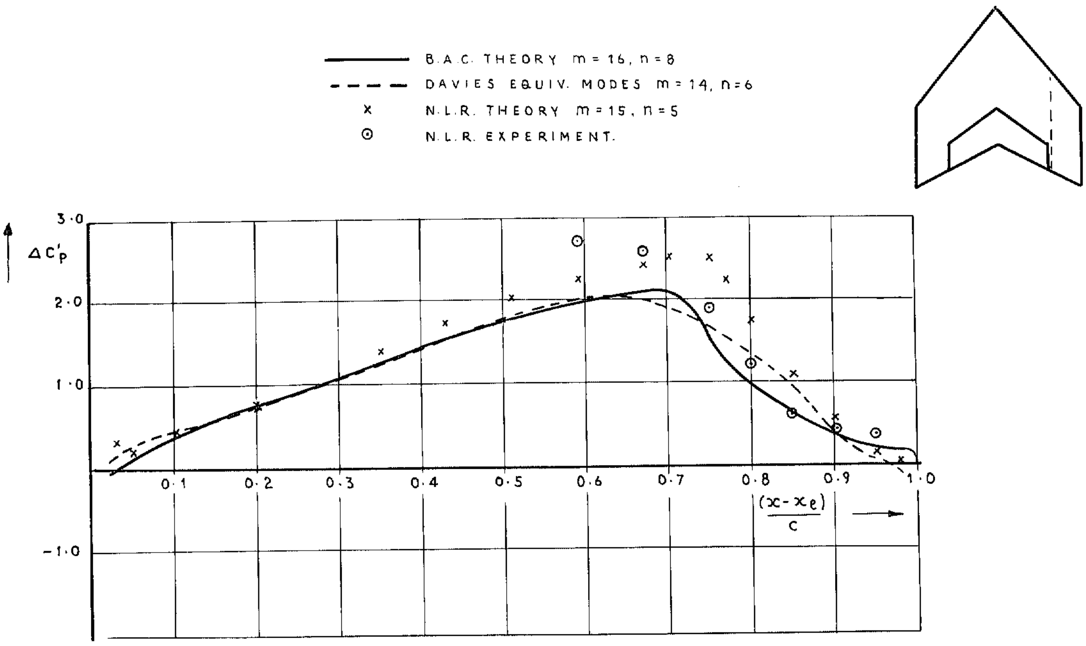

FIG. 23.

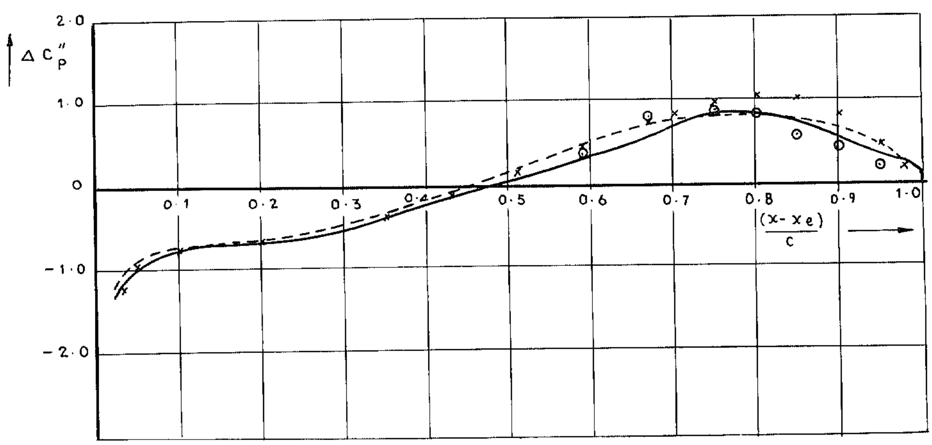

FIG. 24. Pressure comparisons for the N.L.R. swept tapered wing with a flat plate control surface at unit incidence. $M = 0{\cdot}8$, $\nu = 0.672$. Real and imaginary pressures for the station eta (η) = 0·64.

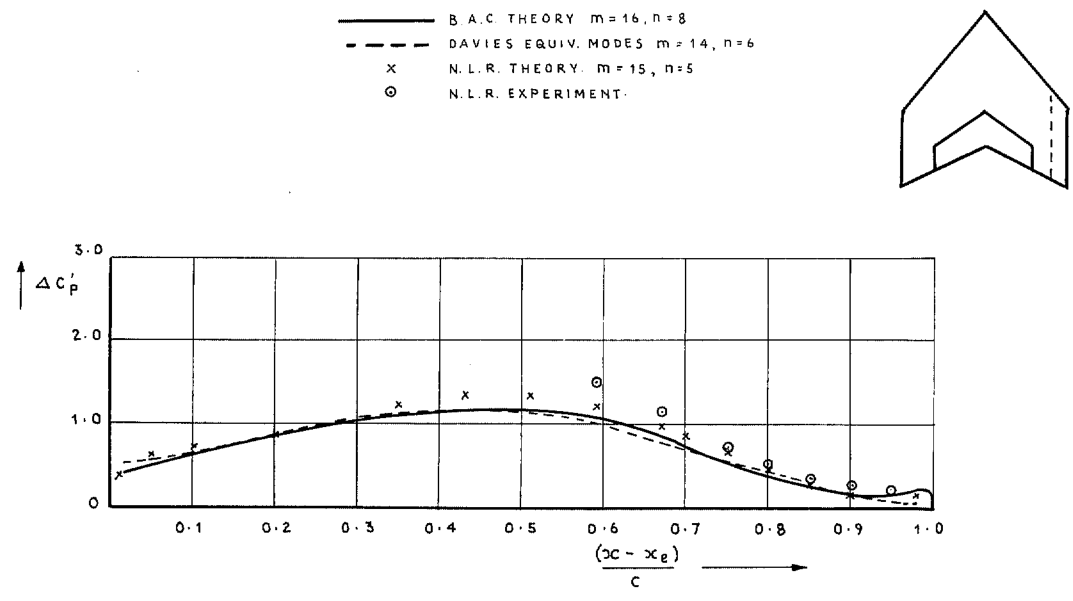

FIG. 25.

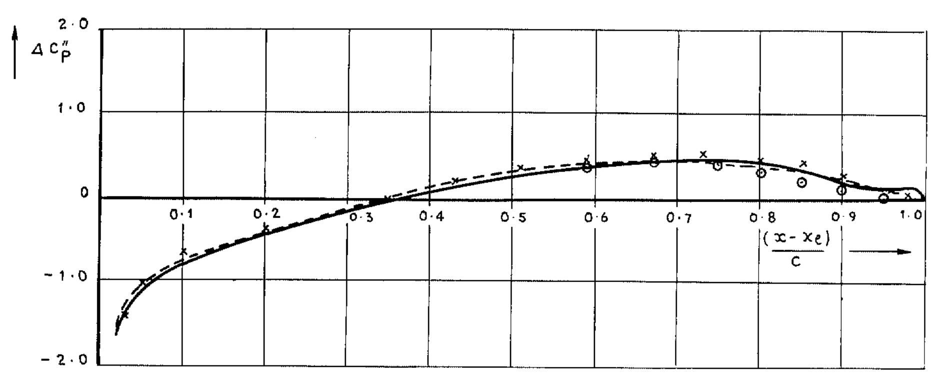

FIG. 26. Pressure comparisons for the N.L.R. swept tapered wing with a flat plate control surface at unit incidence. $M = 0{\cdot}8$, $\nu = 0{\cdot}672$. Real and imaginary pressures for the station eta (η) $= 0{\cdot}8$.

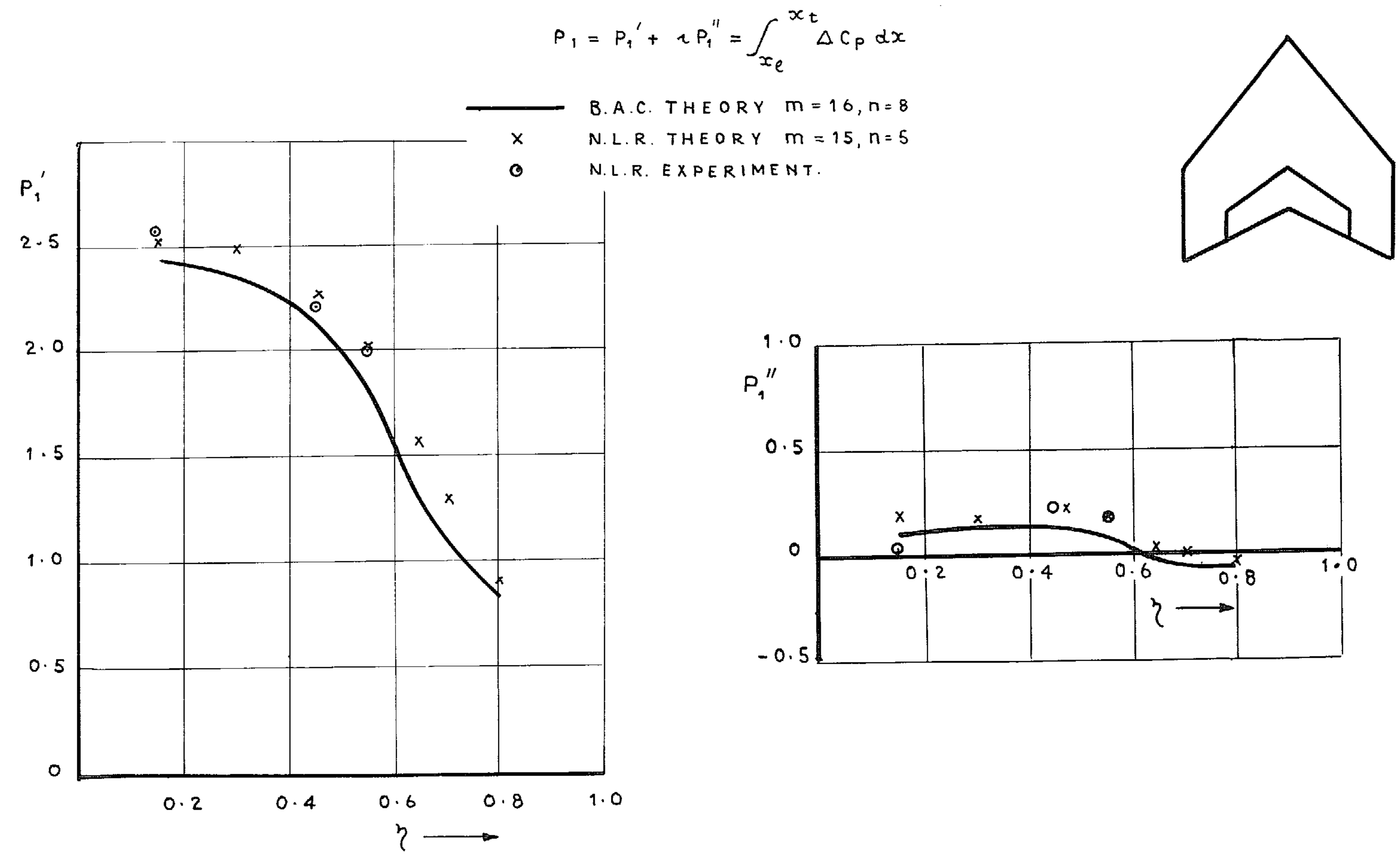

FIG. 27. Comparison of the local lift (P_1) on the N.L.R. swept tapered wing with flat plate control surface at unit incidence. $M = 0{\cdot}8$, $\nu = 0{\cdot}672$.

$$P_2 = P_2' + i\,P_2'' = \int_{x_l}^{x_t} (x - x_l - c/4)\,\Delta C_p \, dx \, .$$

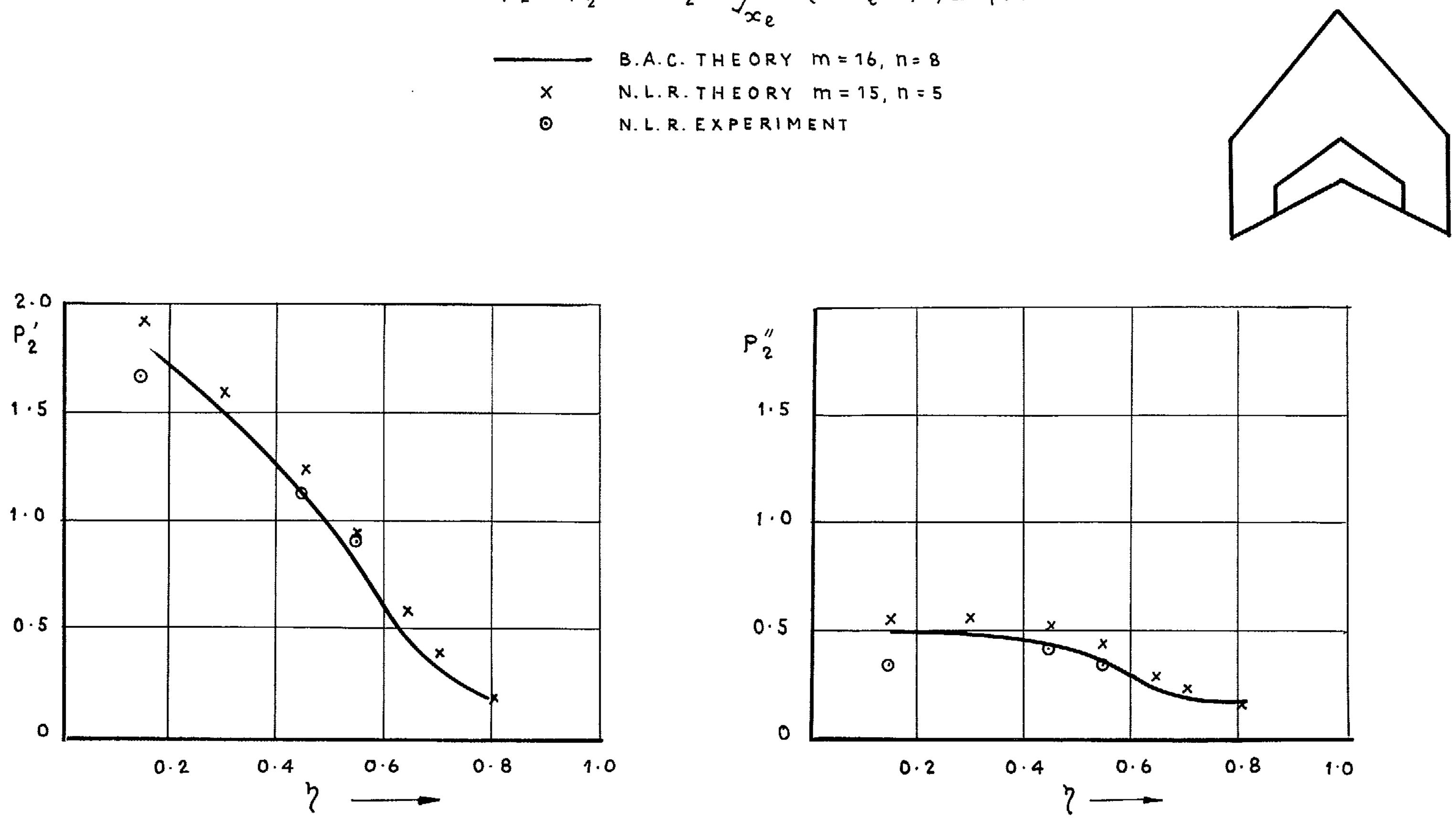

FIG. 28. Comparison of local pitching moment about $\frac{1}{4}$ chord (P_2) on the N.L.R. swept tapered wing with flat plate flap at unit incidence. $M = 0{\cdot}8$, $\nu = 0{\cdot}672$.

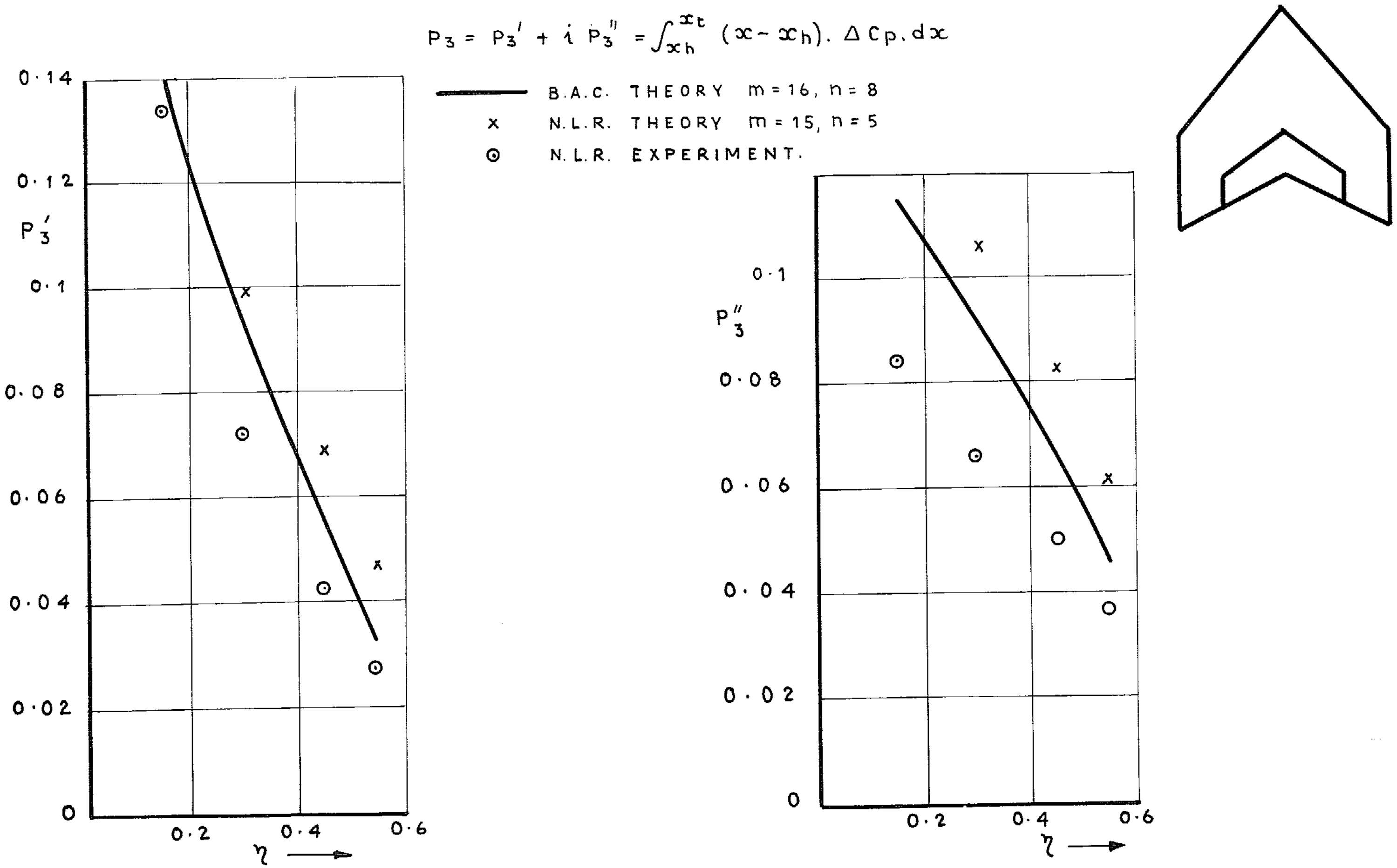

FIG. 29. Comparison of the local hinge moment (P_3) on the N.L.R. swept tapered wing with a flat plate flap at unit incidence. $M = 0{\cdot}8$, $\nu = 0{\cdot}672$.

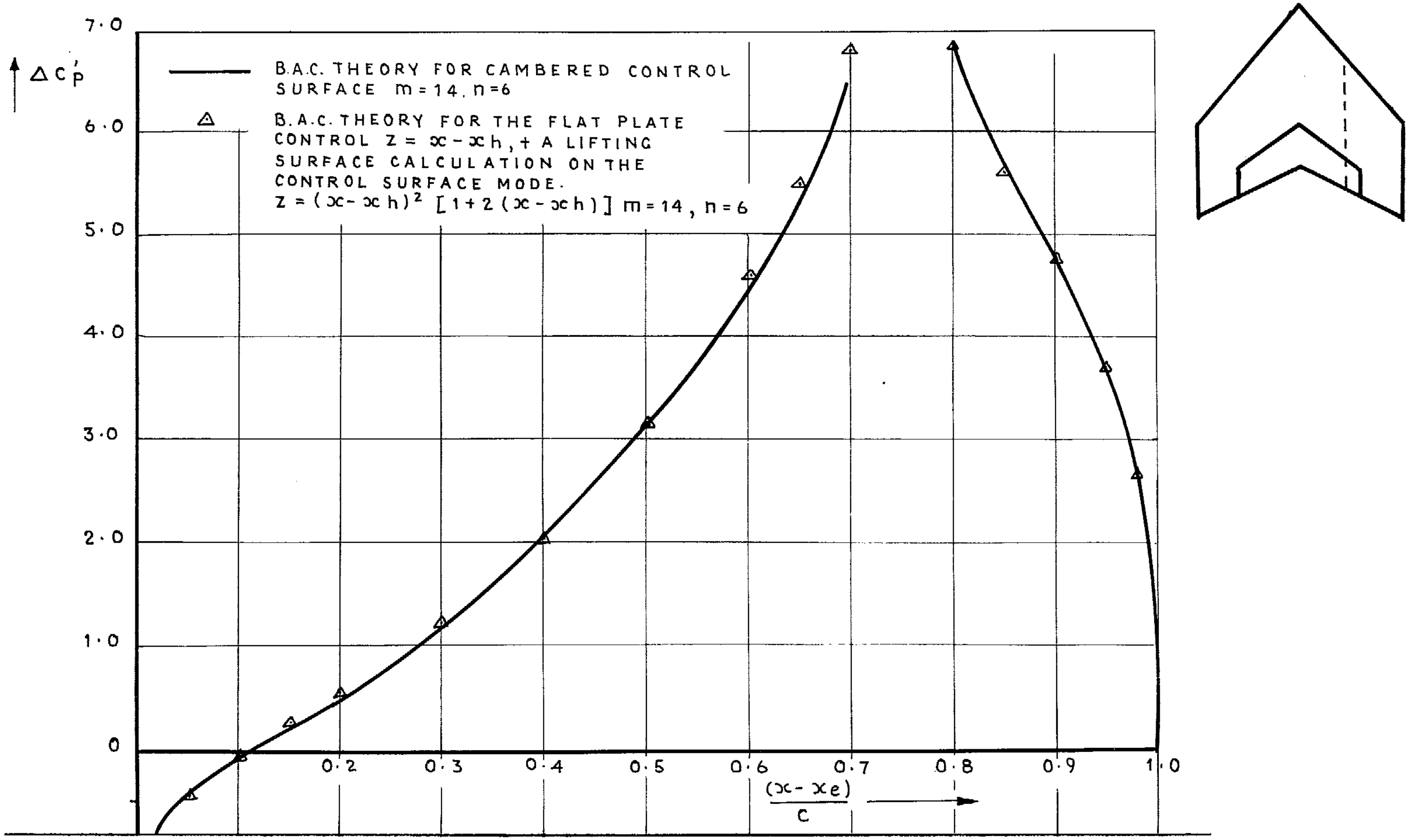

FIG. 30. Pressure comparisons for the N.L.R. swept tapered wing with a control surface camber defined by $z = (x - x_h)[1 + (x - x_h) + 2(x - x_h)^2]$. $M = 0{\cdot}8$, $\nu = 0{\cdot}672$. Real pressures for eta (η) $= 0{\cdot}45$.

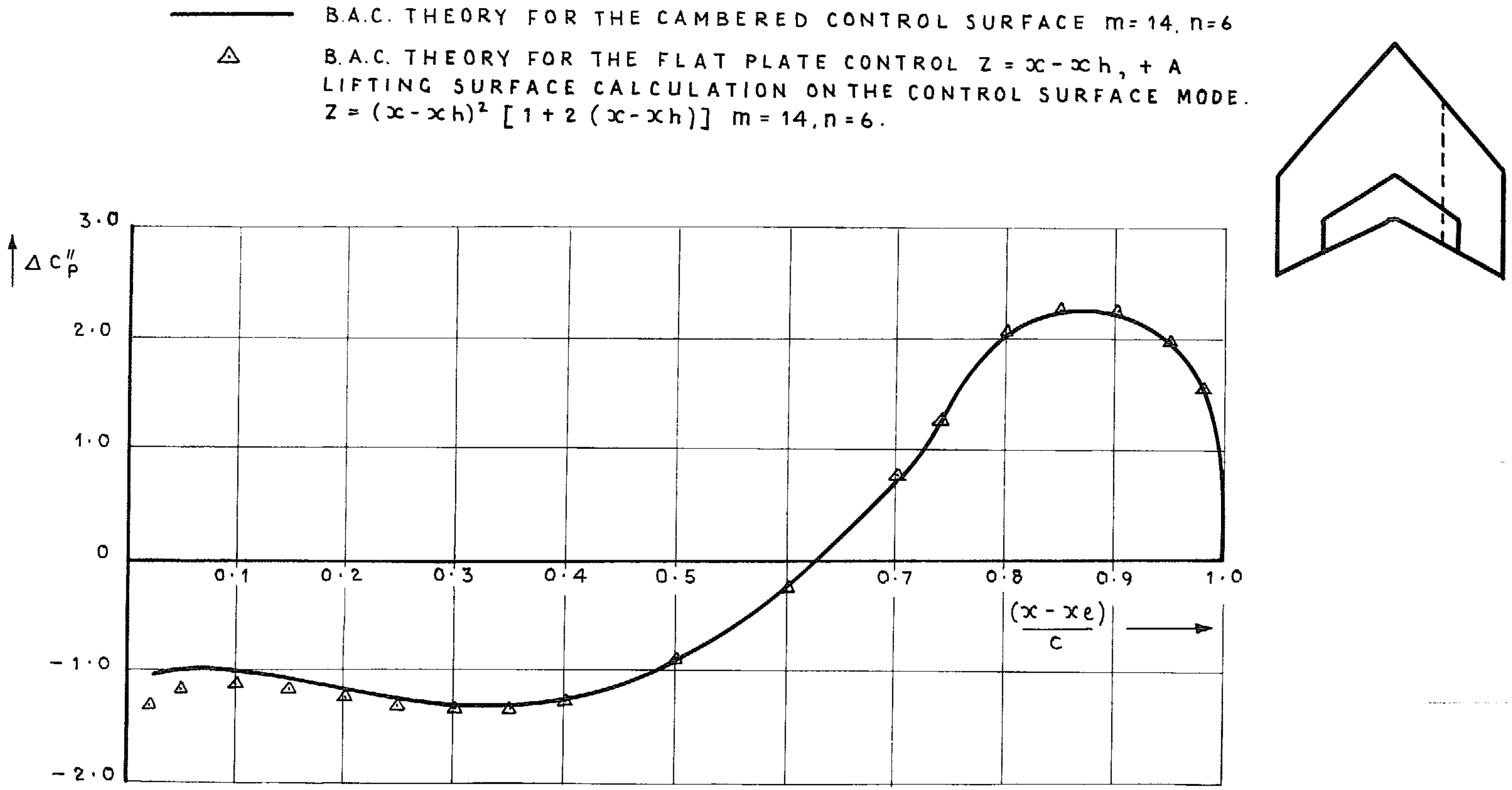

FIG. 31. Pressure comparisons for the N.L.R. swept tapered wing with a control surface camber defined by $z=(x-x_h)[1+(x-x_h)+2(x-x_h)^2]$. $M=0{\cdot}8$, $\nu=0{\cdot}672$. Imaginary pressures for eta $(\eta)=0{\cdot}45$.

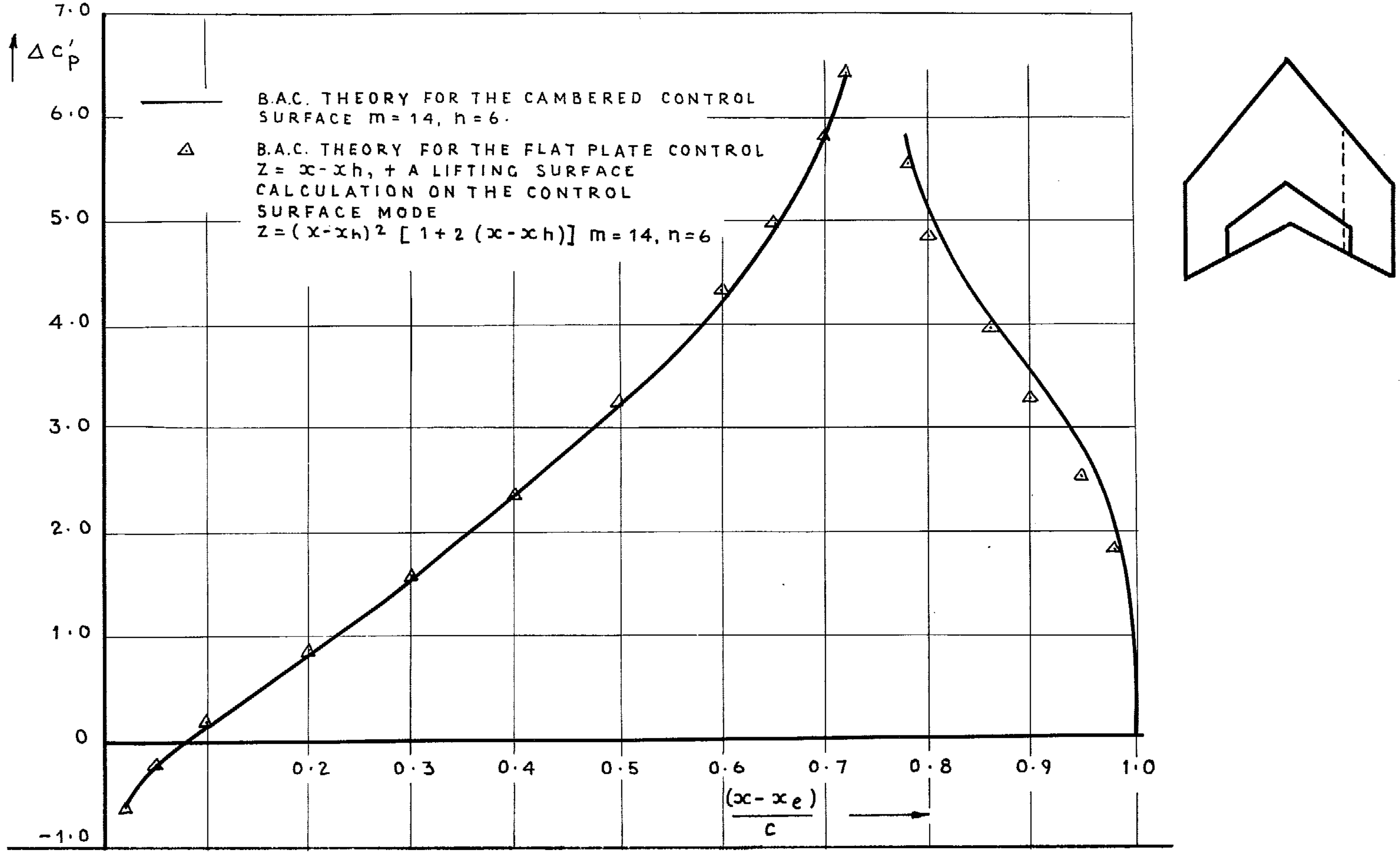

FIG. 32. Pressure comparisons for the N.L.R. swept tapered wing with a control surface camber defined by $z = (x - x_h)[1 + (x - x_h) + 2(x - x_h)^2]$. $M = 0{\cdot}8$, $\nu = 0{\cdot}672$. Real pressures for eta (η) = 0·55.

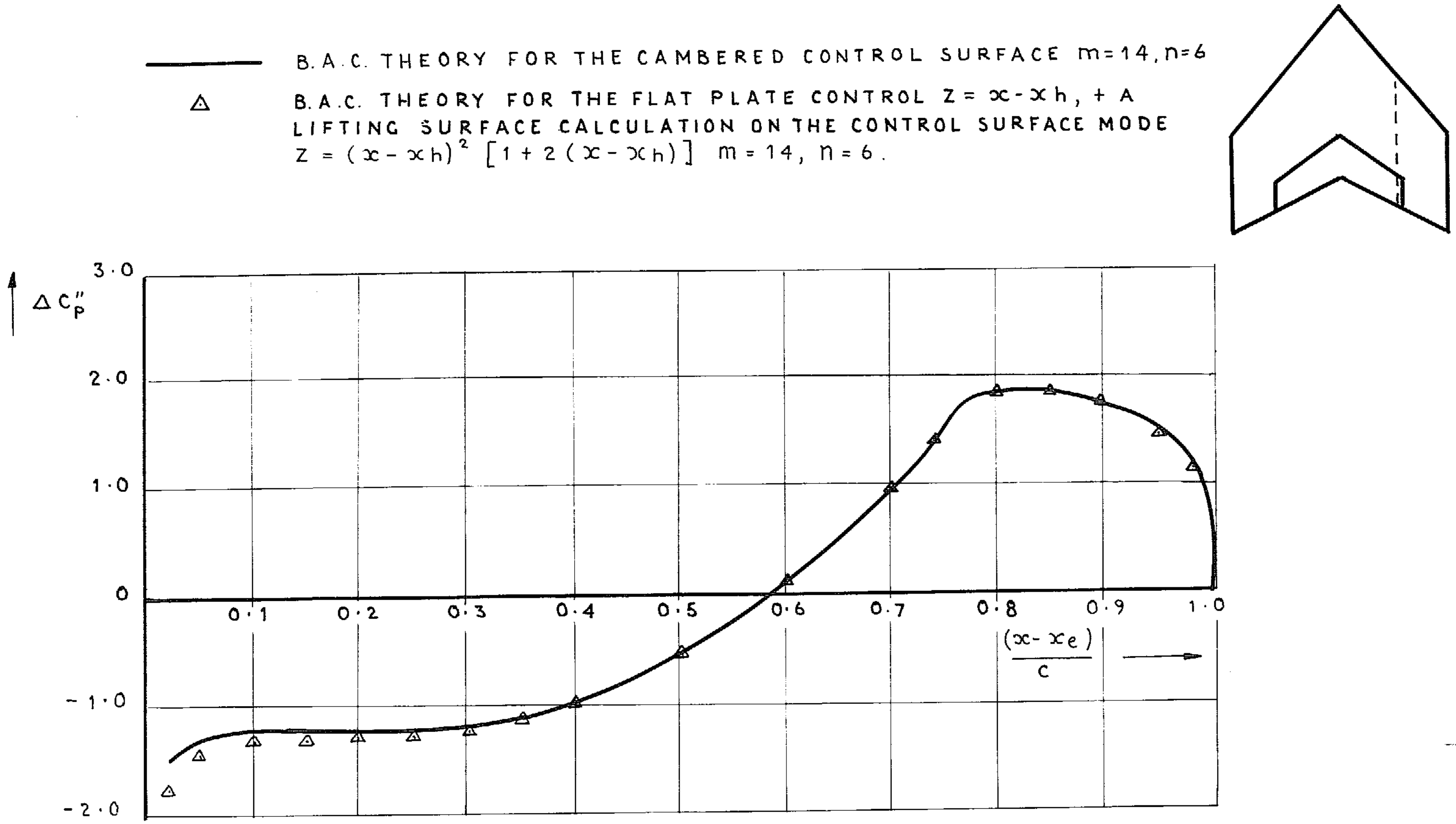

FIG. 33. Pressure comparisons for the N.L.R. swept tapered wing with a control surface camber defined by $z = (x - x_h)[1 + (x - x_h) + 2(x - x_h)^2]$. $M = 0{\cdot}8$, $\nu = 0{\cdot}672$. Imaginary pressures for eta $(\eta) = 0{\cdot}55$.

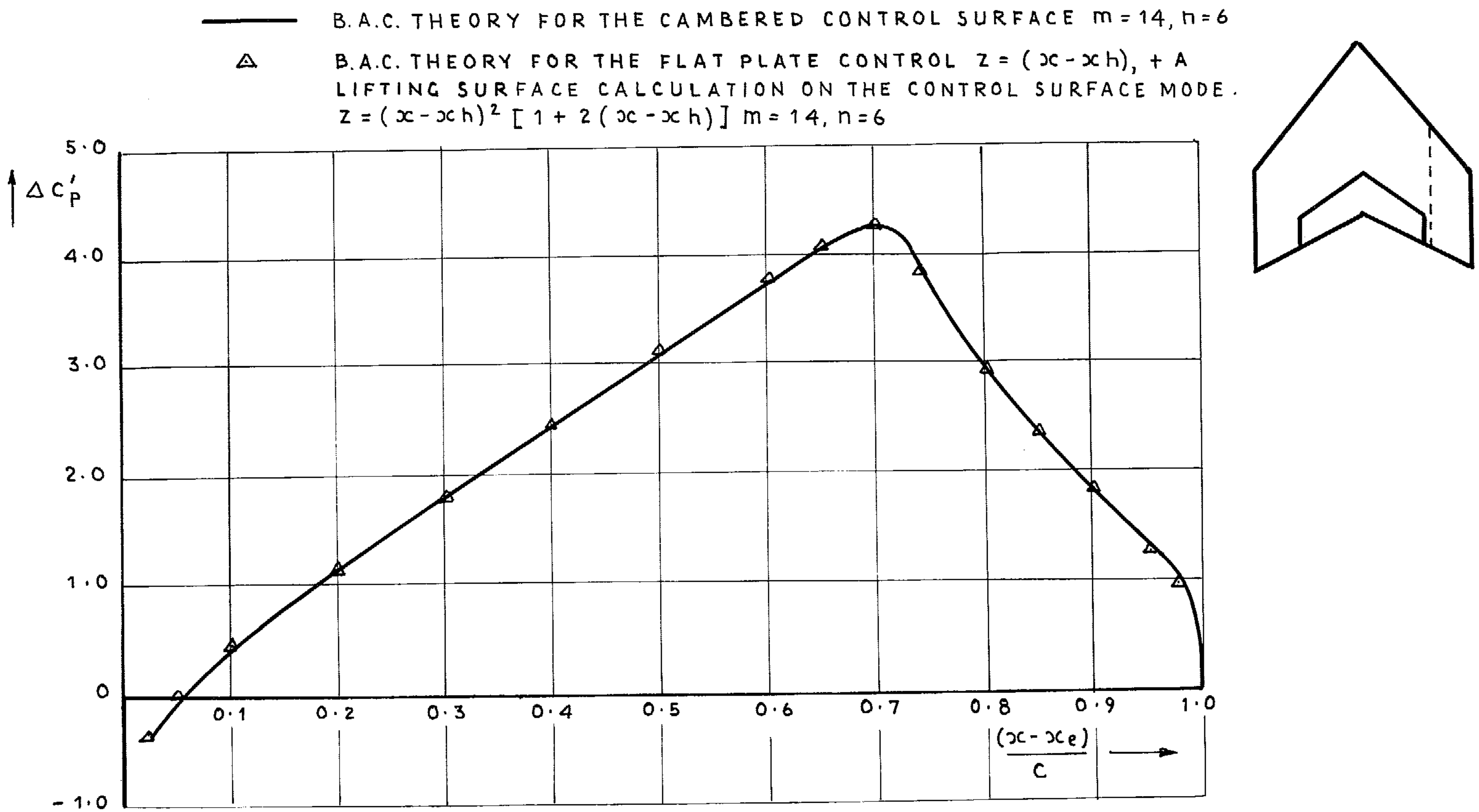

FIG. 34. Pressure comparisons for the N.L.R. swept tapered wing with a control surface camber defined by $z=(x-x_h)[1+(x-x_h)+2(x-x_h)^2]$. $M=0{\cdot}8$, $\nu=0{\cdot}672$. Real pressures for eta $(\eta)=0{\cdot}64$.

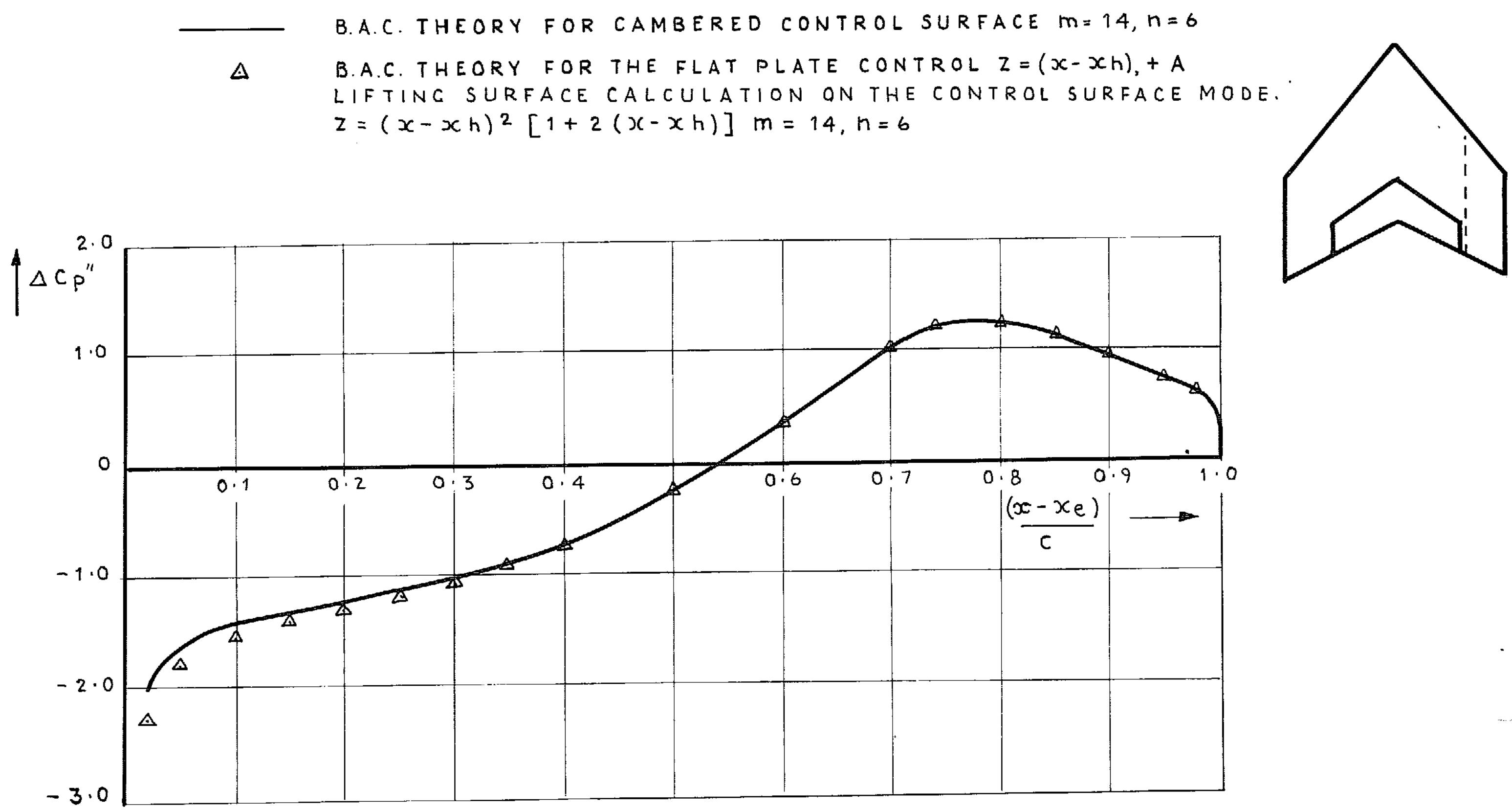

FIG. 35. Pressure comparisons for the N.L.R. swept tapered wing with a control surface camber defined by $z = (x - x_h)[1 + (x - x_h) + 2(x - x_h)^2]$. $M = 0{\cdot}8$, $\nu = 0{\cdot}672$. Imaginary pressures for eta $(\eta) = 0{\cdot}64$.

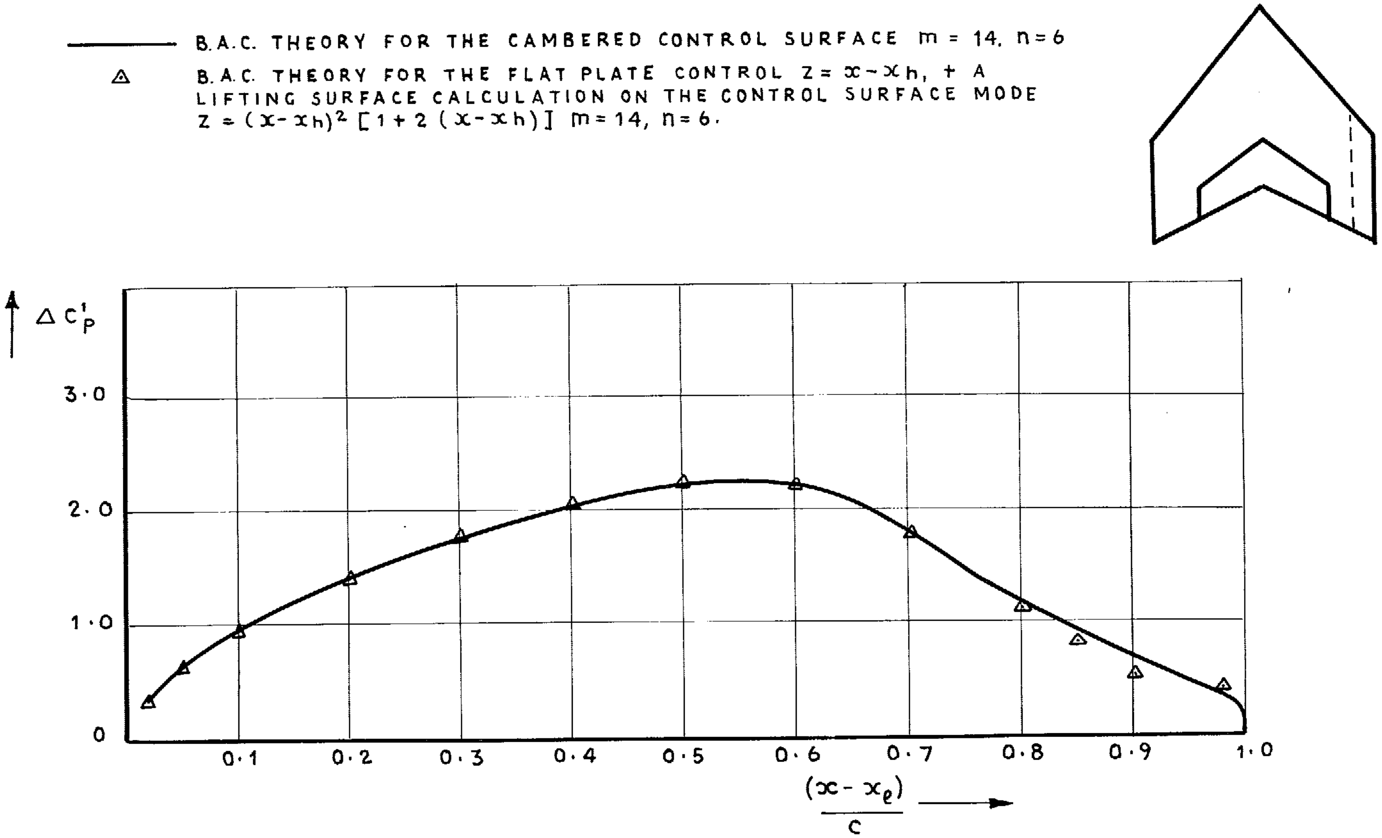

FIG. 36. Pressure comparisons for the N.L.R. swept tapered wing with a control surface camber defined by $z=(x-x_h)[1+(x-x_h)+2(x-x_h)^2]$. $M=0{\cdot}8$, $\nu=0{\cdot}672$. Real pressures for eta $(\eta)=0{\cdot}8$.

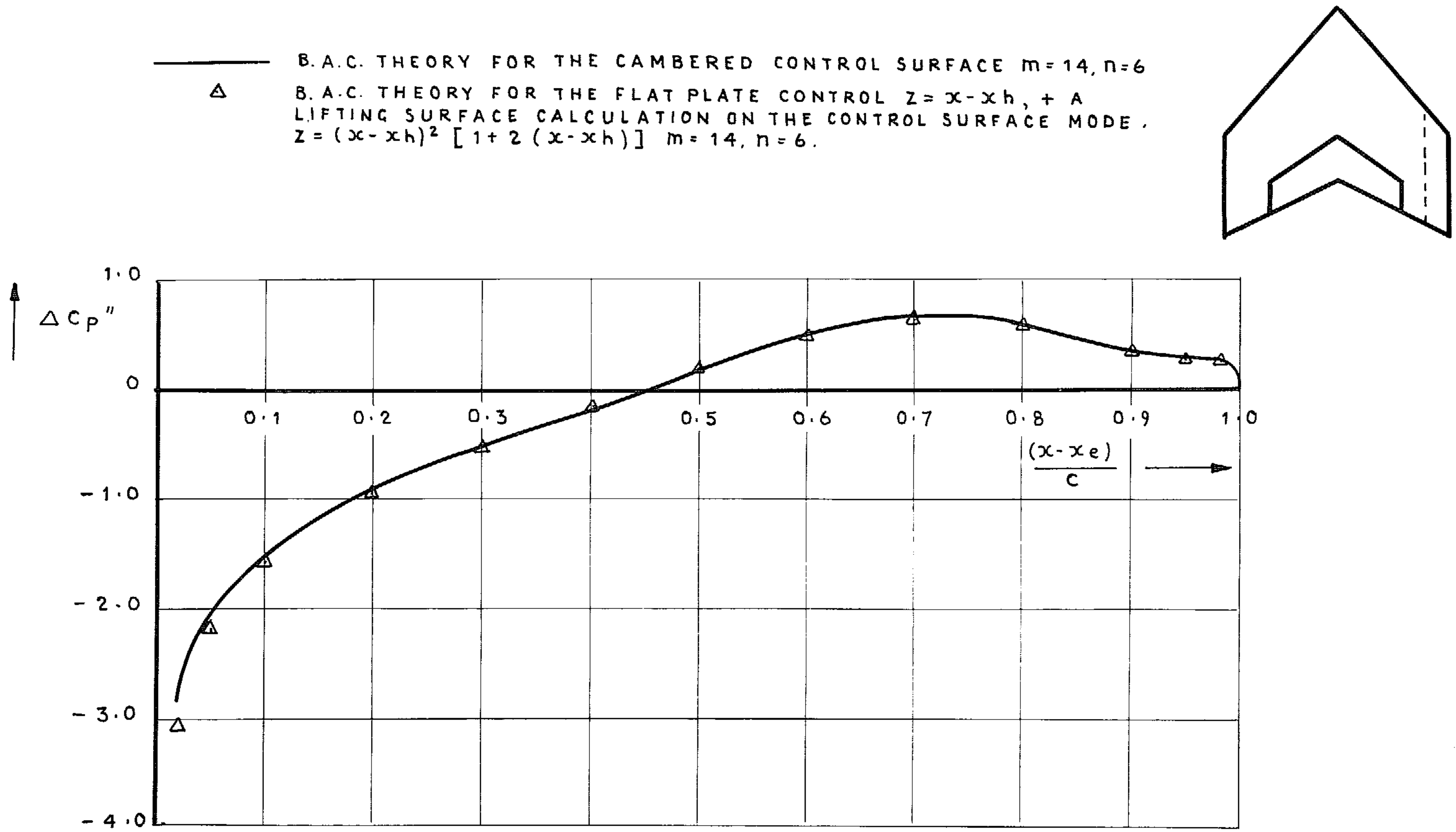

FIG. 37. Pressure comparisons for the N.L.R. swept tapered wing with a control surface camber defined by $z=(x-x_h)[1+(x-x_h)+2(x-x_h)^2]$. $M=0\cdot8$, $\nu=0\cdot672$. Imaginary pressures for eta $(\eta)=0\cdot8$.

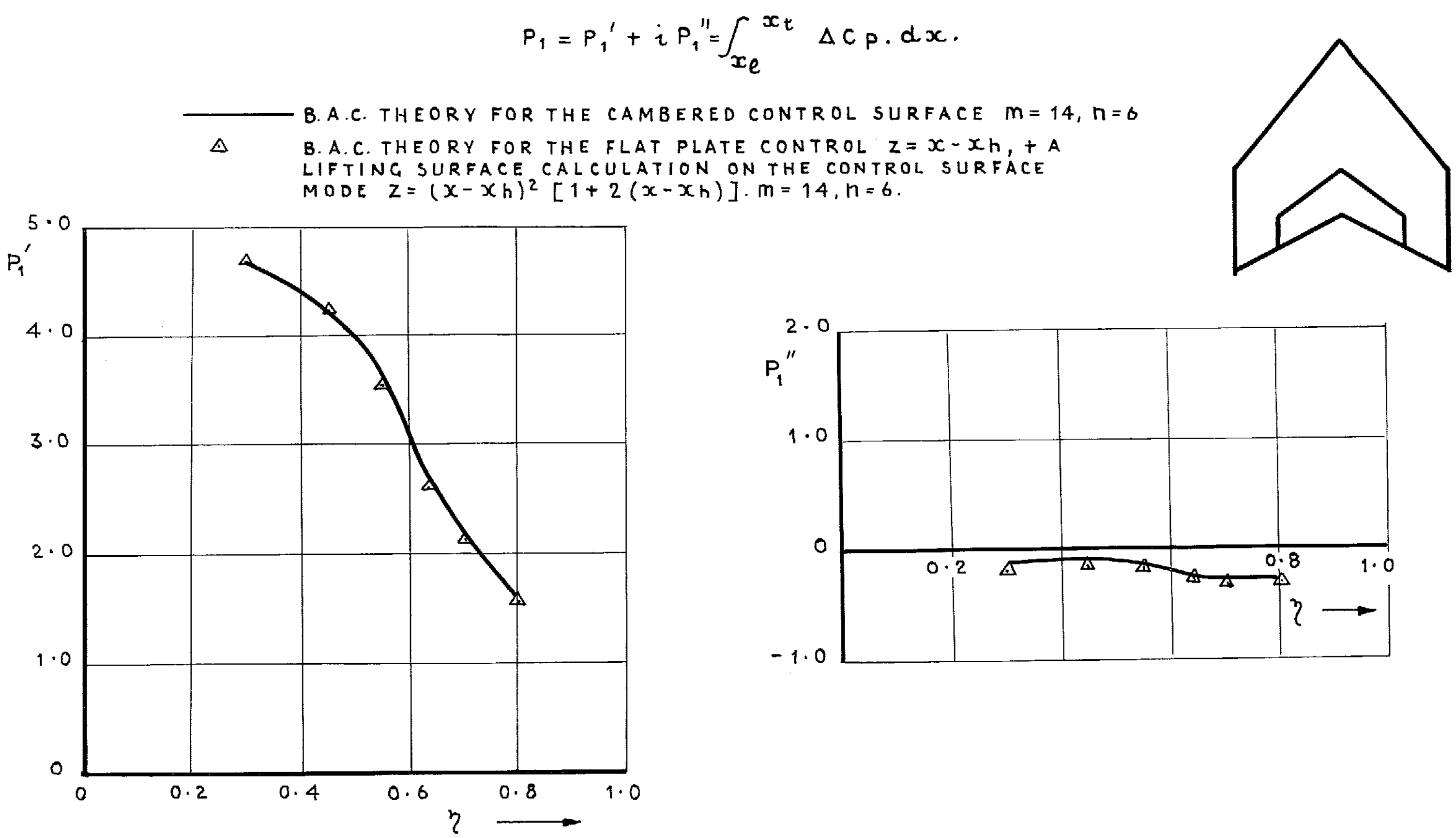

FIG. 38. Comparison of the local lift (P_1) on the N.L.R. swept tapered wing with a control surface camber defined by $z = (x - x_h)[1 + (x - x_h) + 2(x - x_h)^2]$. $M = 0{\cdot}8$, $\nu = 0{\cdot}672$.

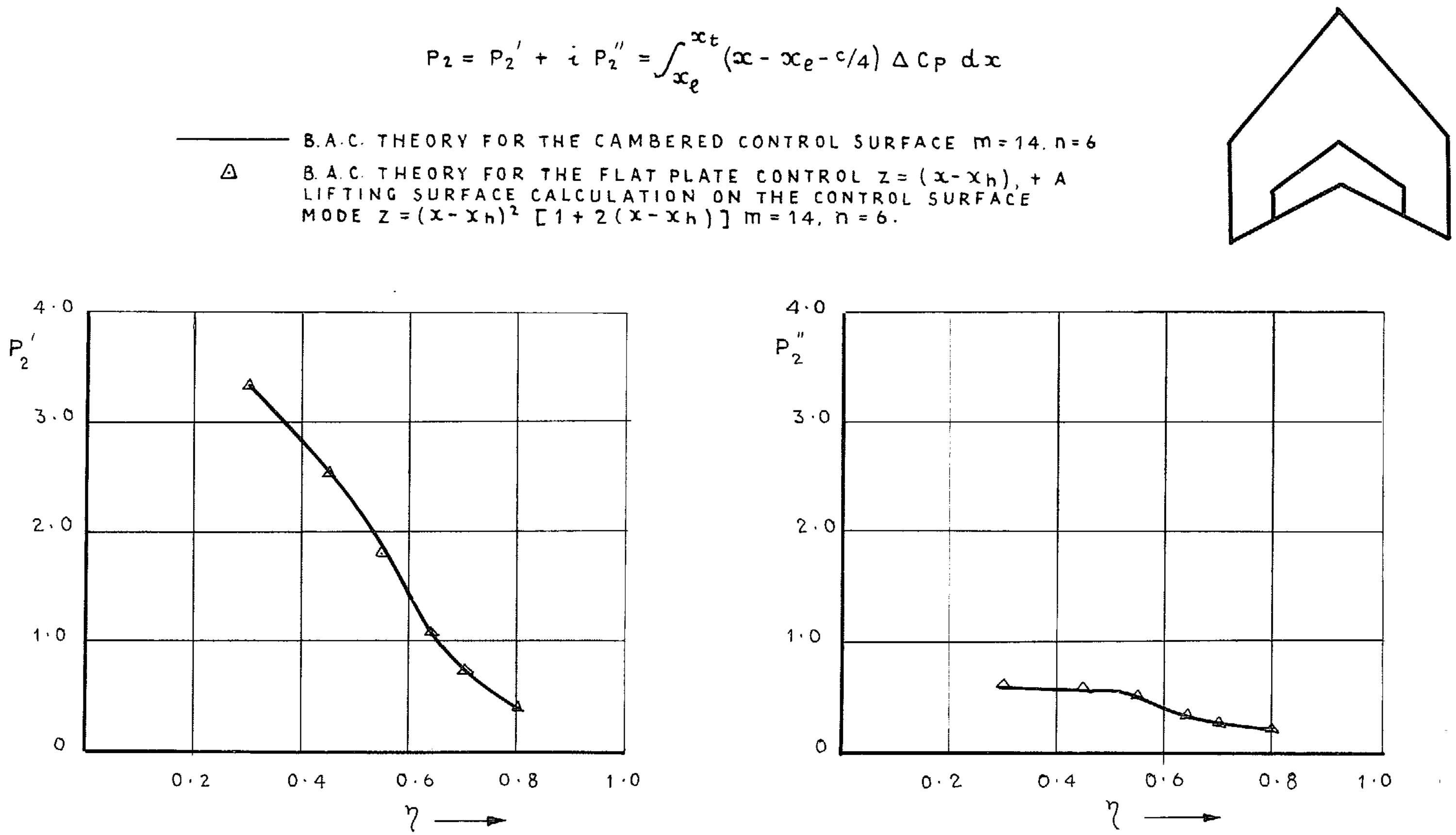

FIG. 39. Comparison of local pitching moment about $\frac{1}{4}$ chord (P_2) on the N.L.R. swept tapered wing with a control surface camber defined by $z = (x - x_h)[1 + (x - x_h) + 2(x - x_h)^2]$. $M = 0{\cdot}8$, $\nu = 0{\cdot}672$.

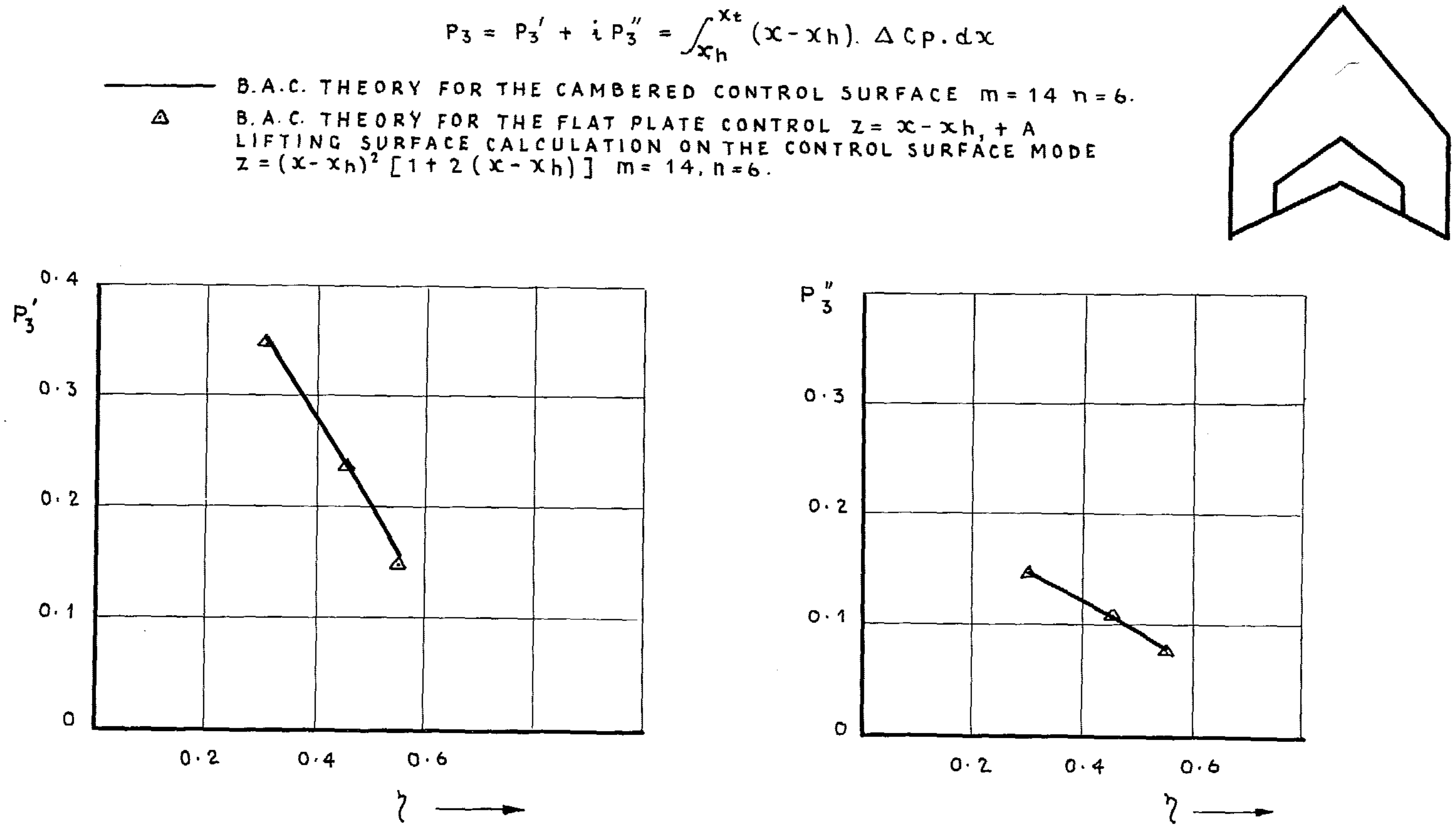

FIG. 40. Comparison of the local hinge moment (P_3) on the N.L.R. swept tapered wing with a control surface camber defined by $z = (x - x_h)[1 + (x - x_h) + 2(x - x_h)^2]$. $M = 0{\cdot}8$, $\nu = 0{\cdot}672$.

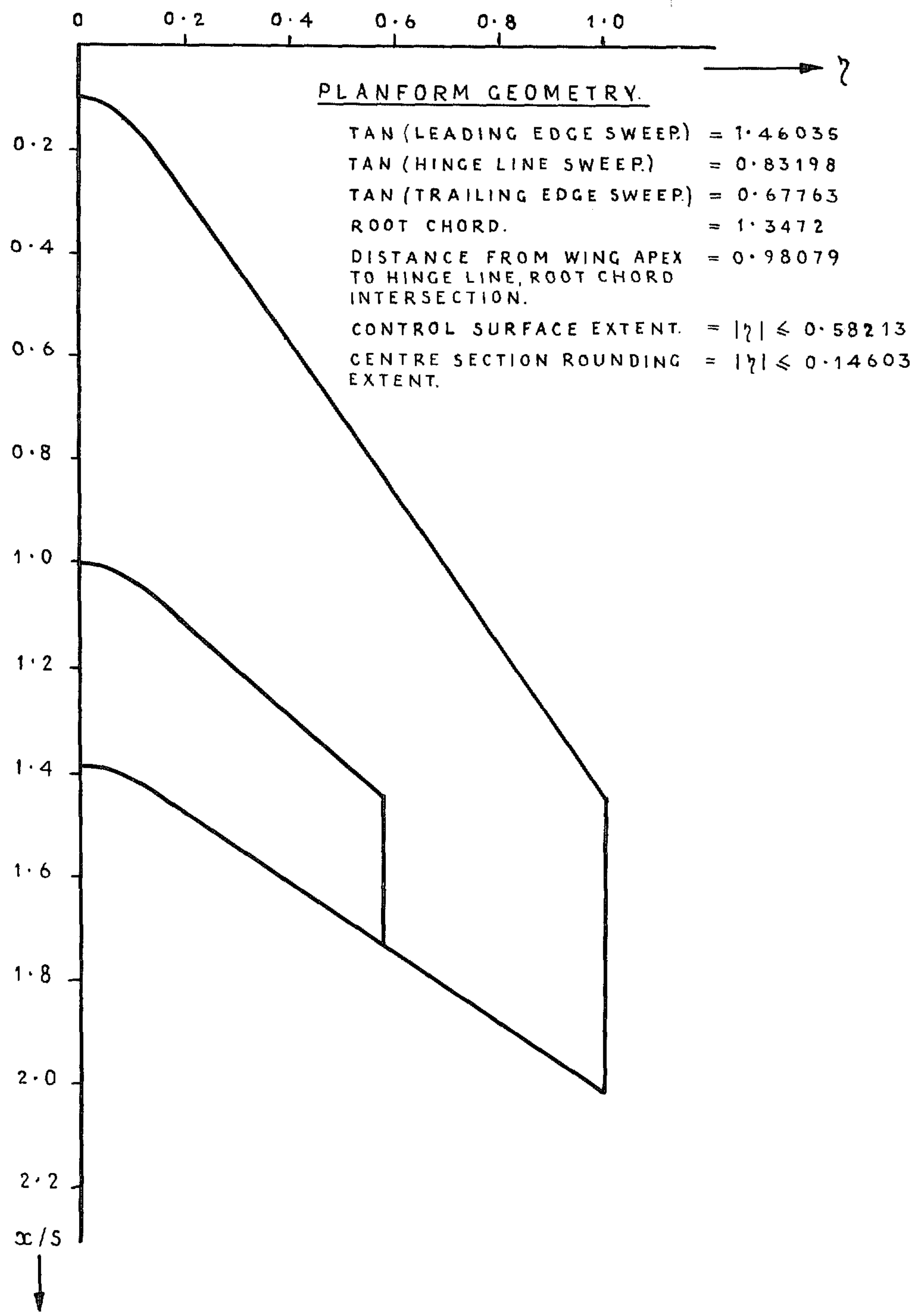

FIG. 41. B.A.C. swept tapered wing.

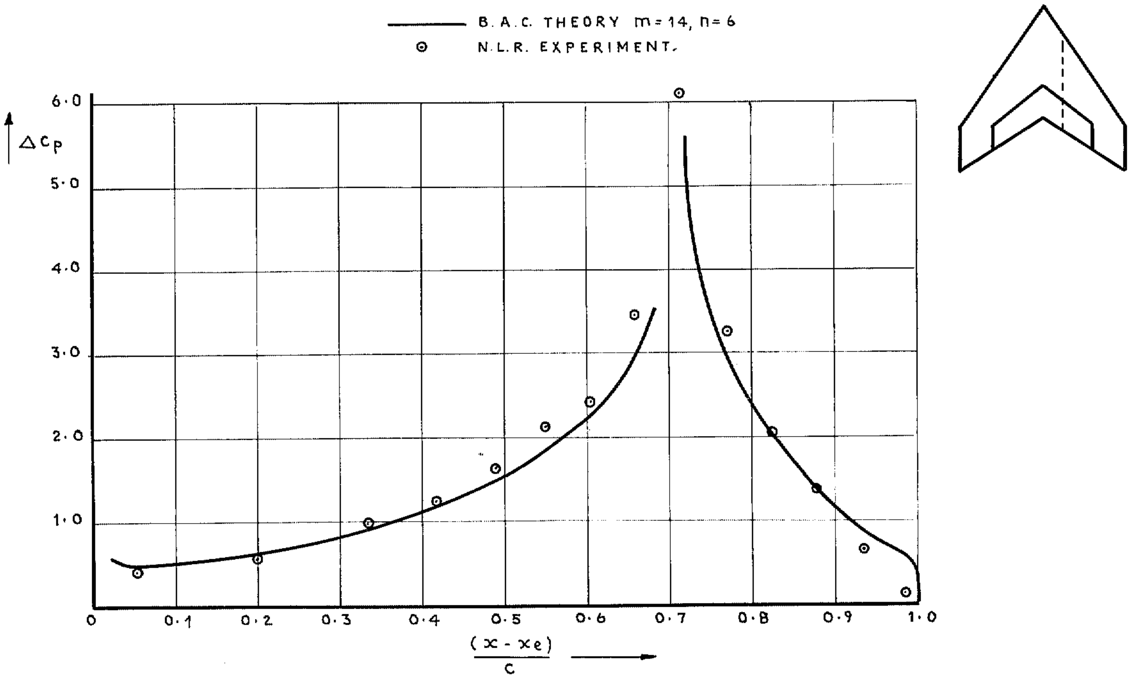

FIG. 42.

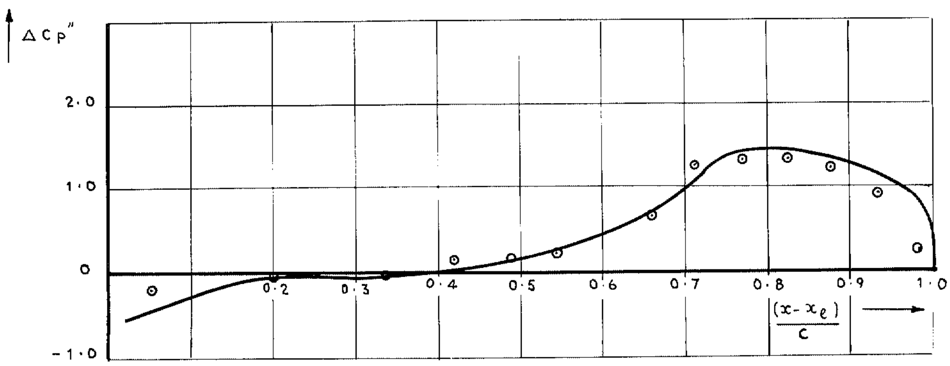

FIG. 43. Pressure comparisons for the B.A.C. swept tapered wing. $M = 0{\cdot}5$, $\nu = 0{\cdot}9551$. Real and imaginary pressures at eta $(\eta) = 0{\cdot}2512$.

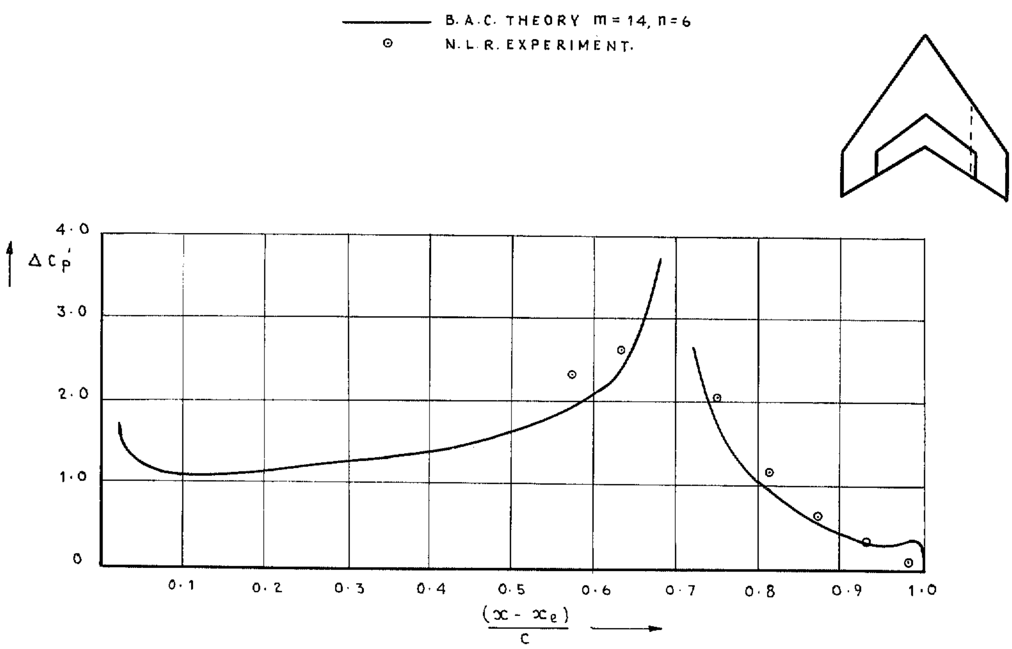

FIG. 44.

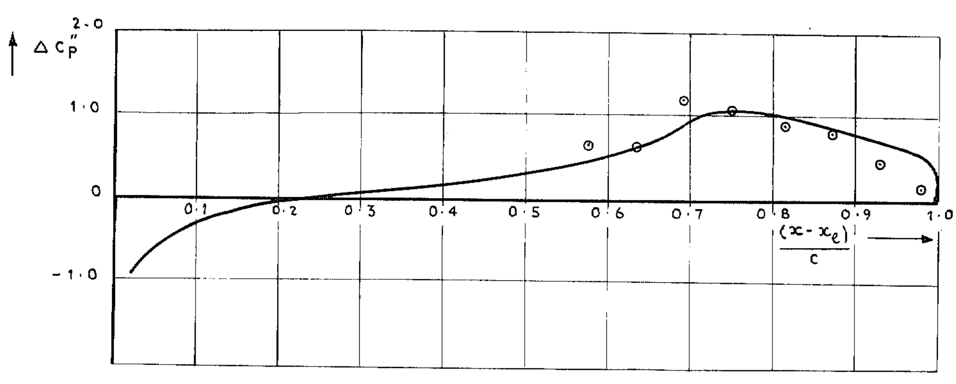

FIG. 45. Pressure comparisons for the B.A.C. swept tapered wing. $M = 0{\cdot}5$, $\nu = 0{\cdot}9551$. Real and imaginary pressures at eta (η) $= 0{\cdot}5454$.

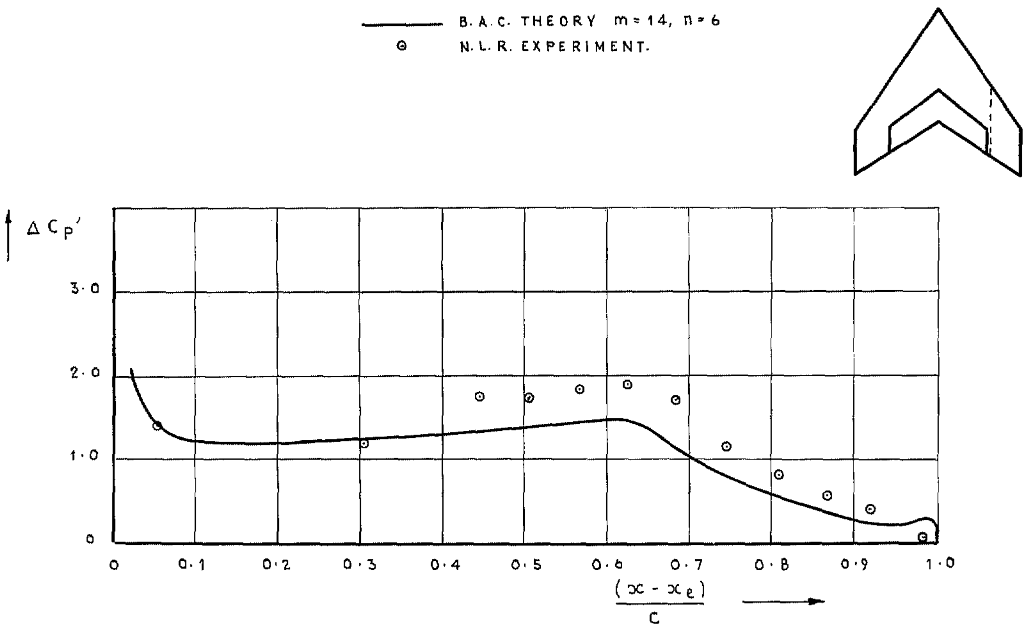

FIG. 46.

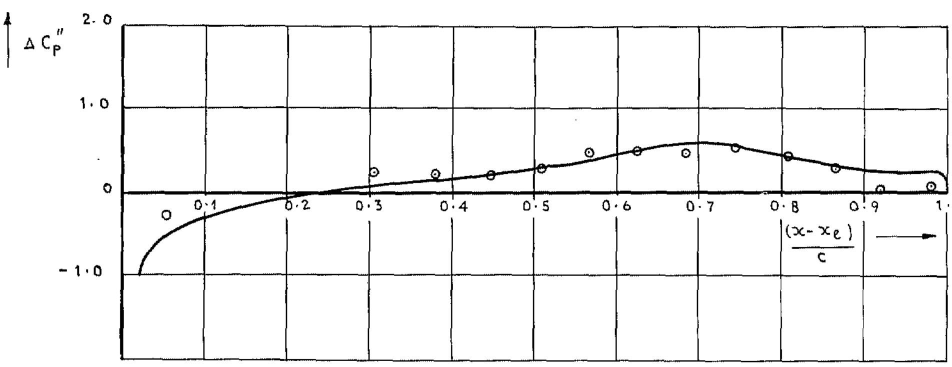

FIG. 47. Pressure comparisons for the B.A.C. swept tapered wing. $M = 0{\cdot}5$, $\nu = 0{\cdot}9551$. Real and imaginary pressures at eta $(\eta) = 0{\cdot}6281$.

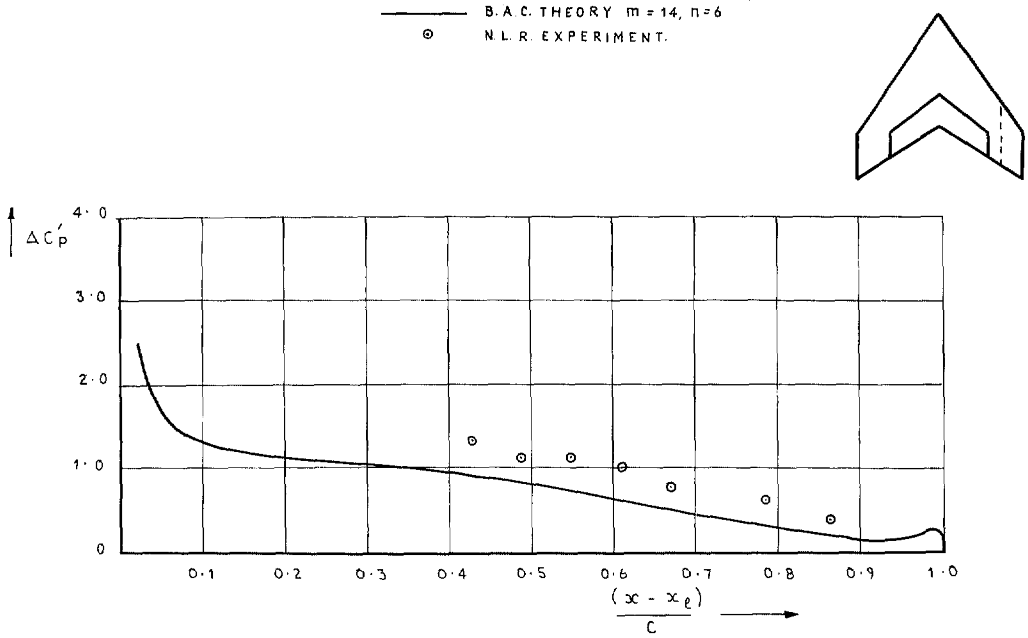

FIG. 48.

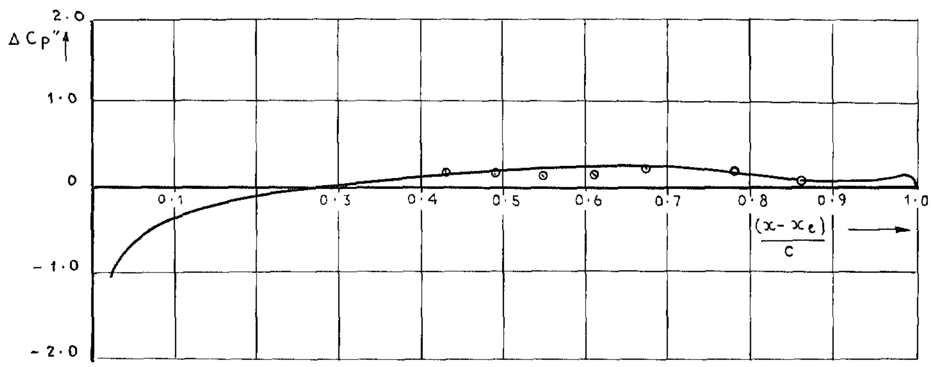

FIG. 49. Pressure comparisons for the B.A.C. swept tapered wing. $M = 0{\cdot}5$, $\nu = 0{\cdot}9551$. Real and imaginary pressures at eta (η) $= 0{\cdot}7438$.

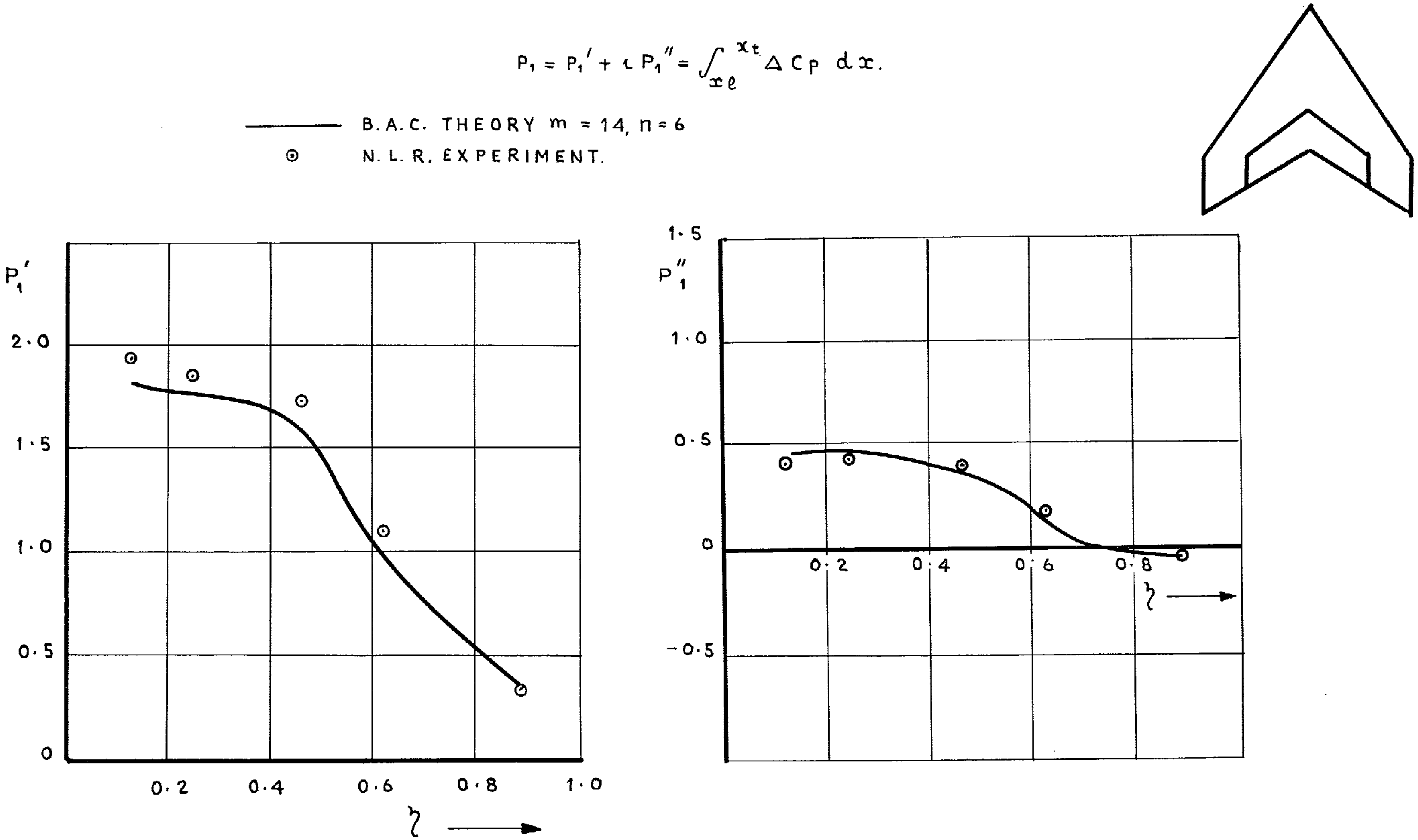

FIG. 50. Comparison of the local lift (P_1) on the B.A.C. swept tapered wing. $M = 0{\cdot}5$, $\nu = 0{\cdot}9551$.

$$P_2 = P_2' + i P_2'' = \int_{x_\ell}^{x_t} (x - x_\ell - c/4)\, \Delta c_p \, dx.$$

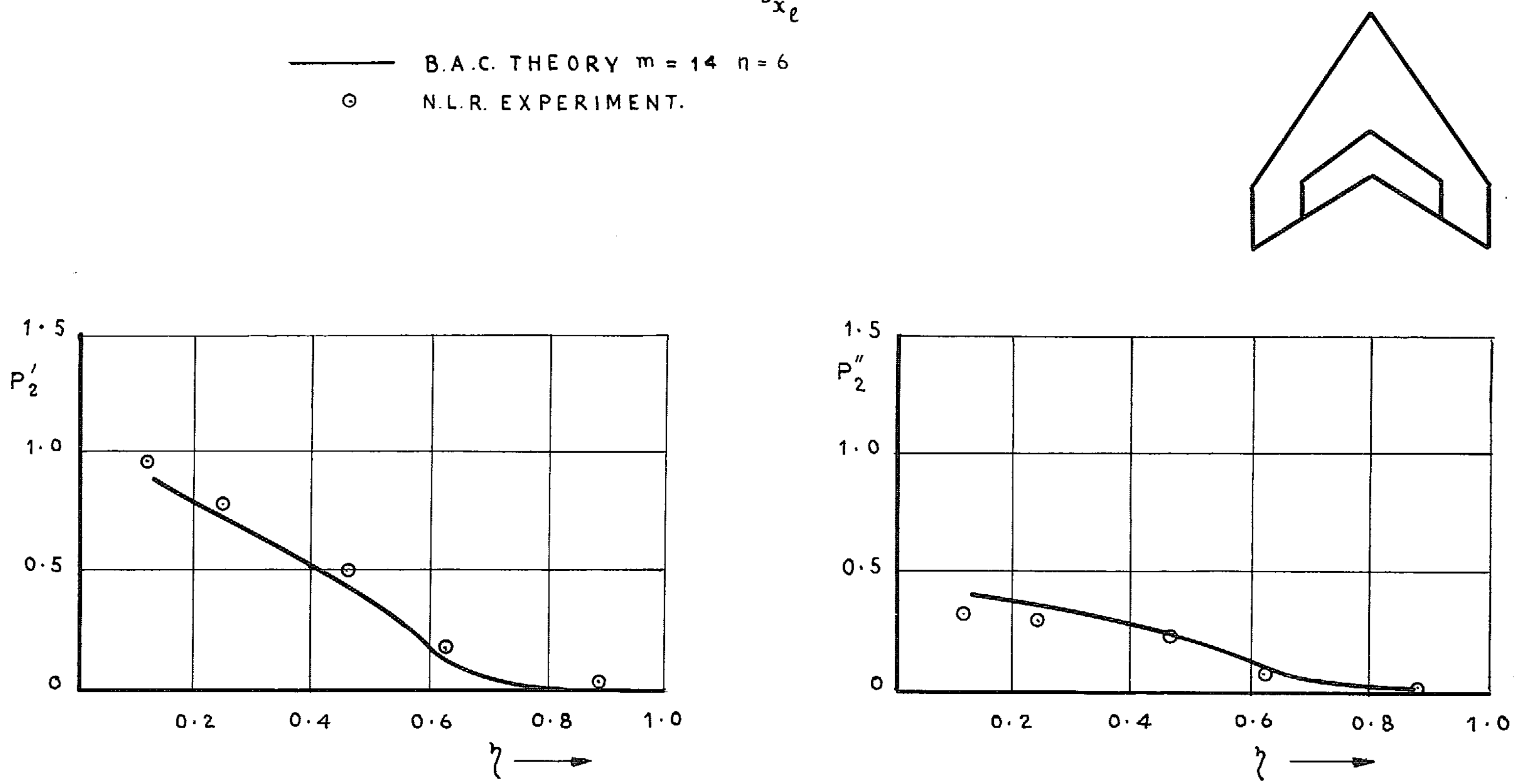

FIG. 51. Comparison of the local pitching moment (P_2) about $\frac{1}{4}$ chord on the B.A.C. swept tapered wing. $M = 0{\cdot}5$, $\nu = 0{\cdot}9551$.

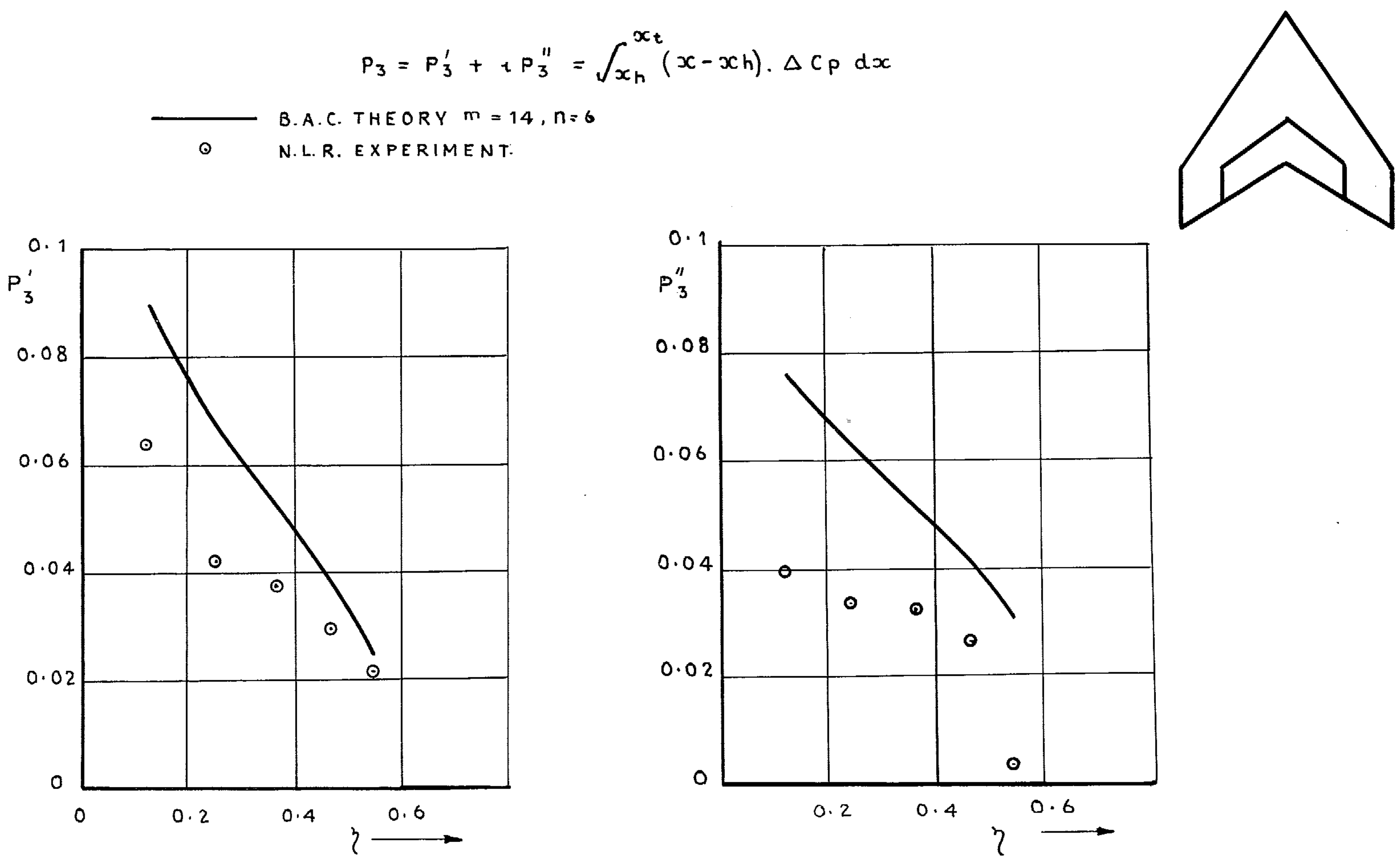

FIG. 52. Comparison of the local hinge moment (P_3) on the B.A.C. swept tapered wing. $M = 0{\cdot}5$, $\nu = 0{\cdot}9551$.

Printed in England for Her Majesty's Stationery Office by J. W. Arrowsmith Ltd., Bristol BS3 2NT
Dd. 289031 K.5. 3/76.

R. & M. No. 3783

HER MAJESTY'S STATIONERY OFFICE

Government Bookshops

49 High Holborn, London WC1V 6HB
13a Castle Street, Edinburgh EH2 3AR
41 The Hayes, Cardiff CF1 1JW
Brazennose Street, Manchester M60 8AS
Southey House, Wine Street, Bristol BS1 2BQ
258 Broad Street, Birmingham B1 2HE
80 Chichester Street, Belfast BT1 4JY

Government publications are also available through booksellers

R. & M. No. 3783
ISBN 0 11 470954 8